Ring-Polymer Approaches to Instanton Theory

Jeremy O. Richardson

Pembroke College, University of Cambridge

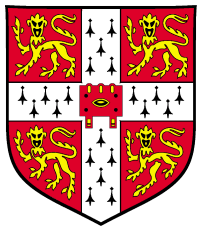

This dissertation is submitted for the degree of
Doctor of Philosophy

22nd May 2012

Abstract

Inspired by the success of the ring-polymer molecular dynamics (RPMD) method, we derive a transition-state-theory version (RPTST) with a dividing surface which is, in general, conical in ring-polymer space. It is explained why this conical form is a good approximation to the optimal dividing surface and therefore why centroid-based quantum transition-state theories are inaccurate for asymmetric barriers at low temperatures.

The geometry of the ring-polymer transition state is found to describe a finite-difference approximation to the semi-classical instanton trajectory (a classical periodic orbit of length $\beta\hbar$ on the inverted potential). Based on this, a new practical method for locating multidimensional instantons is proposed, by computing saddle points on the ring-polymer surface, and a derivation for the reaction rate constant based on the "$\mathrm{Im}\,F$" premise using the ring-polymer formalism is shown to be far simpler than in previous instanton approaches based on functional determinants. The resulting expression is based only on the ring-polymer potential at the transition-state and its Hessian, and is applied to evaluate the rate in a number of polyatomic systems. We show that a free-energy version of the $\mathrm{Im}\,F$ instanton theory is related to RPTST and thereby provide an explanation for why RPMD produces accurate results for thermal reaction rates in the deep-tunnelling regime and demonstrate how it can be made more efficient and systematically improved. From this, we also explain why RPMD is seen to underestimate the rates of symmetric reactions and overestimate the rates of asymmetric reactions.

We also present a ring-polymer instanton derivation of a theory for calculating tunnelling splittings leading to another new practical method, which owing to its simple form, is easily extended to determine the entire tunnelling-splitting pattern of molecular clusters with two or more degenerate wells. This method is applied to the water dimer, trimer, and octamer, and shown to be in good overall agreement with experiment and to provide a deeper understanding of the tunnelling pathways.

Declaration

This dissertation is the result of my own work and includes nothing which is the outcome of work done in collaboration except where specifically indicated in the text. Some of the work described in this thesis has been published in:

- J. O. Richardson and S. C. Althorpe. "Ring-polymer molecular dynamics rate-theory in the deep-tunneling regime: Connection with semiclassical instanton theory." *J. Chem. Phys.* **131**, 214106 (2009).
- J. O. Richardson and S. C. Althorpe. "Ring-polymer instanton method for calculating tunneling splittings." *J. Chem. Phys.* **134**, 054109 (2011).
- J. O. Richardson, S. C. Althorpe and D. J. Wales. "Instanton calculations of tunneling splittings for water dimer and trimer." *J. Chem. Phys.* **135**, 124109 (2011).

The number of words in this thesis does not exceed the limit set by the degree committee.

Acknowledgements

I would like to thank my supervisor, Stuart Althorpe, for his help, insight and guidance throughout the whole period which I have been working on this project. I also gratefully acknowledge the Engineering and Physical Sciences Research Council for providing funding.

It is difficult to overestimate the popularity of instantons.

Vainshtein et al. (1982)

Contents

Chapter 1

Introduction

This work is concerned with developing, improving, and gaining a better understanding of methods used for the study of nuclear quantum effects in chemistry and in particular for the computation of reaction rates and tunnelling splittings. First, we review some of the most important methods and concepts which can be used for these calculations before describing the new work introduced and showing how it contributes to the field.

For many chemical systems, we are able to make use of the Born-Oppenheimer approximation which accurately separates the electronic from the nuclear dynamics. This allows a potential energy surface (PES) to be defined on which the nuclei move according to the laws of quantum mechanics. In this thesis, only single-surface systems will be studied as multi-state non-adiabatic generalizations of the new work are not yet known.

There is a wide variety of exact and approximate methods which have been applied to the calculation of properties related to quantum nuclear dynamics. A representative selection, by no means complete, of methods in this class is summarized here. We shall return to some of the methods described when the specific applications of calculating thermal rate constants and tunnelling splittings are discussed below.

1.1 Exact dynamical methods

The majority of exact methods compute either the time-independent or time-dependent nuclear wave function directly and use this to calculate the required observable properties of the system. There are two main approaches

for calculating the time-independent wave function: a basis-set expansion can be used, for which one solves matrix equations for the coefficients, or else the solution to the differential equations can be computed directly using numerical iterative schemes.

One such method of the former type involves the diagonalization of the Hamiltonian projected onto a finite spectral representation to obtain the eigenstates of the system (Chan and Stelman, 1963). The integrals are usually computed as a finite sum using Gaussian quadrature (Harris et al., 1965). The method is exact in the limit of a complete basis set, and so the results can be converged to whatever accuracy is required. However, unless the basis functions are chosen to be similar to the correct eigenfunctions, a very large basis set, and hence a large amount of computation, will be needed to construct the matrix required for convergence. The calculation of the time-independent wave function is also possible in a pseudo-spectral basis set such as a discrete variable representation (Light et al., 1985).

The other approach for computing time-independent wave functions is provided by methods such as the Numerov (Blatt, 1967) and log derivative (Johnson, 1973; Manolopoulos, 1986) methods which compute solutions to the Schrödinger equation using a stepwise finite-difference integration of the second-order ordinary differential equation.

Exact time-dependent methods propagate wave packets on the potential energy surface, for example by the split operator method (Feit et al., 1982). The wave packets are usually represented on a grid which avoids expansion in an predetermined basis set, but as for the time-independent methods, it soon becomes intractable as the number of atoms grows (Althorpe and Clary, 2003) such that the largest system treated in this way is the $H_2 + OH$ reaction in six degrees of freedom (Zhang and Zhang, 1994). This is because of the non-local nature of wave functions and the size of the space, which increases exponentially with the number of degrees of freedom, that must be represented by the grid as the wave function spreads out. Other problems include unphysical reflections from the edge of the grid, which, although they are mostly relieved by artificial absorbing potentials (Gonzalez-Lezana et al., 2004), set a lower bound on the size of the grid that must be used. An advantage of the method over the time-independent case is that it can sometimes reveal the dynamics of the system in an intuitive way; a movie of $|\psi^2(t)|$ can be made, from which the reaction mechanism may be discerned.

One important development of the time-dependent method is the multi-configurational time-dependent Hartree (MCTDH) approach (Meyer et al., 2009). This has increased the size of the reactions which it is possible to study from four atoms to six by expanding the wave function as a product of single-particle functions and including correlation between the degrees of freedom with a sum over configurations. Wave-packet propagation in this form can be performed efficiently if the PES can be written, to a good approximation, as a product of single-particle potentials. The method is able to treat very large system-bath models where correlation between the modes is minimal, but because the difficulty rapidly increases when simulating large systems with strong correlations between the degrees of freedom, it is not suited to more complex large systems.

Degrees of freedom can of course be frozen or treated adiabatically to reduce the dimensionality of the system and make these time-independent (Bowman, 1991; von Horsten et al., 2011) and time-dependent (di Domenico et al., 2001) methods applicable to polyatomic systems, but this is neither a rigorous nor systematic approximation; the errors cannot be controlled and no information can be gathered about what has been lost. In order to obtain information of the quantum effects on these complex systems, approximate methods which can treat all degrees of freedom equally must instead be used, to which we now turn our attention.

1.2 Semi-classical methods

The application of the correspondence principle, which states that the laws of quantum mechanics must reduce to those of classical mechanics in the limit $\hbar \to 0$, has provided a range of approximate semi-classical methods, which, although they seem to emanate from diverse theories, are all inherently related by taking this limit. One such method is the Wentzel-Kramers-Brillouin (WKB) approximation which neglects high-orders of $\hbar$ and attempts to construct the wave function in the classically-allowed and forbidden regions separately, joining them at the so-called "classical turning-points" (Schiff, 1968, §34). The result is that the wave function is proportional to $\mathrm{e}^{\mathrm{i}S/\hbar}$, where $S = \int \mathrm{d}x \, \sqrt{2m(E - V(x))}$ is the classical action (Goldstein et al., 2002, ch. 2) and becomes imaginary in classically-forbidden regions and hence describes exponential decay. In this way the WKB approximation extends classical

mechanics to allow for tunnelling effects. There is, however, no general method for extending such calculations to more than one dimension.

Simple scattering problems, including elastic, inelastic and reactive collisions, have been successfully treated using "classical dynamics plus quantum superposition". These methods are able to describe interference, tunnelling, quantization and selection rules and are based only on classical trajectories (in complex phase space for classically-forbidden processes) with probability amplitudes related to the WKB phase term (Miller, 1974*a*). The semi-classical propagator for these processes (Gutzwiller, 1967) takes a prefactor equal to a determinant attributed to van Vleck (1928). This is equivalent to a stationary-phase approximation of Feynman's path integral approach (Feynman and Hibbs, 1965), which provides an alternative but equivalent methodology to the usual wave-function description of quantum mechanics in which the propagator is expressed as the sum over all paths between the initial and final coordinates, each with a phase again equal to $S/\hbar$. In the limit $\hbar \to 0$, the phases vary enormously for small changes in the path and the integrand becomes very oscillatory and sums to zero except in the vicinity of the paths where $S[x(t)]$ is stationary. According to Hamilton's principal, it is classical trajectories for which the action is stationary, and therefore, as it is only these paths which contribute, this explains how classical mechanics is recovered. In the semi-classical limit, these classical trajectories are given a Jacobian-type determinant based on the stability of the trajectory, which effectively describes some of the quantum paths which lie very near by. Using the semi-classical propagator, an approximation to the S-matrix can be defined, the elements of which give the quantum-mechanical amplitudes and hence the probabilities for transition from each reactant state to each product state (Schiff, 1968, §36).

An improvement to this method for including quantum effects into molecular dynamics simulations is provided by the semi-classical initial-value representation (SC-IVR) (Skinner and Miller, 1999; Miller, 2001), which removes the necessity of end-point boundary conditions on the trajectories and expresses the propagator as an integral over initial conditions. Another useful contribution was made by Herman and Kluk (1984), who proved that the frozen-Gaussian method (Heller, 1981) stems from the semi-classical propagator. This method surrounds each classical trajectory with an analytical Gaussian wave packet with average position and momentum equal

to that of the initial point of the trajectory and with a phase equal to the classical action along the path. The wave function can be formed from the superposition of the swarm of Gaussian wave packets at final time.

All these forms of semi-classical dynamics based on real-time trajectories suffer from convergence problems when computing reaction rates in complex systems (Yamamoto et al., 2002), because although the phase is stationary in the immediate vicinity of the classical path, the other classical trajectories have quite different phases and may contribute with opposite signs, making it very difficult to converge the integral. Indeed, the reason why all the real-time quantum methods described so far are limited to small systems stems from this "sign problem", because of which, methods common in classical simulations such as Monte Carlo and molecular dynamics cannot be used.

1.3 Quantum statistical methods

Computing thermodynamical properties of quantum systems is far easier than dynamical properties. The Boltzmann operator is equivalent to a propagator in imaginary time, where the problems concerning phase oscillations disappear as the integrand becomes a function of exponential decay. There are two main approaches based on an imaginary-time formulation of quantum mechanics which can be used for computing stationary states and equilibrium phenomena: the methods of diffusion Monte Carlo (DMC) and imaginary-time path integrals.

The DMC method is a powerful way of computing the time-independent ground-state wave function in polyatomic systems (Suhm and Watts, 1991). It exploits the equivalence between a recasting of the Schrödinger equation in imaginary time and a diffusion equation, which can be solved by random walks of many replicas of the system, such that after many iterations, the excited states decay away leaving the walkers arranged so as to describe the ground-state wave function. An extension to compute excited states is possible if the wave function's nodes are known *a priori*. It would be too difficult to treat dynamical processes in this way but the method has been successfully used to compute vibrational states and tunnelling splittings; we shall return to these applications in §1.5. A large amount of sampling is necessary to converge the results, and it is thus suitable for systems described

by fairly cheap potentials.

The other approach, that based on an imaginary-time path-integral representation of the Boltzmann operator (Feynman, 1972), is the foundation of all the work derived in this thesis. In imaginary time, the complex oscillatory integrand of the standard path integral becomes a positive real decaying exponential, which is far easier to work with. If the path integral is discretized, one obtains an expression equivalent to a classical partition function of many replicas of the system connected together by harmonic springs; this is called a ring polymer. It is possible to evaluate the integrals, and hence the quantum statistics and thermodynamics, exactly using standard classical statistical mechanics including Monte Carlo (Ceperley, 1995) or molecular dynamics (Tuckerman, 2002) methods, even while employing *ab initio* potentials (Marx and Parrinello, 1996). Numerical methods based on this principle scale well with system size (the calculation of the PES is the limiting step), such that all degrees of freedom can be treated in an equivalent way and can be used to compute static properties of large systems fully quantum mechanically (Chandler and Wolynes, 1981; Parrinello and Rahman, 1984). Although they neglect interference effects and the real-time quantum dynamics, it is possible to recast certain dynamical calculations in terms of statistics, as we discuss below, such that these ring-polymer methods are applicable.

The methods reviewed so far can be used to describe a whole range of quantum effects. In the following sections, we turn our attention to the particulars of computing rates and tunnelling splittings of chemical systems.

1.4 Chemical reaction rates

In the study of chemical reaction dynamics, an important quantity of interest is the thermal rate constant (Hänggi et al., 1990). For example, there is considerable interest in the catalytic effect on the rate of a reaction in a biological system (Kamerlin and Warshel, 2010). The reaction mechanism can often be inferred from a theoretical approach to calculating the temperature dependence of the rate constant and the kinetic isotope effect. We shall review some of the foremost methods which can be used for the computation of rate constants and describe some of the historical and theoretical background to the approaches used in the main part of this work.

The concept of a rate constant can be defined for reactions for which

it is possible to divide the configuration space into products and reactants by a dynamical variable or reaction coordinate. Often these are separated by a high activation barrier, over which transitions caused by statistical fluctuations from the thermally equilibriated reactants can be considered to be rare events, for the effects of recrossing of the barrier must decay away quickly or the reaction will be reversible on a short timescale and the rate constant will be undefined (Chandler, 1987, §8.3).

An approach for computing the reaction rate based on classical mechanics computes the trajectories on the PES and averages over those which cross the barrier (Levine, 2005, §5.2). However, the inclusion of quantum-mechanical effects in such calculations is often important, because for reactions at low temperature or involving light atoms, and especially the transfer of hydrogen, the effects of tunnelling can increase the rate by many orders of magnitude. Much work has been concentrated on computing the correct rate in these cases where classical mechanics fails.

Quantum rates were first computed via the reactive scattering matrix (S-matrix) using the exact quantum-dynamical methods described above, and such approaches are therefore limited to small systems. Miller put reaction-rate theory into a more general form (Miller, 1974*b*) by deriving a formula for the rate constant from the Boltzmann average of the reactive cross-section. This gave an expression in terms of the long-time limit of a flux-side correlation function, which is similar to that of classical rate theory except that it tends to zero in the $t \to 0^+$ limit. In this formulation, the rate is independent of the choice of dividing surface which can be important for calculations on complex systems where it is difficult to locate the optimal surface. The method was applied to simple test cases by Miller et al. (1983), to a fully-dimensional four-atom system (Manthe et al., 1993), and to $H+CH_4$ using MCTDH (Huarte-Larrañaga and Manthe, 2000). For "direct reactions", those for which the system passes quickly through the barrier region (Levine, 2005, §4.4.1), the method is able to calculate the rate at short times without constructing the S-matrix of state-to-state reaction probabilities and is thus a more efficient method for computing thermal rates than is provided by quantum scattering calculations. However, because of the difficulties involved in propagation of multidimensional wave functions, it has not been practical to apply the method to larger systems.

A popular approximation used in the calculation of classical rate constants

for direct reactions is transition-state theory (TST). Modern approaches to TST define the rate in terms of the short-time limit of the classical flux-side correlation function, and it is thus a statistical rather than a dynamical theory. The dividing surface is placed along a reaction coordinate which leads from reactants to products, and the TST approximation assumes that the barrier region is the bottleneck for the reaction and that classical trajectories having crossed the dividing surface would not return (Levine, 2005, §6.1); it is not therefore applicable to systems with diffusive dynamics. The rate is given by a flux through the dividing surface and the ratio of the partition function constrained to the dividing surface and the partition function of the reactants, each of which is computed by standard statistical-mechanics methods. The TST rate depends exponentially on the location of the dividing surface, but as it can be shown to give an upper bound to the classical result, the dividing surface can in practice be variationally chosen to give the best approximation to the classical rate (Truhlar and Garrett, 1984).

Eyring's famous TST (Eyring, 1935) chooses the dividing surface to pass through the first-order saddle point on the PES and assumes that the classical dynamics along the reaction coordinate are separable from those in the other degrees of freedom in the vicinity of the transition state. The modes perpendicular to the reaction coordinate are treated using the analytic formulae for quantum partition functions (with the approximations of rigid rotors and harmonic oscillators). Treating quantum effects perpendicular to the reaction coordinate in this way allows zero-point energy effects to become apparent but does not account for tunnelling through the barrier.

Tunnelling effects have been included approximately in some versions of TST based on *ad hoc* one-dimensional tunnelling paths with a WKB-type approximation (Truhlar et al., 1985). For example, some of the pathways which have been chosen follow the minimum-energy path, a straight line or something in-between (Marcus and Coltrin, 1977).

Because Miller's flux-side correlation function does not have a useful $t \to 0^+$ limit, it is not so obvious how to make a quantum version of transition-state theory which does not require solution of the full multidimensional reaction dynamics and would thus be able to treat complex systems including polyatomic molecules and clusters in and out of condensed phase. One would like to have a theory which makes only one assumption—direct dynamics in the barrier region—but without making the approximation that the reaction

coordinate is separable from the other degrees of freedom (Miller, 1993). The quest for such a quantum transition-state theory (QTST) still continues. Indeed, such a diverse set of theories have been named QTST, none of which rigorously fulfils this definition, that it can become rather confusing, and we shall avoid labelling any current method by the term.

One method in this class was derived by Miller (1975) from the semi-classical limit of the exact quantum flux-side correlation function. It gives an approximation to the low-temperature rate from the action and stability parameters (Gutzwiller, 1971) of a classical periodic orbit on the upside down surface (Miller, 1971). This orbit is known as an *instanton* and its action $S[x(\tau)] = \int_0^{\beta\hbar} \mathrm{d}\tau \left[\frac{1}{2}m\dot{x}(\tau)^2 + V(x(\tau))\right]$ is the same as in the WKB expression. In its original implementation, it was extremely difficult to locate the unstable periodic trajectories on general multidimensional surfaces. One had to choose the initial conditions of a trajectory such that by solving the classical equations of motion ("shooting"), the trajectory returned after a specified time, not just to the same location, but with the same momentum with which it started. However, as we shall show, more practical methods for locating instantons exist and will be used in this work.

A different formulation of instanton theory, based on the "$\mathrm{Im}\, F$" premise, was also developed (Affleck, 1981) and was recently proved to be equivalent to that of Miller's (Althorpe, 2011). This rate expression is computed from a steepest-descent approximation to the imaginary part of the partition function analytically continued into the complex plane. As in Miller's version, there is an exponential factor which depends on the action of the classical periodic orbit, but the prefactor is given as a functional determinant describing fluctuations about the instanton.

Gillan (1987) proposed a method for computing the rate based on the centroids of path integrals $\bar{q} = (\beta\hbar)^{-1} \int_0^{\beta\hbar} \mathrm{d}\tau\, x(\tau)$, and Voth, Chandler and Miller (1989) (VCM) modified Gillan's prefactor to reproduce the correct rate in the classical limit. These centroid-based methods work well for symmetric barriers but poorly for asymmetric systems at low temperature as was shown by Makarov and Topaler (1995) who also explained how Gillan's theory could be obtained from a centroid-based derivation of $\mathrm{Im}\, F$. A key step was made by Mills et al. (1997) who departed from centroid-based theory and defined the transition-state as a cone rather than a plane in the space of Feynman paths. This allowed modes other than the centroid to contribute to

the flux and hence corrected the asymmetric rates. With a steepest-descent approximation, $\mathrm{Im}\, F$ instanton theory is recovered.

The quantum instanton method (Miller et al., 2003) was derived from the flux-flux correlation function using steepest-descent approximations to the integrals in time (Vaníček et al., 2005). It is similar in form to the semi-classical instanton method but does not take the steepest-descent approximation in positional coordinates. Instead, it computes diagonal and non-diagonal elements of the quantum Boltzmann operator using path-integral Monte Carlo (Yamamoto and Miller, 2004). This corrects for errors in the local quadratic approximation present in the instanton method and performs well for deep tunnelling but is not correct for a free particle or in the high-temperature classical limit. Because two optimal free-energy dividing surfaces need to be found, this method is difficult to apply.

There is also a set of rate theories based on path integrals which do not take a TST-type approximation. The simplest is the classical Wigner method, which is a linearized version of the SC-IVR method discussed above (Miller, 2001). For this method, one propagates real-time classical trajectories chosen from a Wigner distribution of initial conditions. This method performs quite well at short times if a good dividing surface is chosen, but as the trajectories do not conserve the quantum Boltzmann distribution, it is not independent of this choice, and because quantum coherence is neglected, it is unable to describe long-time behaviour. A further difficulty is that, in order to sample a multidimensional Wigner distribution, one must make a local harmonic or Gaussian approximation (Liu and Miller, 2009).

Another such method is centroid molecular dynamics (CMD) (Voth, 1996) in which the centroid moves classically in an effective potential of mean force defined by a constrained path integral over the other modes. CMD suffers from the same problems as the centroid-based QTST methods described above when used to compute the rate of asymmetric barriers, and has the added difficulty of needing to compute the effective potential in a large space. In certain versions, the rate is not dividing-surface independent and does not necessarily systematically improve on its corresponding TST theory (Jang and Voth, 2000).

The method of ring-polymer molecular dynamics (RPMD) (Craig and Manolopoulos, 2005*b*) has been used to compute rate constants using the fictitious dynamics of path integrals. RPMD was derived starting from the

ring polymers used to sample the quantum Boltzmann statistics and by applying classical rate theory in the resulting extended phase space; it is thus independent of the choice of dividing surface. The method reproduces the correct rate for a parabolic barrier, and in its most common formulation reduces to VCM in the short-time limit but is systematically improved at longer times. The dynamics are obviously fictitious and yet the rates are surprisingly good, even in the deep-tunnelling regime. RPMD has been shown to be superior to CMD for rate calculations because of a different choice of bead masses (Braams and Manolopoulos, 2006), although the latter is more suitable for the calculation of spectra (Habershon et al., 2008).

In this work, a transition-state-theory approach is applied to RPMD and the resulting theory is shown to be related to the work of Mills et al. (1997) and hence to $\operatorname{Im} F$ instanton theory. This provides the explanation of why RPMD works so well in the deep-tunnelling regime, and thereby provides a better understanding of what can be expected from RPMD and centroid-based methods. Recognizing the similarity between instanton theory and the ring-polymer transition state provides a much simpler method for computing the instantons than had previously been applied, avoiding the problem of shooting by instead locating the periodic orbit using a saddle-point optimization on the extended ring-polymer surface. This approach also simplifies the mathematics in the derivation of instanton rate theory by avoiding stability parameters and functional determinants, and allows rates to be computed with relative ease for multidimensional reactions. We call this the ring-polymer instanton method, and it was developed concurrently but independently by Andersson et al. (2009), who called it harmonic QTST, and applied the methodology to the reaction $\mathrm{H} + \mathrm{CH_4}$ achieving results in good agreement with MCTDH.

After a mathematical introduction to the ring-polymer path-integral approach in Chapter 2, the instanton method in ring-polymer form is described in Chapter 3 and its relationship to RPMD in Chapter 4. Numerical results are given showing the accuracy of these methods.

1.5 Tunnelling splittings

The other area in which progress has been made by the work of this thesis is in the calculation of tunnelling splittings. The overlap between degenerate

eigenstates in symmetric wells leads to energy-level splitting patterns which are important observables in molecular science as they provide quantifiable clues to the structures and rearrangement dynamics in molecular clusters and help the development of accurate universal force fields.

In particular, because of the unique importance of liquid water in molecular science, water clusters have been at the centre of much interest for experimentalists and theoreticians, and both microwave and infrared rotation-vibration-tunnelling spectroscopy have provided detailed experimental data which numerous theoretical studies have attempted to reproduce. Studies on clusters, starting with the water dimer before increasing the size one monomer at a time, have provided insight into the many-body interactions which are so difficult to compute accurately (Keutsch and Saykally, 2001).

Over the years, many potential energy surfaces have been constructed to describe water clusters which we review in Chapter 6. However, many of them describe only the relative positions of rigid monomers and have been fitted empirically such that a classical dynamics simulation reproduces some experimental properties of liquid water. They are not therefore accurate enough for application to calculating tunnelling splittings, which are very sensitive to the anisotropy of the PES (Szalewicz et al., 2009). In this work, we apply our methods to accurate, and therefore more expensive, potentials such as the *ab initio* water PES of Bowman and co-workers (Wang and Bowman, 2010).

There have been a number of theoretical studies to calculate tunnelling splittings. One such exact method, the direct solution of the Schrödinger equation by diagonalization of the Hamiltonian, has been applied to small van der Waals clusters such as $(HF)_2$ and $(H_2O)_2$ with fixed monomers (Althorpe et al., 1991; Althorpe and Clary, 1994, 1995). As mentioned previously, such methods suffer from huge computational requirements and are thus not applicable to large clusters. DMC has also been used to compute tunnelling splittings in small clusters including flexible models of $(HF)_2$ (Sun and Watts, 1990; Quack and Suhm, 1995) and rigid models of water dimer to pentamer (Gregory and Clary, 1995*a*, 1996), including a study of the effects of three-body terms in the potential (Gregory and Clary, 1995*b*). In these studies the nodal positions were defined approximately using symmetry arguments, and only some of the tunnelling splittings were calculated rather than the complete pattern. We return to the specific applications of these

methods to water clusters in Chapter 6.

Path-integral approaches have also been used for computing electron transfer in a fixed environment (Kuki and Wolynes, 1987; Marchi and Chandler, 1991), and exchange frequencies in solid (fermionic) ^{3}He (Ceperley and Jacucci, 1987; Alexandrou and Negele, 1988). These theories are directly related to the computation of tunnelling splittings between two degenerate wells. They require the calculation of free energies which is well-known to be a difficult problem in classical statistical mechanics, and are therefore not appropriate for use with high-quality, expensive water potentials. A major drawback is that they have not been generalized to treat systems with more than two wells. Nonetheless, there are many similarities between these path-integral approaches and the instanton method which we shall propose.

None of these exact methods is able to treat complex systems in full dimensionality and so there is need for an approximate, yet still reliable, method which can be applied to larger water clusters using more-accurate flexible potential energy surfaces than current methods are able to manage. However, most approximate methods tend to be based on reduced dimensionality, where a reaction coordinate is chosen (Wales, 1993*b*) and the resulting one-dimensional system solved for the tunnelling splitting using the WKB or periodic-orbit approximation (Miller, 1979). These methods involve no sampling but do require prior knowledge of the tunnelling path and could potentially lead to large errors if the pathway is poorly chosen. The tunnelling pathway, along which the WKB phase integral is taken, tends to be chosen in an *ad hoc* fashion as either the line of steepest ascent to the saddle point (i.e. the minimum-energy path), or within the "sudden" approximation, the direct straight line from one minimum to another. A better approach would be to locate the optimal pathway with the smallest action as was done by Tautermann et al. (2002*a*, *b*) using the global optimization method, simulated annealing. This is not, however, a very efficient algorithm and in this thesis, we shall give a simpler method for performing this minimization and derive a more rigorous and self-contained theory based on another application of instanton theory.

In a similar way to these approximate implementations using WKB theory, the semi-classical instanton method, which was first applied to a double-well system by Polyakov (1977), can also be used to calculate tunnelling splittings based on a single pathway. The instanton pathway is defined as

the minimum-action path between the wells. However, as it has not been practical to compute this pathway in multidimensional systems until recently, reduced dimensionality approximations were used (Benderskii et al., 1994). Mil'nikov and Nakamura (2001) developed a multidimensional method able to locate instantons in many degrees of freedom. They did not shoot for trajectories, but described the tunnelling pathway as a linear combination of basis functions, and optimized the parameters to minimize the action. The method has been applied to estimate the tunnelling splitting of malonaldehyde with an *ab initio* potential (Mil'nikov et al., 2004). However, their derivation, which involves calculating the functional determinant of the instanton, has not been extended to treat systems with more than two wells.

We develop an instanton method using the same ideas as for the rate calculations—using the ring-polymer representation of the quantum partition function. This leads to far simpler mathematics than is encountered in the standard instanton literature, and importantly, has allowed the development of an practical and accurate theory which is able to compute the entire splitting pattern for a system with more than two degenerate wells. Sampling is avoided altogether, all degrees of freedom are treated equally, and no prior assumptions about the tunnelling pathways are made. The disadvantage of all instanton approaches is that fluctuations around the instanton are treated harmonically. Anharmonicity along the instanton is included exactly, however, and it thus should capture the dominant tunnelling mechanism and give results correct to within an order of magnitude. Because of the simplicity of the approach, we were able to use accurate potentials for clusters of flexible water molecules and apply the method to each of the many possible tunnelling splittings in the systems studied. The theory and example calculations of the ring-polymer instanton method for two degenerate wells is given in Chapter 5 and its extension for complex systems in Chapter 6, in which results are also given for the water dimer, trimer and octamer and predictions made for some other water clusters. The method is shown to reproduce some well-known experimental and theoretical results in most cases to well within a factor of two; it makes predictions about previously uncalculated pathways and helps explain the appearance of the experimental spectra of the water trimer and octamer. Chapter 7 concludes the thesis and describes some applications to which the methods developed here could be applied.

Chapter 2

Path Integrals and Ring Polymers

In this chapter we show how ring polymers can be used to compute quantum partition functions and provide useful concepts and relationships which will be used throughout the rest of this thesis. It was Feynman who first formulated quantum statistical mechanics in terms of path integrals (Feynman and Hibbs, 1965; Feynman, 1972). However, only a few systems are simple enough that these expressions can be evaluated analytically and so Monte Carlo and molecular dynamics techniques are often used to compute the multidimensional integrals (Ceperley, 1995; Tuckerman, 2002). Such methods have been used to compute quantum equilibrium properties, for example by Parrinello and Rahman (1984) and Marx and Parrinello (1996), and they provide a way to calculate many of the integrals needed for this work in either an exact or approximate manner.

2.1 Partition functions

The quantum partition function in the canonical (NVT) ensemble for a system with reciprocal temperature $\beta = 1/k_{\mathrm{B}}T$ is given by the well-known formula

$$Q(\beta) = \sum_n \mathrm{e}^{-\beta E_n}, \tag{2.1}$$

where the energy levels are solutions of the time-independent Schrödinger equation $\hat{H}|n\rangle = E_n|n\rangle$. For large and anharmonic systems, it will not be

possible to calculate $Q(\beta)$ in the standard manner by enumerating the energy levels, and so we require a transformation to ease the computation; this is provided by the path-integral representation.

Let us consider first one-dimensional systems with Hamiltonians of the form

$$\hat{H} = \frac{\hat{p}^2}{2m} + \hat{V}, \tag{2.2}$$

where m is the system mass, $\hat{V} = V(\hat{x})$ the potential, and $\hat{p} = -\mathrm{i}\hbar\mathrm{d}/\mathrm{d}x$ the momentum operator. The generalization to multidimensional systems will be carried out in §2.2.

The partition function can also be defined more generally as the trace of the Boltzmann operator (Chandler, 1987, §3.3)

$$Q(\beta) = \mathrm{tr}\left[\mathrm{e}^{-\beta\hat{H}}\right], \tag{2.3}$$

which reduces to Eq. 2.1 if evaluated in the basis set of eigenstates $|n\rangle$ of the Hamiltonian, but could instead be expanded in any complete set of states, for instance in the position representation as

$$Q(\beta) = \int_{-\infty}^{\infty} \mathrm{d}x \, \langle x|\mathrm{e}^{-\beta\hat{H}}|x\rangle. \tag{2.4}$$

Although the kinetic-energy part can be evaluated in the momentum representation as

$$\mathrm{e}^{-\beta\hat{p}^2/2m}|p\rangle = \mathrm{e}^{-\beta p^2/2m}|p\rangle, \tag{2.5}$$

and the potential-energy part in the position representation as

$$\mathrm{e}^{-\beta\hat{V}}|x\rangle = \mathrm{e}^{-\beta V(x)}|x\rangle, \tag{2.6}$$

the exponential of the total Hamiltonian cannot in general be evaluated in either representation because $\hat{x}$ and $\hat{p}$ do not commute.

It is, however, possible to make an approximation to the Boltzmann operator using the split-operator method or Trotter splitting. Using $\hat{T}$ as a

shorthand for $\hat{p}^2/2m$, the density matrix is

$$\begin{aligned}
\left\langle x'\middle|\mathrm{e}^{-\beta\hat{H}}\middle|x\right\rangle &\approx \left\langle x'\middle|\mathrm{e}^{-\beta\hat{V}/2}\mathrm{e}^{-\beta\hat{T}}\mathrm{e}^{-\beta\hat{V}/2}\middle|x\right\rangle && \text{(2.7a)}\\
&= \mathrm{e}^{-\beta V(x')/2}\left\langle x'\middle|\mathrm{e}^{-\beta\hat{T}}\middle|x\right\rangle \mathrm{e}^{-\beta V(x)/2} && \text{(2.7b)}\\
&= \int_{-\infty}^{\infty}\mathrm{d}p\left\langle x'\middle|\mathrm{e}^{-\beta\hat{T}}\middle|p\right\rangle\left\langle p|x\right\rangle \mathrm{e}^{-\beta[V(x')+V(x)]/2} && \text{(2.7c)}\\
&= \int_{-\infty}^{\infty}\mathrm{d}p\left\langle x'|p\right\rangle \mathrm{e}^{-\beta p^2/2m}\left\langle p|x\right\rangle \mathrm{e}^{-\beta[V(x')+V(x)]/2} && \text{(2.7d)}\\
&= \frac{1}{2\pi\hbar}\int_{-\infty}^{\infty}\mathrm{d}p\,\mathrm{e}^{-\beta p^2/2m}\,\mathrm{e}^{\mathrm{i}p(x'-x)/\hbar}\,\mathrm{e}^{-\beta[V(x')+V(x)]/2} && \text{(2.7e)}\\
&= \frac{1}{2\pi\hbar}\int_{-\infty}^{\infty}\mathrm{d}p\,\exp\left[\left(\mathrm{i}\sqrt{\frac{\beta}{2m}}p+\sqrt{\frac{m}{2\beta\hbar^2}}(x'-x)\right)^2\right.\\
&\qquad \left.-\frac{m}{2\beta\hbar^2}(x'-x)^2\right]\mathrm{e}^{-\beta[V(x')+V(x)]/2} && \text{(2.7f)}\\
&= \frac{1}{2\pi\hbar}\int_{-\infty}^{\infty}\mathrm{d}p\,\mathrm{e}^{-\beta p^2/2m}\,\mathrm{e}^{-\frac{m}{2\beta\hbar^2}(x'-x)^2-\beta[V(x')+V(x)]/2} && \text{(2.7g)}\\
&= \sqrt{\frac{m}{2\pi\beta\hbar^2}}\,\mathrm{e}^{-\frac{m}{2\beta\hbar^2}(x'-x)^2-\beta[V(x')+V(x)]/2}, && \text{(2.7h)}
\end{aligned}$$

where $\mathrm{i}=\sqrt{-1}$, and we have introduced the completeness relation for the momentum eigenstates

$$\int_{-\infty}^{\infty}\mathrm{d}p\,|p\rangle\langle p| = 1 \tag{2.8}$$

and used the relation

$$\langle x|p\rangle = \frac{1}{\sqrt{2\pi\hbar}}\,\mathrm{e}^{\mathrm{i}px/\hbar}. \tag{2.9}$$

Equation 2.7a is not an equality because $\hat{T}$ does not commute with $\hat{V}$ and the error introduced by the approximate commutation is of order β^3 (Tannor, 2007, §11.7.1); it therefore diminishes only in the high-temperature limit. This is of course not the regime in which we are interested in studying, as quantum nuclear dynamical effects are only apparent at low temperatures. Higher-order Trotter algorithms are available which reduce the error but increase the complexity. For certain applications the higher-order methods make computations more tractable (Drozdov, 1998), but for our purposes we choose to retain the simpler form.

In order to calculate the quantum trace efficiently yet accurately, we note that the Boltzmann operator can be split in two and a new complete set of

states inserted over which we integrate, i.e.

$$Q(\beta) = \int_{-\infty}^{\infty} \mathrm{d}x \, \big\langle x \big| \mathrm{e}^{-\beta\hat{H}/2} \, \mathrm{e}^{-\beta\hat{H}/2} \big| x \big\rangle \tag{2.10}$$

$$= \int_{-\infty}^{\infty} \mathrm{d}x \int_{-\infty}^{\infty} \mathrm{d}x' \big\langle x \big| \mathrm{e}^{-\beta\hat{H}/2} \big| x' \big\rangle \big\langle x' \big| \mathrm{e}^{-\beta\hat{H}/2} \big| x \big\rangle, \tag{2.11}$$

where we have used the property that

$$\int_{-\infty}^{\infty} \mathrm{d}x' \big| x' \big\rangle \big\langle x' \big| = 1. \tag{2.12}$$

In fact, we can split the operator into N factors inserting a new set of states each time to give

$$Q(\beta) = \int_{-\infty}^{\infty} \mathrm{d}x_1 \int_{-\infty}^{\infty} \mathrm{d}x_2 \cdots \int_{-\infty}^{\infty} \mathrm{d}x_N \big\langle x_1 \big| \mathrm{e}^{-\beta_N \hat{H}} \big| x_2 \big\rangle \times \big\langle x_2 \big| \mathrm{e}^{-\beta_N \hat{H}} \big| x_3 \big\rangle \cdots \big\langle x_N \big| \mathrm{e}^{-\beta_N \hat{H}} \big| x_1 \big\rangle, \tag{2.13}$$

where $\beta_N = \beta/N$. Taking advantage of the split-operator approximation to the density matrix (Eq. 2.7h) now introduces an error only of order β_N^3 in each case, and the method becomes exact in the limit $N \to \infty$. The partition function can therefore be written

$$Q(\beta) \simeq \left(\frac{m}{2\pi\beta_N \hbar^2} \right)^{N/2} \int \mathrm{d}\mathbf{x} \, \mathrm{e}^{-\beta_N U_N(\mathbf{x})}, \tag{2.14}$$

where $\mathbf{x} = (x_1, \ldots, x_N)$,

$$U_N(\mathbf{x}) = \sum_{i=1}^{N} \left[\frac{m}{2\beta_N^2 \hbar^2} (x_i - x_{i-1})^2 + V(x_i) \right], \tag{2.15}$$

and, as a consequence of representing a quantum trace, the sum is cyclic, i.e. $x_0 \equiv x_N$.

Equation 2.14 is equivalent to a classical partition function of an extended system with Hamiltonian

$$H_N(\mathbf{p}, \mathbf{x}) = \sum_{i=1}^{N} \frac{p_i^2}{2m} + U_N(\mathbf{x}), \tag{2.16}$$

which can be seen to describe a ring, somewhat akin to a necklace, of N

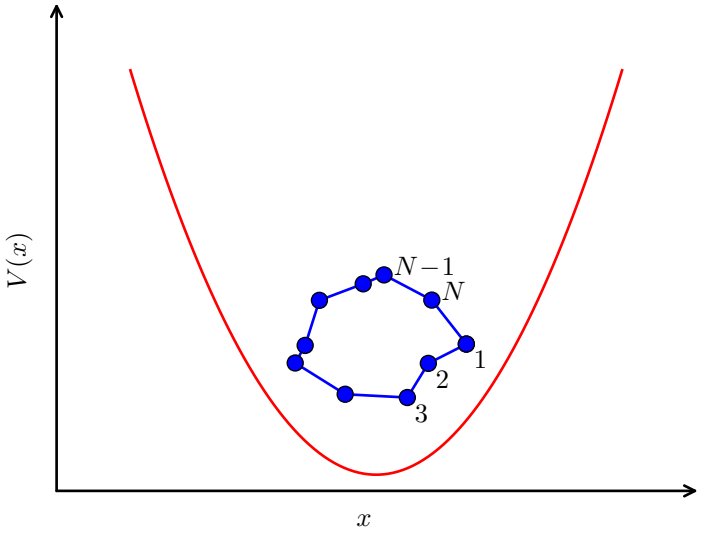

Figure 2.1 – One possible arrangement of $N = 10$ ring-polymer beads (blue blobs) connected by harmonic springs (blue lines) in a potential well (red). In the limit of an infinite number of beads, the classical partition function of the ring polymer is equal to the quantum partition function of the system. NB, the vertical spacing of the beads in this one-dimensional potential is chosen for clarity and has no physical meaning.

"beads", each of mass m, with momentum p_i and connected together by temperature-dependent Hookean springs (with nil equilibrium length), and is known as the "ring polymer" (see Figure 2.1). Describing a quantum system with the ring polymer in this way is known as the classical isomorphism (Chandler and Wolynes, 1981). The external potential $V(x)$ acts on each bead separately, whereas the springs act to pull only neighbouring beads together. With large masses and at high temperatures, the springs become very strong and force the beads to collapse to a single point—the ring polymer then has the dynamics of a classical particle. The springs become easier to stretch for small masses at low temperatures which is the quantum regime. Nonetheless the vibrations are fictitious and describe only the quantum thermodynamics but not the real-time dynamics. In the limit of an infinite number of beads, Eq. 2.14 tends to Feynman's path integral representation of the partition function, and hence the exact result. However, in order to make the method practicable for numerical solution, we choose N to be large enough to achieve results to whatever accuracy is required, and for the purposes of keeping the formulae simple, we assume that it is an even number.

It will be useful to have the forms of the first and second derivatives of the ring-polymer potential:

$$\frac{\partial U_N(\mathbf{x})}{\partial x_i} = \frac{m}{\beta_N^2\hbar^2}(-x_{i+1} + 2x_i - x_{i-1}) + \frac{\partial V(x_i)}{\partial x_i}, \tag{2.17}$$

and

$$G_{ii'} = \frac{1}{m}\frac{\partial^2 U_N(\mathbf{x})}{\partial x_i \partial x_{i'}} = \frac{-\delta_{i+1\,i'} + 2\delta_{ii'} - \delta_{i-1\,i'}}{\beta_N^2\hbar^2} + \frac{\delta_{ii'}}{m}\frac{\partial^2 V(x_i)}{\partial x_i^2}. \tag{2.18}$$

The mass-weighted Hessian matrix is sparse and has the following structure:

$$\mathbf{G} = \frac{1}{\beta_N^2\hbar^2}\begin{pmatrix} \alpha_1 & -1 & \cdot & \cdot & \cdot & -1 \\ -1 & \alpha_2 & -1 & \cdot & \cdot & \cdot \\ \cdot & -1 & \alpha_3 & -1 & \cdot & \cdot \\ \cdot & \cdot & \ddots & \ddots & \ddots & \cdot \\ \cdot & \cdot & \cdot & -1 & \alpha_{N-1} & -1 \\ -1 & \cdot & \cdot & \cdot & -1 & \alpha_N \end{pmatrix}, \tag{2.19}$$

where $\alpha_i = 2 + (\beta_N\hbar)^2 V''(x_i)/m$ and zeros fill the empty spaces.

2.1.1 Harmonic oscillator

We now demonstrate that the ring-polymer formulation gives the exact partition function in the infinite-bead limit for the quantum harmonic oscillator described by the potential

$$V(x) = \frac{1}{2}m\omega_\mathrm{s}^2 x^2. \tag{2.20}$$

In order to calculate the partition function of Eq. 2.14, we can expand the ring-polymer potential as a Taylor series about the stationary point $\mathbf{x} = \mathbf{0}$ giving

$$U_N(\mathbf{x}) = \frac{1}{2}m\sum_{i=1}^{N}\sum_{i'=1}^{N} x_i G_{ii'} x_{i'}. \tag{2.21}$$

It is possible to perform the multidimensional integral over $\mathbf{x}$ as the product of N one-dimensional integrals by first transforming to a basis of the normal modes, as in this basis, the matrix $\mathbf{G}$ is diagonal.* The normal modes are

*See Wales (2003, §2.5.2) for an introduction to normal-mode analysis.

found by an orthogonal transform from the coordinates $\mathbf{x} = (x_1, \ldots, x_N)$ using a transformation matrix with columns equal to the normalized eigenvectors of the (symmetric) mass-weighed Hessian $\mathbf{G}$. The normal modes are associated with frequencies equal to the square root of the eigenvalues. To find the form of these normal modes and their eigenvalues, one can draw a parallel with the Hückel theory calculation of molecular orbitals and energy levels for an even-membered alkene ring, whose Hamiltonian matrix is equivalent to the ring-polymer Hessian, and use the standard results (Salem, 1966, §3.2) for the eigenvectors which represent the normal modes. Because of the presence of degenerate eigenvalues, there is no unique way of specifying the transformation. However, one possible choice is

$$q_0 = \frac{1}{\sqrt{N}} \sum_{i=1}^{N} x_i, \tag{2.22a}$$

$$q_k = \sqrt{\frac{2}{N}} \sum_{i=1}^{N} \sin\left(\frac{2\pi i k}{N}\right) x_i, \qquad k = 1, \ldots, N/2 - 1, \tag{2.22b}$$

$$q_{-k} = \sqrt{\frac{2}{N}} \sum_{i=1}^{N} \cos\left(\frac{2\pi i k}{N}\right) x_i, \qquad k = 1, \ldots, N/2 - 1, \tag{2.22c}$$

$$q_{N/2} = \frac{1}{\sqrt{N}} \sum_{i=1}^{N} (-1)^i x_i. \tag{2.22d}$$

The corresponding normal frequencies are

$$\omega_k = \sqrt{\frac{4}{\beta_N^2 \hbar^2} \sin^2 \frac{|k|\pi}{N} + \omega_\mathrm{s}^2}. \tag{2.23}$$

Note that the normal-mode eigenvectors are independent of ω_s; they will be referred to as the free-ring-polymer normal modes (Craig and Manolopoulos, 2005*a*).

These formulae are also applicable to multidimensional systems (for which see below) and for odd values of N if the $N/2$ mode is removed. Because the vectors $\mathbf{q} \equiv (q_0, q_1, q_{-1}, \ldots, q_{N/2})$ and $\mathbf{x}$ describe the same ring-polymer geometry, even though they use a different representation and hence have different components, we shall use them interchangeably, e.g. $U_N(\mathbf{q}) \equiv U_N(\mathbf{x})$.

Since the Jacobian is unity for a normal-mode transformation, we can

rewrite Eq. 2.14, using Eq. 2.21, as

$$Q_{\mathrm{vib}}(\beta) \simeq \left(\frac{m}{2\pi\beta_N\hbar^2}\right)^{N/2} \int \mathrm{d}\mathbf{q}\, \mathrm{e}^{-\beta_N \sum_k \frac{1}{2} m\omega_k^2 q_k^2} \tag{2.24}$$

$$= \left(\frac{m}{2\pi\beta_N\hbar^2}\right)^{N/2} \prod_k \sqrt{\frac{2\pi}{\beta_N m\omega_k^2}} \tag{2.25}$$

$$= \prod_k \frac{1}{\beta_N\hbar\omega_k}, \tag{2.26}$$

where k runs from $1 - N/2$ to $N/2$. Taking the limit $N \to \infty$ and following the manipulations from Kleinert (2006, §2.10), we obtain

$$Q_{\mathrm{vib}}(\beta) = \frac{1}{2\sinh\left(\beta\hbar\omega_{\mathrm{s}}/2\right)}, \tag{2.27}$$

which is of course the exact result for the partition function of a quantum harmonic oscillator. Equation 2.26, which shows how the vibrational partition function for a ring polymer in a harmonic potential can be calculated, is the main result of this section.

NB, when computing Eq. 2.26, one must be aware of the danger of overflow errors. It is generally safest to use the formula given there rather than the version given in Eq. 2.25.

It is also possible to use the ring-polymer formalism to compute the exact vibrational partition function for a particle in an anharmonic well. However, in this case, an analytic expression is not available and a simulation would have to be carried out in the way described in Chapter 4. Alternatively, one can neglect the effect of the anharmonicity and use the harmonic expression anyway, effectively truncating the Taylor series at second order. This is the approach used in Chapter 3; it introduces an error which is usually small in comparison to the tunnelling effect that we are attempting to describe. For example, the error in the rate of $\mathrm{H} + \mathrm{CH_4}$ at 200 K from taking a harmonic approximation to the reactant partition function was about a factor of three (Bowman et al., 2001).

2.1.2 Translational partition function

As the translational partition function $Q_{\text{trans}}(\beta)$ for an unbounded particle is infinite, the quantity which we wish to compute is the (finite) partition function per unit length. In this section, we derive the partition function for a free ring polymer in one dimension.

The derivation is somewhat similar to that of the harmonic oscillator except that $\omega_{\text{s}} = 0$ and therefore ω_0 is also zero. This means that the integrand along the q_0 mode is no longer Gaussian but constant since this is the unbounded mode. We set the limits of this integral to $-L/2$ to $L/2$ and let L tend to infinity:

$$Q_{\text{trans}}(\beta) = \left(\frac{m}{2\pi\beta_N\hbar^2}\right)^{N/2} \int_{-L/2}^{L/2} \mathrm{d}\mathbf{x}\, \mathrm{e}^{-\beta_N U_N(\mathbf{x})} \tag{2.28}$$

$$= \left(\frac{m}{2\pi\beta_N\hbar^2}\right)^{N/2} \int_{-\sqrt{N}L/2}^{\sqrt{N}L/2} \mathrm{d}q_0 \prod_k{}' \sqrt{\frac{2\pi}{\beta_N m\omega_k^2}} \tag{2.29}$$

$$= L\sqrt{\frac{Nm}{2\pi\beta_N\hbar^2}} \prod_k{}' \frac{1}{\beta_N\hbar\omega_k}, \tag{2.30}$$

where the prime indicates that the zero-frequency mode ($k = 0$) is omitted from the product. Using 1.396.1 from Gradshteyn and Ryzhik (2000), in the special case that $\omega_{\text{s}} = 0$, we obtain the useful equality

$$\prod_k{}' \beta_N\hbar\omega_k = N, \tag{2.31}$$

from which one can compute the translational partition function per unit length,

$$Q_{\text{trans}}(\beta)/L = \sqrt{\frac{m}{2\pi\beta\hbar^2}}, \tag{2.32}$$

which is the exact result for the quantum partition function of a free particle and also holds true for a bounded particle in the classical limit.

We could have derived Eq. 2.30 directly using arguments from standard classical statistical mechanics by separating the N-dimensional ring-polymer system into translational and vibrational factors. In this sense, the reciprocal temperature is β_N and there is one translational degree of freedom, for which the relevant mass is Nm, and $N-1$ classical vibrational modes each contributing $1/\beta_N\hbar\omega_k$. Note that the method includes *vibrational* modes of

the ring polymer even whilst formulating the *translational* partition function, and that the translational factor alone does not reproduce the correct result. This is a consequence of the nature of the classical isomorphism which describes quantum effects by the classical fluctuations of the ring polymer.

2.2 Multidimensional generalization

The molecular systems that we wish to study cannot in general be separated along each degree of freedom to give one-dimensional integrals, but the advantage of the ring-polymer method is that it is easily extended to treat multidimensional systems without considerably increasing the complexity. Within the Born-Oppenheimer approximation, we can separate the electronic from the nuclear motions and introduce the concept of a potential energy surface (PES). For example, a three-dimensional molecule of $f/3$ atoms may be described by a single point in f-dimensional space subject to the Hamiltonian

$$\hat{H} = \sum_{j=1}^{f} \frac{\hat{p}_j^2}{2m_j} + V(\hat{x}_1, \ldots, \hat{x}_f), \tag{2.33}$$

where the coordinates x_j and their conjugate momenta p_j can be chosen in any way such that they span phase space and are orthogonal to each other. The usual choice is: x_1, x_2 and x_3 describe the Cartesian coordinates of atom 1, x_4 to x_6 describe those of atom 2 etc., and m_j is the mass of the atom represented by the j^{th} degree of freedom. $V(x_1, \ldots, x_f)$ is a scalar field which returns the value of the potential energy at the specified geometry.

As before, the ring polymer is represented by N beads and the notation $x_{i,j}$ is introduced to describe the location of the i^{th} bead in the j^{th} dimension. The ring-polymer potential is now defined as

$$U_N(\mathbf{x}) = \sum_{i=1}^{N} \sum_{j=1}^{f} \frac{m_j}{2\beta_N^2 \hbar^2} (x_{i,j} - x_{i-1,j})^2 + \sum_{i=1}^{N} V(x_{i,1}, \ldots, x_{i,f}), \tag{2.34}$$

the gradients are

$$\frac{\partial U_N(\mathbf{x})}{\partial x_{i,j}} = m_j \frac{-x_{i+1,j} + 2x_{i,j} - x_{i-1,j}}{\beta_N^2 \hbar^2} + \frac{\partial V(x_{i,1}, \ldots, x_{i,f})}{\partial x_{i,j}} \tag{2.35}$$

and the Hessian is

$$\frac{\partial^2 U_N(\mathbf{x})}{\partial x_{i,j}\partial x_{i',j'}} = m_j \frac{-\delta_{i+1\,i'} + 2\delta_{ii'} - \delta_{i-1\,i'}}{\beta_N^2\hbar^2}\delta_{jj'} + \delta_{ii'}\frac{\partial^2 V(x_{i,1},\ldots,x_{i,f})}{\partial x_{i,j}\partial x_{i,j'}}. \quad (2.36)$$

The mass-weighted Hessian

$$G_{i,j,i',j'} = \frac{1}{\sqrt{m_j m_{j'}}}\frac{\partial^2 U_N}{\partial x_{i,j}\partial x_{i',j'}} \quad (2.37)$$

will be useful too.

Although we have formulated the multidimensional ring-polymer gradient and Hessian with two and four indices each, it is often easier to think of the gradient as a vector of length Nf and the Hessian as a matrix of size $Nf \times Nf$. This allows us to apply standard optimization and linear algebra routines. The mass-weighted Hessian then has a block structure similar to that shown in Eq. 2.19 with -1 replaced by a submatrix of size $f \times f$ equal to $-\mathbf{1}$ and $\alpha_i = 2 \times \mathbf{1} + (\beta_N\hbar)^2\boldsymbol{\nabla}^2 V(x_{i,1},\ldots,x_{i,f})/\sqrt{\mathbf{m}\mathbf{m}^\top}$, where $\boldsymbol{\nabla}^2 V$ is the Hessian of the PES at a particular geometry.

Each bead describes a "replica" of the system as its position completely defines a geometry of all $f/3$ atoms, and generates a single value of the potential energy including all interatomic forces. The beads are connected to their neighbours with f-dimensional harmonic springs which are stronger in the directions corresponding to heavy masses. Alternatively, one could interpret Eq. 2.34 as describing a N-bead three-dimensional ring polymers on each atom with beads that are only connected to their neighbouring beads on the same atom and the usual atomic interactions are only included between similarly-numbered beads on different atoms. In the author's opinion, the former interpretation is much simpler and will be used as the starting point for all derivations in forthcoming chapters.

2.2.1 Total partition function

The harmonic oscillator and translational partition function formulations are easily extended such that they can be applied to multidimensional systems. When all the beads are collapsed at the bottom of a well, the normal modes are defined as in Eq. 2.22 for each degree of freedom j, and their frequencies

are

$$\omega_{k,j} = \sqrt{\frac{4}{\beta_N^2\hbar^2}\sin^2\frac{|k|\pi}{N} + \zeta_j^2}, \tag{2.38}$$

where ζ_j are the harmonic frequencies of the well (of which some may be zero) calculated as the square roots of the eigenvalues of the mass-weighted Hessian of the PES $\boldsymbol{\nabla}^2 V/\sqrt{\mathbf{m}\mathbf{m}^\top}$. Assuming an even number of beads, k runs from $1 - N/2$ to $N/2$ and j from 1 to f. The same frequencies and normal modes could of course be obtained directly, but less-efficiently, by diagonalizing $\mathbf{G}$ (Eq. 2.37) computed with all the beads collapsed at the minimum of the PES. The transformation of $x_{i,j}$ to normal modes can be computed efficiently using a fast-Fourier transform (FFT) as described in Appendix C.

It is also possible, but difficult, to reformulate ring-polymer methodology for rotational degrees of freedom (Marx and Müser, 1999). However, since in the majority of cases, the rotational spacing will be much smaller than $k_\mathrm{B}T$ and many rotational energy levels will be occupied, the partition function will be close to its equipartition limit such that a fully classical treatment will be good enough. We can modify the classical results (McClelland, 1973, §5.5) for the rotation of a linear molecule to obtain

$$Q_\mathrm{rot}(\beta) = \frac{2I}{\beta\hbar^2} = \frac{2NI}{\beta_N\hbar^2}\prod_{j=1}^{2}\prod_{k}{}' \frac{1}{\beta_N\hbar\omega_{k,j}}, \tag{2.39}$$

where the frequencies $\omega_{k,j}$ describe fluctuations in the direction of the rotational modes and are defined by Eq. 2.38 with $\zeta_1 = \zeta_2 = 0$. The index k runs over all its possible values ($1 - N/2$ to $N/2$) except that, as indicated by the prime, $k = 0$ is excluded. I is the moment of inertia about the centre of mass calculated in the standard way using the minimum-energy geometry.

For a non-linear molecule, the expression is

$$Q_\mathrm{rot}(\beta) = \sqrt{\frac{8\pi\det\mathbf{I}}{\beta^3\hbar^6}} = \sqrt{\frac{8\pi N^3\det\mathbf{I}}{\beta_N^3\hbar^6}}\prod_{j=1}^{3}\prod_{k}{}' \frac{1}{\beta_N\hbar\omega_{k,j}}, \tag{2.40}$$

where ζ_3 is also zero, and $\mathbf{I}$ is the 3×3 moment of inertia tensor calculated about the molecule's centre of mass (McClelland, 1973, §5.5). We have not taken account of the symmetry number in the rotational partition function as this is an inherently quantum factor, which should not be included in the

classical ring-polymer formulation, where the particles are distinguishable. The effect of the symmetry instead manifests itself in a number of identical transition states (see for example §3.4.2).

The formulae for the translational, rotational and vibrational partition functions are multiplied together to obtain an expression for the total partition function. For example, the total partition function per unit volume of a non-linear molecule with three translational, three rotational and $f-6$ vibrational degrees of freedom is

$$Q(\beta) = \left(\frac{NM}{2\pi\beta_N\hbar^2}\right)^{3/2} \sqrt{\frac{8\pi N^3 \det \mathbf{I}}{\beta_N^3\hbar^6}} \prod_{j=1}^{f} {\prod_{k}}' \frac{1}{\beta_N\hbar\omega_{k,j}}, \tag{2.41}$$

where $M = \sum_{j=1}^{f} m_j/3$ is the total mass of the molecule. Only the six zero frequencies $\omega_{0,1}, \ldots, \omega_{0,6}$ are excluded from the product over $\omega_{k,j}$, but all non-zero fluctuations, including those in the $j = 1, \ldots, 6$ degrees of freedom corresponding to translations and rotations, are included. Here, $\mathbf{I}$ is calculated using just one replica of the system and the factor of N^3 introduced accounts for all the beads occupying the same geometry.

We now have all the necessary equations for defining the ring-polymer representation of the quantum partition function. The remainder of this work shows how this formulation can be used to calculate rates (Chapters 3 and 4) and tunnelling splittings (Chapters 5 and 6).

Chapter 3

Ring-Polymer Instanton Rate Theory

In this chapter we shall derive an instanton method for estimating the rate of a chemical reaction starting from the "Im F" premise and following some standard instanton methodology (Coleman, 1977*b*). However, we employ the ring-polymer formulation from the start which greatly simplifies the mathematics and leads to a particularly practical method for locating instantons in multidimensional systems (Richardson and Althorpe, 2009). An equivalent method called harmonic QTST was derived independently by Andersson et al. (2009) and has been used in a number of applications on small gas-phase molecular reactions in the last couple of years since its discovery (Andersson et al., 2011; Meisner et al., 2011; Goumans and Kästner, 2011).

The Im F instanton method follows the ideas of Coleman (1977*a*) and Callan and Coleman (1977) who argued that, within the framework of a semi-classical approximation to quantum field theory, the probability of barrier penetration could be related to the imaginary part of a complex "free energy". Affleck (1981), however, described how the method could be applied to calculate the rate of decay from a metastable state either by thermal activation or tunnelling. Considering the reactants as a metastable states which decay into products by tunnelling through an energy barrier, one can therefore use the Im F method to compute the rates of chemical reactions at low temperature (Benderskii et al., 1994).

Unfortunately, no rigorous derivation for the Im F premise at all tem-

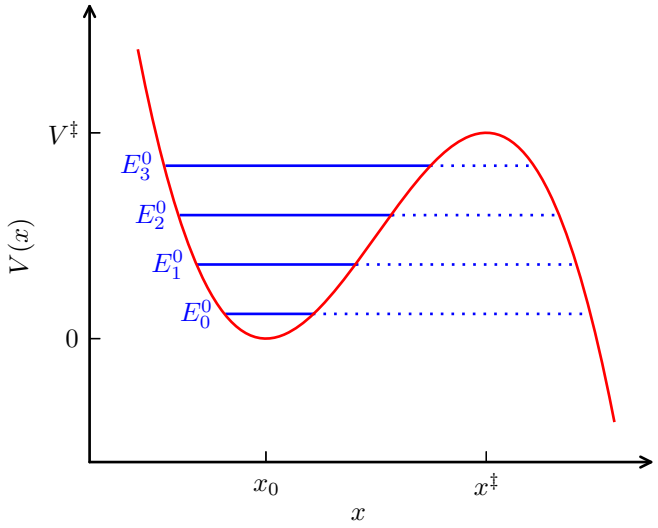

Figure 3.1 – A schematic of a potential (red curve) including a set of metastable states in the vicinity of x_0. The solid blue lines show the energy levels that would be found in a system which could not escape, but which, in reality, leak out through the barrier.

peratures exists, and it is not possible to rigorously evaluate the complex "partition function". Nonetheless, a steepest-descent approximation to an analytic continuation of the partition function can be computed, as we shall discuss below, which leads to an instanton theory which seems to work well at a large range of temperatures and has become a standard and widely-used technique in quantum chromodynamics, field theory and cosmology (Vainshtein et al., 1982).

3.1 Im F rate theory

We follow the derivation of Benderskii et al. (1994, §3.4) to derive the rate of decay of a metastable state. If there were no barrier transmission, a set of bound-state energy levels would exist with energy E_n^0 (see Figure 3.1) and partition function $Q_\mathrm{r}(\beta)$. However, because of tunnelling through the barrier, we can formally represent the energies in complex form (Landau and Lifshitz, 1965, §132),

$$E_n = E_n^0 - \mathrm{i}\hbar\Gamma_n/2. \tag{3.1}$$

This gives the required decay of the states Ψ_n:

$$|\Psi_n(t)|^2 = \left|\Psi_n(0)\,\mathrm{e}^{-\mathrm{i}E_n t/\hbar}\right|^2 \tag{3.2a}$$

$$= \left|\Psi_n(0)\,\mathrm{e}^{-\mathrm{i}E_n^0 t/\hbar}\,\mathrm{e}^{-\Gamma_n t/2}\right|^2 \tag{3.2b}$$

$$= |\Psi_n(0)|^2\,\mathrm{e}^{-\Gamma_n t}, \tag{3.2c}$$

and it is seen that the rate of decay of the n^{th} state is

$$\Gamma_n = -\frac{2}{\hbar}\,\mathrm{Im}\,E_n. \tag{3.3}$$

We introduce a complex "partition function"

$$Q(\beta) = \sum_n \mathrm{e}^{-\beta E_n} \tag{3.4}$$

$$= \sum_n (\cos\beta\hbar\Gamma_n/2 + \mathrm{i}\sin\beta\hbar\Gamma_n/2)\,\mathrm{e}^{-\beta E_n^0}, \tag{3.5}$$

with an associated "free energy"

$$F = -\frac{1}{\beta}\ln Q(\beta), \tag{3.6}$$

and would like to compute $Q(\beta)$ by an analytic continuation of the path-integral expression into the complex plane. Unfortunately, it is not known how to do this rigorously, but as we shall see, we can calculate the leading contribution to the imaginary part using the method of steepest descent.

Assuming it is possible to compute $Q(\beta)$, we could obtain the canonical, Boltzmann-averaged rate as

$$k(\beta) = \frac{1}{Q_{\mathrm{r}}(\beta)}\sum_n \Gamma_n\,\mathrm{e}^{-\beta E_n^0} \tag{3.7}$$

$$= -\frac{2}{\hbar Q_{\mathrm{r}}(\beta)}\sum_n \mathrm{Im}\,E_n\,\mathrm{e}^{-\beta E_n^0} \tag{3.8}$$

$$\approx \frac{2}{\beta\hbar}\frac{\mathrm{Im}\,Q(\beta)}{\mathrm{Re}\,Q(\beta)} = -\frac{2}{\hbar}\,\mathrm{Im}\,F, \tag{3.9}$$

where we have used the real and imaginary parts of Eq. 3.5 with the approximation that $\beta\hbar\Gamma_n/2 \ll 1$. This is valid for low values of n where the decay rates are small such that $\mathrm{Im}\,Q(\beta) \ll \mathrm{Re}\,Q(\beta)$ unless the barrier is asymptotically

low or thin, and the errors associated with higher-n states will be reduced by the Boltzmann weighting. We have also implicitly assumed that the rate is dominated by tunnelling and not by thermal activation taking the system over the barrier. However, at higher temperatures, classical thermodynamic fluctuations dominate, and the expression for the $\operatorname{Im} F$ rate takes a different form (Affleck, 1981), given in Appendix A, and reproduces Wigner's exact expression for a parabolic barrier. This form can describe shallow tunnelling through the top of the barrier, which is approximately parabolic on a short length-scale. The two expressions are equal at $\beta_{\mathrm{c}} = 2\pi/\hbar\omega_{\mathrm{b}}$ where $\mathrm{i}\omega_{\mathrm{b}}$ is the imaginary barrier frequency. This "cross-over" temperature will be seen to be important in the derivation below. The $\operatorname{Im} F$ premise has a well-defined limit at the cross-over temperature, and also in the limit $\hbar\Gamma_0/2 \ll \beta^{-1} \ll E_1^0$ where $k(\beta)$ reduces to Γ_0, the decay rate of the lowest state. For now we shall assume that it also gives a good approximation at temperatures between these two limits, which will be confirmed by the numerical implementations. Equation 3.9 will be our starting point for the instanton-theory derivation.

The problem is how to compute the complex partition function $Q(\beta)$, the real part of which describes the reactant state (and is approximately equal to $Q_{\mathrm{r}}(\beta)$) and the imaginary part the barrier region.* The $\operatorname{Im} F$ approach therefore relates the rate constant to a ratio of the partition functions of the top of the barrier with the reactants in a similar, but not equivalent, way to transition-state theory.

It is also possible to use the theory to treat reactive scattering problems where there is no metastable well but rather a reactive channel with a translational degree of freedom. In this case there would be a continuum of states with decay constants Γ_n. However, as $\operatorname{Im} Q(\beta)$ is based only on the quantum Boltzmann operator in the vicinity of the barrier, one is free to modify the potential elsewhere to create a metastable well and a discrete series of resonances which decay by tunnelling through the barrier as before.

As shown in Chapter 2, the ring-polymer method provides a relatively simple way of computing quantum partition functions, especially when it is possible to perform the integrals analytically. Although the N-dimensional integral for an anharmonic PES is not separable by converting to normal

*A purely imaginary partition function would result from a parabolic potential with $\omega_{\mathrm{s}}^2 < 0$ (cf. Eq. 2.27), and so it is the barrier region of the metastable potential, where the Hessian has a negative eigenvalue, which contributes to the imaginary part of $Q(\beta)$.

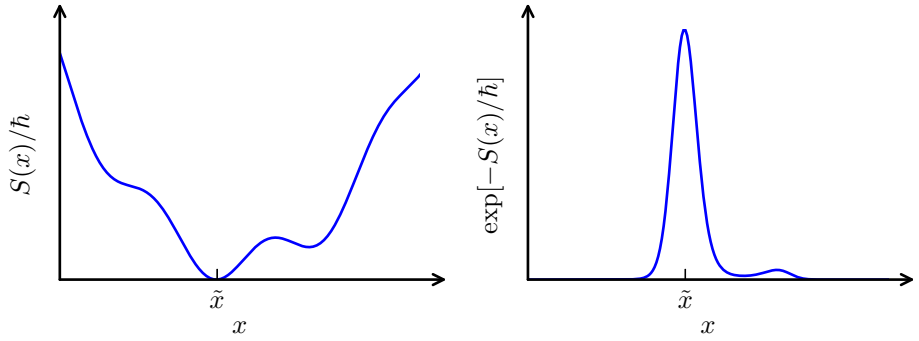

Figure 3.2 – A function of the form $S(x)/\hbar$, as shown on the left, with a minimum at $\tilde{x}$ produces an approximately-Gaussian peak, centred about $\tilde{x}$, when the exponential is taken and $\hbar$ is small. In the steepest-descent method, one uses this approximate function to perform the integral analytically.

modes, we can employ a steepest-descent approximation which greatly simplifies the integrals whilst retaining the majority of tunnelling effect. We shall use these ideas to compute an approximation to $\operatorname{Im} Q(\beta)$ and therefore the rate constant $k(\beta)$ for the one-dimensional case and generalize the treatment to systems of many dimensions in §3.3.

3.1.1 Steepest-descent instantons

In order to compute the integrals in the expression for the ring-polymer partition function of an anharmonic system analytically, we employ the method of steepest descent. The method is based on the principle that a function of the form $\mathrm{e}^{-S(x)/\hbar}$ is dominated by the region in which $S(x)$ is minimal (see Figure 3.2). In order to compute the integral over this function, the method of steepest descent is employed, which in one-dimension can be expressed as

$$\int_{-\infty}^{\infty} \mathrm{d}x\, \mathrm{e}^{-S(x)/\hbar} \approx \int_{-\infty}^{\infty} \mathrm{d}x\, \mathrm{e}^{-\left[S(\tilde{x})+\frac{1}{2}S''(\tilde{x})(x-\tilde{x})^2\right]/\hbar} \tag{3.10}$$

$$= \sqrt{\frac{2\pi\hbar}{S''(\tilde{x})}}\mathrm{e}^{-S(\tilde{x})/\hbar}, \tag{3.11}$$

where $\tilde{x}$ is the minimum of the function $S(x)$ and so $S'(\tilde{x}) = 0$ and $S''(\tilde{x}) > 0$. This approximation becomes exact in the limit $\hbar \to 0$ and is therefore a form

of semi-classical approximation.

In the ring-polymer formulation for the partition function (Eq. 2.14) of the metastable system, there is a minimum in the ring-polymer potential $U_N(\mathbf{x})$ when all the beads are collapsed at x_0. A steepest-descent approximation about this point leads to a harmonic approximation for $Q_\mathrm{r}(\beta)$ which is calculated using the methods of Chapter 2. However, as will become clear, we also need to take a steepest-descent integral about a first-order saddle point in order to obtain $\operatorname{Im} Q(\beta)$.

To find these stationary points, we search for geometries where the ring-polymer gradient (Eq. 2.17) is zero, giving

$$V'(x_i) = m\frac{x_{i+1} - 2x_i + x_{i-1}}{\beta_N^2\hbar^2}, \tag{3.12}$$

which is recognized as a finite-difference approximation to Newton's equation of motion in an inverted potential $-V(x)$ with time steps of $\beta_N\hbar$. This comes as no surprise since the Boltzmann operator $\mathrm{e}^{-\beta\hat{H}}$ can also be thought of as the propagator $\mathrm{e}^{-\mathrm{i}\hat{H}t/\hbar}$ with $\beta\hbar = \mathrm{i}t = \tau$ as first done by Miller (1971).* In imaginary time,

$$\frac{\mathrm{d}x}{\mathrm{d}\tau} = -\mathrm{i}\frac{\mathrm{d}x}{\mathrm{d}t}, \qquad\qquad \frac{\mathrm{d}^2x}{\mathrm{d}\tau^2} = -\frac{\mathrm{d}^2x}{\mathrm{d}t^2}, \tag{3.13}$$

such that the classical equation of motion becomes

$$V'(x) = m\frac{\mathrm{d}^2x}{\mathrm{d}\tau^2} \tag{3.14}$$

with the energy, a constant of motion,

$$E = -\frac{1}{2}m\left(\frac{\mathrm{d}x}{\mathrm{d}\tau}\right)^2 + V(x(\tau)), \tag{3.15}$$

and the Euclidean action along the path $x(\tau)$,

$$S[x(\tau)] = \int_0^{\beta\hbar}\left[\frac{1}{2}m\left(\frac{\mathrm{d}x}{\mathrm{d}\tau}\right)^2 + V(x(\tau))\right]\mathrm{d}\tau. \tag{3.16}$$

We can see that $\beta_N\hbar U_N(\mathbf{x})$ is a finite-difference approximation to the action of a periodic classical trajectory in the inverted potential. Periodic orbits

*This transition to imaginary time is called the Wick rotation.

formed the basis of early applications of instanton theory, but except in one-dimensional systems, were extremely difficult to locate as one has to use trial and error to find the initial conditions with which to "shoot" a particle such that it describes a periodic orbit. Instead, this work uses a much easier method to calculate a discretized orbit, using a standard transition-state search on the ring-polymer potential surface.

There is a trivial solution of Eq. 3.12 where all the beads are located at the position of the barrier maximum, $x_i = x^\ddagger$. The normal-mode frequencies are now

$$\omega_k = \sqrt{\frac{4}{\beta_N^2 \hbar^2} \sin^2 \frac{|k|\pi}{N} - \omega_\mathrm{b}^2}, \tag{3.17}$$

where $\mathrm{i}\omega_b = \sqrt{V''(x^\ddagger)/m}$ is the imaginary barrier frequency. Since in the large-N limit, the lowest three frequencies are

$$\omega_0 = \mathrm{i}\omega_\mathrm{b}, \tag{3.18}$$

$$\omega_{\pm 1} \simeq \sqrt{\frac{4\pi^2}{\beta^2 \hbar^2} - \omega_\mathrm{b}^2}, \tag{3.19}$$

we infer that there is a cross-over temperature T_c below which $\omega_{\pm 1}$ is imaginary, where

$$\beta_\mathrm{c} = \frac{1}{k_\mathrm{B} T_\mathrm{c}} = \frac{2\pi}{\hbar \omega_\mathrm{b}}, \tag{3.20}$$

which is the same cross-over temperature as was seen before. At temperatures above T_c, the solution $x_i = x^\ddagger$ is a stationary point with only one imaginary mode q_0 corresponding to translation of the centroid. However, below the cross-over temperature, this solution has three imaginary modes and the location of the first-order saddle is elsewhere. The new solution $\mathbf{x} = \tilde{\mathbf{x}}$ must be computed numerically and is named the instanton solution. An example of an instanton located by the methods explained in §3.2 is shown in Figure 3.3. The equivalence with periodic orbits in the upside down potential provides a few insights into the geometry of the instanton. We deduce that the beads will be closely spaced near to the turning points and have larger spacings near to the barrier top, and that as the temperature is lowered (i.e. the imaginary time lengthened) and the springs become weaker, the instanton will stretch more into the regions of lower potential.

If the temperature is lowered below $T_\mathrm{c}/2$, a collapsed ring polymer at

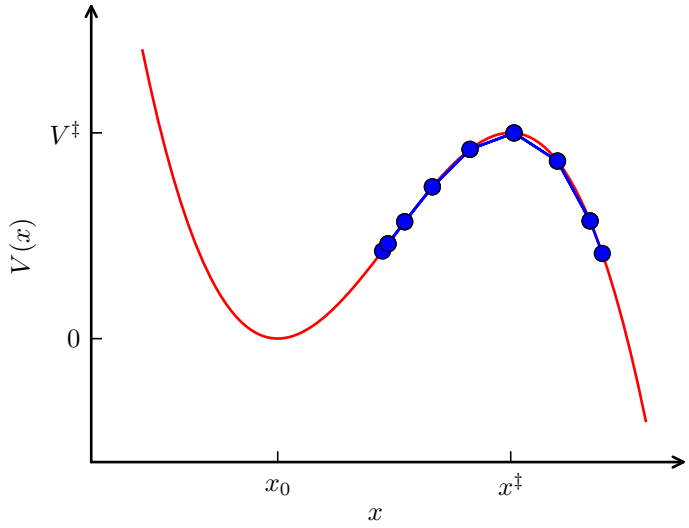

Figure 3.3 – The 16-bead instanton on the metastable barrier for $\beta\hbar\omega_\mathrm{b} = 7$. The beads form a ring which folds back on itself and have been depicted lying on the potential curve but one must remember that the springs only act in the x direction.

the barrier has five imaginary modes and another periodic orbit exists which traces twice around the path of the instanton corresponding to twice the temperature, but this is a third-order saddle point and therefore not appropriate for our needs. The true instanton is very stretched such that it spends most of its orbit in regions of positive curvature and is thus able to remain a first-order saddle point. All temperatures below T_c, where the instanton is not collapsed, are known as the the deep-tunnelling regime.

Below T_c, we expand the ring-polymer potential (Eq. 2.15) in a Taylor series, truncated to second order, about the instanton geometry $\tilde{\mathbf{x}}$ using a new set of normal modes $\{\mathbf{s}_k\}$, where $\mathbf{G}\mathbf{s}_k = \eta_k^2\mathbf{s}_k$ and k runs from 1 to N. The normal modes and eigenvalues η_k^2 are calculated using standard eigenvalue solvers on the (symmetric) mass-weighted ring-polymer Hessian $\mathbf{G}$ calculated at the point $\tilde{\mathbf{x}}$. As expected for such a saddle point, one of the frequencies η_1 is imaginary, but it is also found that η_2 tends to zero in the limit of large N, and so it will not be possible to immediately perform the integral by steepest descent. This is owing to the invariance of the periodic orbit under time translation (Benderskii et al., 1994, §3.5). To see that this is true, we must write the eigenvalue equation in its functional form, equivalent

to the $N = \infty$ case, and postulate that $s_2(\tau) = \partial\tilde{x}(\tau)/\partial\tau$.

$$\lim_{N\to\infty} \mathbf{G}\mathbf{s}_2 \equiv \mathcal{G}s_2(\tau) = -\frac{\partial^2}{\partial\tau^2}\frac{\partial\tilde{x}}{\partial\tau} + \frac{1}{m}V''(\tilde{x}(\tau))\frac{\partial\tilde{x}}{\partial\tau} \tag{3.21a}$$

$$= \frac{1}{m}\frac{\partial}{\partial\tau}\left[-m\frac{\partial^2\tilde{x}}{\partial\tau^2} + V'(\tilde{x}(\tau))\right] \tag{3.21b}$$

$$= 0, \tag{3.21c}$$

which follows from Eq. 3.14 and proves that $s_2(\tau)$ is indeed an eigenfunction with zero eigenvalue. In the finite-N ring-polymer formalism, η_2 is very close to zero, and the mode, which cyclically permutes the beads, is defined as

$$s_2 = \frac{1}{\sqrt{B_N}}\sum_{i=1}^{N}(\tilde{x}_{i+1} - \tilde{x}_i)x_i, \tag{3.22}$$

where the normalization coefficient, chosen to make the transformation to normal modes orthogonal, is

$$B_N = \sum_{i=1}^{N}(\tilde{x}_{i+1} - \tilde{x}_i)^2. \tag{3.23}$$

Moving all x_i from $\tilde{x}_i$ to $\tilde{x}_{i+1}$ adds the term $\sqrt{B_N}$ to s_2 and it takes N such steps to travel all the way around the ring. The integration over the zero-frequency mode should be thus be from 0 to $N\sqrt{B_N}$.

We are now in a position to compute the integrals using the method of steepest descent about the instanton geometry $\tilde{\mathbf{x}}$ in all degrees of freedom except that in the direction of the imaginary mode s_1. Expanding $Q(\beta)$ in the usual way about the saddle point would of course lead to a divergent integral, but we are able to compute its imaginary part with an analytic continuation into the complex plane.

3.1.2 Expression for the rate

Following the arguments of Coleman (1977*b*) we choose to compute $Q(\beta)$ following the integration path shown in Figure 3.4. Using this, we can see that in the steepest-descent limit, $\mathrm{Re}\,Q(\beta) = Q_\mathrm{r}(\beta)$ the reactant partition function, and that $\mathrm{Im}\,Q(\beta)$ can be calculated by integrating along the unstable mode from 0 to ∞ and changing the sign of η_1^2. The Gaussian integral over s_1 therefore gives a factor of a half.

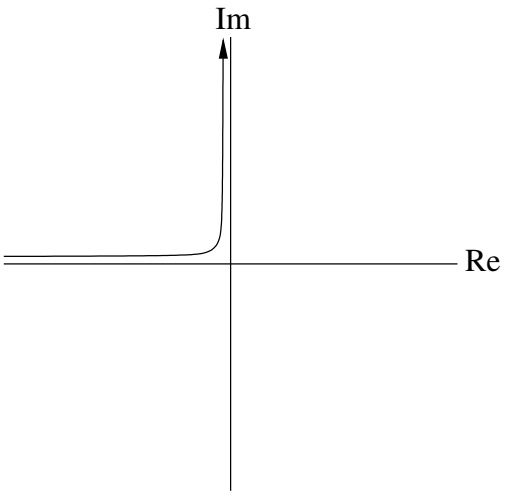

Figure 3.4 – A schematic showing how the partition function $Q(\beta)$ is analytically continued into the complex plane of the unstable mode s_1.

For temperatures below cross-over, steepest-descent integration over all the modes gives

$$\operatorname{Im} Q(\beta) = \frac{N\sqrt{B_N}}{2}\left(\frac{m}{2\pi\beta_N\hbar^2}\right)^{N/2}\prod_k{}' \sqrt{\frac{2\pi}{\beta_N m|\eta_k|^2}}\,\mathrm{e}^{-\beta_N U_N(\tilde{\mathbf{x}})}, \qquad (3.24)$$

where the factor of $N\sqrt{B_N}$ is from the integral over s_2 and the prime indicates that the zero-frequency mode $k = 2$ is omitted from the product. From this and Eq. 3.9, we arrive at the expression for the rate constant

$$k_{\mathrm{inst}}(\beta)Q_{\mathrm{r}}(\beta) = \frac{1}{\beta_N\hbar}\sqrt{\frac{mB_N}{2\pi\beta_N\hbar^2}}\prod_k{}' \left|\frac{1}{\beta_N\hbar\eta_k}\right| \mathrm{e}^{-\beta_N U_N(\tilde{\mathbf{x}})}. \qquad (3.25)$$

This result was independently derived by Andersson et al. (2009) and was proved (Althorpe, 2011) to be equivalent, in the infinite bead limit, to Miller's formulation of semi-classical instanton theory derived from the flux-side correlation function (Miller, 1975),

$$k_{\mathrm{inst}}(\beta)Q_{\mathrm{r}}(\beta) = \left(2\pi\hbar^3\right)^{-\frac{1}{2}}\left|\frac{\mathrm{d}^2 S[\tilde{x}(\tau)]}{\mathrm{d}\beta^2}\right|^{\frac{1}{2}} \mathrm{e}^{-S[\tilde{x}(\tau)]/\hbar}, \qquad (3.26)$$

which lends some support to the $\operatorname{Im} F$ premise.

The reactant partition function is computed using the ring-polymer

techniques of Chapter 2, taking advantage of the expression in Eq. 2.23 to save unnecessary computation. This partition function could perhaps be computed more accurately, but it seems sensible to be consistent and take the same steepest-descent approximations for $Q_{\mathrm{r}}(\beta)$ as for $\operatorname{Im} Q(\beta)$. If we are lucky, there may be some cancellation of errors.

The major error in the method, in addition to the $\operatorname{Im} F$ assumptions, will be caused by taking the steepest-descent approximation. Although this neglects anharmonicity around the instanton geometry, it is not equivalent to taking a harmonic approximation about the barrier, in which case no deep tunnelling would be possible at all. Instead, the anharmonicity of the barrier is included exactly along the instanton pathway. It is for this reason that the method is expected to give a reliable estimate of the quantum rate.

Above the cross-over temperature, the $\operatorname{Im} F$ solution has a different form, as in this regime, it is the classical thermodynamic fluctuations which dominate the rate (Affleck, 1981). It can be shown that when expressed in ring-polymer form with the analytic continuation applied to the steepest-descent integrals, this reduces to Wigner's parabolic tunnelling correction (see Appendix A) and to classical TST if $N = 1$.

3.2 Results

The method was tested for a one-dimensional Eckart barrier (Eckart, 1930) for which the exact quantum dynamics can also be calculated.* This will be useful for testing the validity of the instanton method at a wide range of temperatures. The barrier is defined as

$$V(x) = \frac{A}{1+\exp(-2x/a)} + \frac{B}{\cosh^2(x/a)}. \tag{3.29}$$

*The rate for this system can be computed from the transmission coefficient $T(E)$, for which the analytic form is known (Eckart, 1930) to be

$$T^2(E) = 1 - \frac{\cosh\pi(\delta-\epsilon)+\cosh\pi\zeta}{\cosh\pi(\delta+\epsilon)+\cosh\pi\zeta}, \tag{3.27}$$

where $\eta = 2ma^2$, $\delta = \sqrt{\eta E}$, $\epsilon = \sqrt{\eta(E-A)}$ and $\zeta = \sqrt{4\eta B - 1}$. The thermal rate constant is obtained by (numerically) integrating over the microcanonical rate:

$$k(\beta) = \sqrt{\frac{\beta}{2\pi m}} \int_0^\infty T^2(E)\, \mathrm{e}^{-\beta E}\, \mathrm{d}E. \tag{3.28}$$

Here we choose the parameters to make the barrier symmetric and to facilitate comparison with previous work (Voth et al., 1989): $A = 0$, $2\pi B = 12\hbar\omega_\mathrm{b}$, $m = 1836\, m_\mathrm{e}$ and $a = 0.66047\, a_0$, where ω_b is given by $12\hbar/\pi m a^2$. The reactant has a purely translational partition function for which we use Eq. 2.32.

For one-dimensional systems, the classical rate (see Appendix A) takes a particularly simple form:

$$k_\mathrm{cl}(\beta) Q_\mathrm{r}(\beta) = \frac{1}{2\pi\beta\hbar}\, \mathrm{e}^{-\beta V^\ddagger}, \tag{3.30}$$

where $V^\ddagger = V(x^\ddagger)$ is the height of the barrier relative to the energy of the reactants.

The cross-over temperature at which non-collapsed instantons exist is given by $\beta_\mathrm{c}\hbar\omega_\mathrm{b} = 2\pi$. Above this temperature, the $\mathrm{Im}\, F$ rate is calculated using Wigner's parabolic approximation (Eq. A.8).

Below the cross-over temperature, instantons were computed at a range of temperatures using the "stream-bed walk" algorithm (Nichols et al., 1990) to locate the saddle point on the ring-polymer surface. This is a Newtonian algorithm (Fletcher, 1987) which, at each iteration, computes the gradient and Hessian of the ring polymer, diagonalizes the Hessian, and takes a step in the upwards direction of the lowest normal mode and in the downwards direction of the other modes. The step length is chosen according to the magnitude and sign of the lowest two eigenvalues (see Appendix B).

The method is not very sensitive to the initial geometry of the ring polymer, but it will not work if one starts from the third-order saddle point $x_i = 0$ as here the gradient is zero. In order to provide a strong test for the method, the initial position of each bead was chosen according to a random distribution about the barrier top. The algorithm was found to converge in nearly all cases but needed significantly more iterations for computations with many beads. An instanton calculated by this method is shown in Figure 3.3. A better starting position is provided by the distribution (Rommel et al., 2011)

$$x_i = x^\ddagger + \Delta x \cos\left(2\pi i/N\right), \tag{3.31}$$

where Δx is chosen manually to reduce the computational effort of the optimization.

It is possible, but not necessary, to project-out the zero-frequency mode

Table 3.1 – Convergence of the instanton action S, "zero" frequency η_2 and rate of the symmetric Eckart barrier with respect to the number of beads N at the lowest temperature considered $\hbar\beta\omega_\mathrm{b} = 12$. The exact rate was computed using Eq. 3.28.

N	$S/\hbar$	$\lvert\eta_2\rvert$	$k \times 10^{11}$/a.u.
8	17.192	2(−3)	2.49
16	17.624	6(−4)	3.36
32	17.693	2(−5)	3.40
64	17.711	9(−6)	3.35
128	17.715	4(−6)	3.34
exact	...	0	4.08

from the ring-polymer Hessian $\mathbf{G}$ at each step. In some calculations this was found to improve performance, but in others to increase the number of iterations needed for convergence. Either way, the effects were not drastic.

Converting the instanton geometry shown in Figure 3.3 to the free-ring-polymer normal-mode coordinates (Eq. 2.22) provides a simple way of describing how the ring polymer deforms in the barrier region. This information will be invaluable to the work carried out in the following chapter. The centroid-mode q_0 is zero because the beads are arranged symmetrically about the origin. The modes q_1 and q_{-1} describe the first-order stretch along the x-axis and at least one of them has a relatively large magnitude, whereas the remaining modes have small magnitudes; they describe more irregular patterns which do not generally lead to stationary points.

Table 3.1 shows how the method converges with respect to the number of beads at a relatively low temperature. It can be seen that the rate converges very quickly to give a good approximation to the quantum result, and that, as expected, the action converges and the permutational mode descends in magnitude as the beads become more-closely spaced. Even fewer beads are needed to converge the rate at higher temperatures where the instanton is less stretched.

Figure 3.5 shows how well the calculated instanton rates correspond to the exact results. As expected, the classical results perform very badly at low temperature because they do not allow for tunnelling through the barrier, and underestimate the rate by more than a couple of orders of magnitude. On the other hand, the rates from the instanton method are in good agreement with the exact results. The only significant deviation is near the cross-over

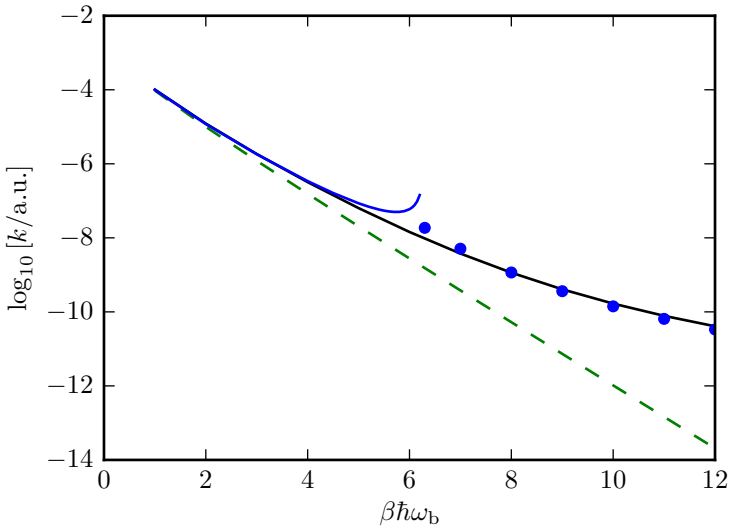

Figure 3.5 – The rates for the Eckart barrier calculated by four different methods are shown. The classical results are depicted by the green dashed line and the exact quantum results in black, the solid blue line shows the results of Wigner's parabolic approximation (above T_c), and the blue blobs indicate the instanton results (below T_c) calculated with 64 beads.

temperature $\beta_c\hbar\omega_\text{b} = 6.28$, where the ring-polymer potential surface becomes flatter and the steepest-descent approximation breaks down. This is not a serious limitation for the method because one can easily calculate β_c in advance to find out whether the approximation will be valid. A better result in these cases could instead be obtained by a Monte Carlo integration or MD simulation to avoid making the steepest-descent approximation as is performed in Chapter 4. The WKB-like instanton method of Kryvohuz (2011) is another way of computing the rates near to the cross-over temperature but which does not require numerical integration.

3.3 Multidimensional generalization

The advantage of the ring-polymer Im F instanton method over exact quantum dynamics, and over the original implementation of the instanton methods based on periodic orbits, is that it remains possible to evaluate the rate computationally even for large systems, without using *ad hoc* reduced-dimensionality models. The extension of the method to the treatment of

multidimensional systems is straightforward and is explained below.

With the classical or $N = 1$ case, there is still only one imaginary frequency $\mathrm{i}\omega_\mathrm{b}$ at saddle point. This is easily calculated via a transition-state search on the PES and by diagonalizing the mass-weighted Hessian at the geometry found. The cross-over temperature can then be determined by the one-dimensional formula Eq. 3.20 but because of corner cutting (Benderskii et al., 1994), instantons may still exist at higher temperatures, and thus, unlike in the one-dimensional case, the value should only be treated as an estimate of the true cross-over temperature. This phenomenon may occur if the symmetry allows because the instanton is free to avoid passing through the transition state if it can reduce its action by doing so. Although in this case it must pass through regions of higher potential energy, the overall path is shortened, especially in the degrees of freedom with large associated masses.

To locate the instanton, we use the same transition-state search as was used in the one-dimensional case, but applied to the multidimensional ring-polymer surface (Eq. 2.34). Although the optimization is performed in Cartesian coordinates, the mass-weighted Hessian (Eq. 2.37) must be used to compute the Nf eigenvalues η_k and eigenvectors $\mathbf{s}_k$, and the steepest-descent integrals are performed in mass-weighted coordinates $y_{i,j} = \sqrt{m_j} x_{i,j}$ (Wales, 2003, §2.5.2).

At at the instanton geometry, there is still one imaginary frequency η_1, one zero-frequency mode,

$$s_2 = \frac{1}{\sqrt{B_N}} \sum_{i=1}^{N} \sum_{j=1}^{f} \sqrt{m_j} (\tilde{x}_{i+1,j} - \tilde{x}_{i,j}) y_{i,j}, \tag{3.32}$$

where the normalization coefficient is

$$B_N = \sum_{i=1}^{N} \sum_{j=1}^{f} m_j (\tilde{x}_{i+1,j} - \tilde{x}_{i,j})^2, \tag{3.33}$$

and the remaining modes have real positive frequencies. The rate is therefore obtained from the expression

$$k_\mathrm{inst}(\beta) Q_\mathrm{r}(\beta) = \frac{1}{\beta_N \hbar} \sqrt{\frac{B_N}{2\pi \beta_N \hbar^2}} \prod_k{}' \left| \frac{1}{\beta_N \hbar \eta_k} \right| \mathrm{e}^{-\beta_N U_N(\tilde{\mathbf{x}})}, \tag{3.34}$$

where k runs from 1 to Nf excluding the zero-frequency mode $k = 2$. Note that if the instanton geometry itself has translational or rotational degrees of freedom, there will be more zero-frequency modes that must also be excluded from the product; they are instead treated in the same way as for the partition function (see §2.2.1). For example, an instanton with three translational and three rotational degrees of freedom would lead to the rate expression

$$k_{\mathrm{inst}}(\beta)Q_{\mathrm{r}}(\beta) = \frac{1}{\beta_N\hbar}\sqrt{\frac{B_N}{2\pi\beta_N\hbar^2}}\left(\frac{NM}{2\pi\beta_N\hbar^2}\right)^{3/2}\sqrt{\frac{8\pi\det\mathbf{I}_N}{\beta_N^3\hbar^6}} \times {\prod_k}'\left|\frac{1}{\beta_N\hbar\eta_k}\right|\mathrm{e}^{-\beta_N U_N(\tilde{\mathbf{x}})}, \quad (3.35)$$

where $\mathbf{I}_N$ is the moment of inertia tensor of the ring polymer treated as an $(Nf/3)$-atom "super-molecule" in three-dimensional space and reduces to $N\mathbf{I}$ if the beads are collapsed.

Miller's (1975) formulation in the multidimensional case is

$$k_{\mathrm{inst}}(\beta)Q_{\mathrm{r}}(\beta) = \left(2\pi\hbar^3\right)^{-\frac{1}{2}}\left|\frac{\mathrm{d}^2 S[\tilde{\mathbf{x}}]}{\mathrm{d}\beta^2}\right|^{\frac{1}{2}}\prod_{j=1}^{f-1}\frac{1}{2\sinh\left(u_j/2\right)}\,\mathrm{e}^{-S[\tilde{\mathbf{x}}]/\hbar}, \quad (3.36)$$

where u_j are the stability parameters of the instanton orbit (Gutzwiller, 1971), and has also been shown to be equivalent to the $\mathrm{Im}\,F$ version in the $N \to \infty$ limit (Althorpe, 2011).

3.4 Example calculations

Here we apply the multidimensional ring-polymer instanton method to calculate the temperature dependence of the rate constant for three different reactions. The first system studied is the collinear reaction

$$\mathrm{H_A} + \mathrm{H_BH_C} \rightarrow \mathrm{H_AH_B} + \mathrm{H_C},$$

using the BKMP2 surface (Boothroyd et al., 1991, 1996; Duchovic et al., 2001–), for which exact quantum results calculated by wave packet propagation are available. The rates of hydrogen exchange in the water dimer and trimer are also computed which are systems are too large for exact quantum

calculations.

3.4.1 Collinear $\mathbf{H + H_2}$

This reaction has been treated as a test case by many methods as it is the simplest example of a chemical reaction. A system of three atoms constrained to move along line can be reduced to a two-dimensional problem by removing the degree of freedom related to the centre-of-mass. Computations were carried-out in Jacobi coordinates (R, r), for which

$$R = \tfrac{1}{2}(x_{\mathrm{B}} + x_{\mathrm{C}}) - x_{\mathrm{A}}, \qquad m_R = \tfrac{2}{3}m_{\mathrm{H}}, \tag{3.37}$$

$$r = x_{\mathrm{C}} - x_{\mathrm{B}}, \qquad m_r = \tfrac{1}{2}m_{\mathrm{H}}, \tag{3.38}$$

where x_{A} is the position of the $\mathrm{H_A}$ atom etc., and m_{H} is the mass of a hydrogen atom.

The reactant partition function (per unit length) is a product of a translational part and a vibrational part:

$$Q_{\mathrm{r}}(\beta) = \sqrt{\frac{Nm_R}{2\pi\beta_N\hbar^2}} \prod_{j=1}^{2} \prod_{k}{}' \frac{1}{\beta_N\hbar\omega_{k,j}}, \tag{3.39}$$

where ω_k is defined as in Eq. 2.38 with $\zeta_1 = 0$ and $\zeta_2 = 4404$ cm^{-1}. The latter is the frequency of vibration between atoms B and C when A is far away and is the only non-zero frequency of the Hessian calculated at the point found by minimizing $V(R, r)$ with respect to r in the limit $R \to \infty$.

As there are only two dimensions, it was easy enough to compute the Hessian by finite-differences at each step in the calculation and the stream-bed walk (Nichols et al., 1990) was again used to find the transition state and the instanton geometry. The cross-over temperature estimated by Eq. 3.20 was 345 K but actually, because of corner-cutting, instantons were found up to 348 K. One instanton geometry calculated is shown in Figure 3.6 and illustrates this concept—the instanton pathway does not pass though the classical transition state. This had been predicted by Marcus and Coltrin (1977), but the advantage of the instanton method is that it is able rigorously to find the tunnelling path without *ad hoc* assumptions. As the temperature is raised, however, the pathway shrinks until at T_{c}, the beads collapse onto a single point at the saddle point of the PES.

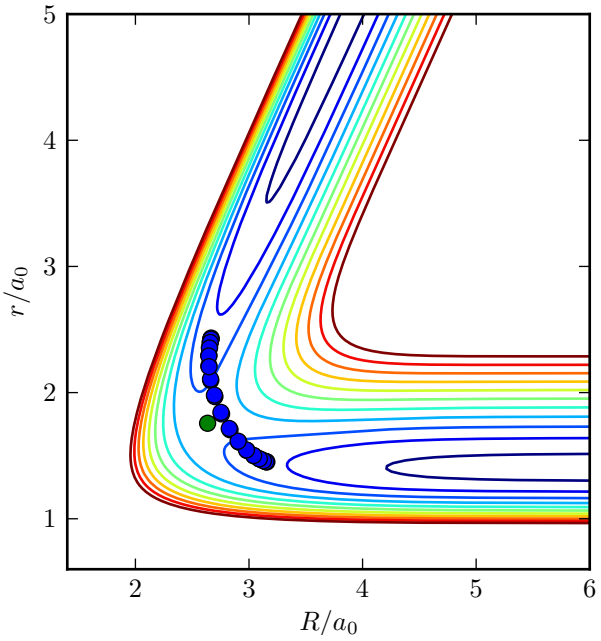

Figure 3.6 – The 32-bead instanton geometry at 240 K for the collinear $H + H_2$ reaction is shown by the blue beads, whereas the $N = 1$ (classical) transition state is marked by the green circle. The potential surface is represented by isoenergetic contours with a spacing of $6\,\mathrm{m}E_\mathrm{h}$.

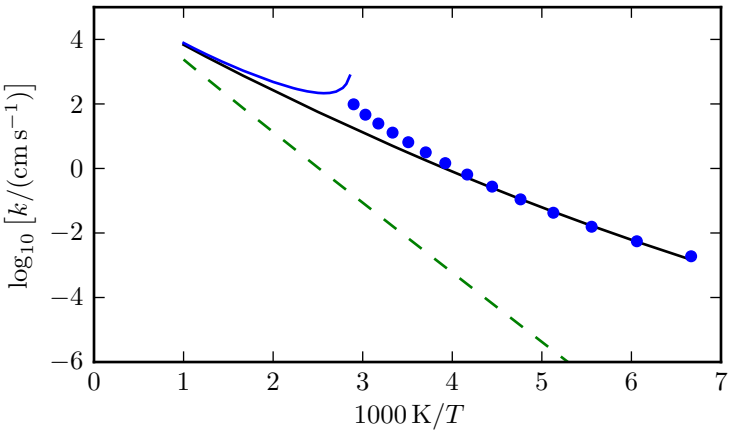

Figure 3.7 – The rates for collinear $H + H_2$ calculated by three different methods are shown. The green dashed line depicts the classical harmonic TST results, the black line depicts the quantum results calculated by wave packet propagation, and the blue blobs depict the ring-polymer instanton results which used 128 beads.

As one can see from Figure 3.7, the instanton results perform very well at low-temperature where the classical TST is out by many orders of magnitude. However, as in the previous example, there is a discrepancy near the cross-over temperature owing to the flattening of the ring-polymer potential.

The calculations performed on the Eckart barrier in §3.2 and on this hydrogen-exchange reaction have shown that the instanton method produces results in good agreement with exact methods for a wide range of temperatures. Armed with this knowledge, we can use it to study systems too large to be for exact treatments to be possible.

3.4.2 Water dimer

The rate of bimolecular hydrogen exchange in the water dimer has been studied by Wang et al. (2010) using the HBB2 water dimer potential (Shank et al., 2009), which is described in §6.2.1. They computed the rate using standard transition-state theory with a tunnelling correction based on a one-dimensional calculation along the imaginary mode of the saddle point. It is not necessary for the instanton method to make this *a priori* separation of degrees of freedom, and we can thus test whether their assumption was correct by comparing the instanton results with those of the one-dimensional method, and if not, the instanton calculations will provide a more accurate result.

For this particular reaction, the reactant state is that of two separate unbounded water molecules, both of which have translational, rotational and vibrational degrees of freedom. To compute the reactant partition function $Q_{\mathrm{r}}(\beta)$, the minimum geometry of a water molecule was found. The 9×9 Hessian at that point has 6 zero eigenvalues, but as there are two identical molecules, each eigenvalue forms a pair to give a set of 18 eigenvalues of which 12 are zero. All 18 frequencies ζ_j are used to compute the $18N$ values of $\omega_{k,j}$ using Eq. 2.38, from which the 12 zero-frequency modes are extracted before computing the partition function using the method described in §2.2.1 with M as the mass of one water molecule and $\mathbf{I}$ its moment of inertia.

It is found that there are two transition states on the potential energy surface with symmetries C_{2h} and C_{2v} which describe different mechanisms of the reaction (Wang et al., 2010). Both are arranged with the oxygen and one hydrogen atom from each molecule forming a rhombus and with the remaining two hydrogen atoms in either a *trans* or *cis* configuration.

Computational details

The potential energy surface is a lot more expensive than those used in the previous examples, and because neither analytical gradients nor Hessians were not available from the routines, it was not practical to use the stream-bed walk algorithm to compute the stationary points. Instead, numerical gradients were calculated using finite-differences and the limited-memory Broyden-Fletcher-Goldfarb-Shanno (L-BFGS) method (Zhu et al., 1997) implemented in SciPy (Jones et al., 2001–) was used to locate minima and the Hessian-update scheme of Bofill (1994) to locate the saddle points. Neither of these methods needs to compute the Hessian at each step as it is instead estimated from the values of the potential and gradient at previous iterations (see Appendix B). This significantly reduces the amount of computation per iteration, and even if the total number of iterations is increased slightly, overall these methods are far more efficient (Rommel et al., 2011).

At least a two-fold improvement in efficiency is quickly gained by modifying the function given in Eq. 2.34. Since the instanton geometry always describes a trajectory which retraces its path between the turning points, half of the beads will lie on top of the other half such that it will not necessary to calculate the potential and gradient for all the beads. Effectively, we can locate stationary points on the object function

$$U_N(\mathbf{x}) = \sum_{i=1}^{N/2-1} \sum_{j=1}^{f} \frac{m_j}{\beta_N^2 \hbar^2} (x_{i+1,j} - x_{i,j})^2 + \sum_{i=1}^{N/2} 2V(x_{i,1}, \ldots, x_{i,f}). \quad (3.40)$$

We call the $N/2$ beads a half ring polymer and its stationary-point geometry a half instanton. In this representation, the Hessian is banded and can potentially greatly speed-up the optimization (see Appendix B). Using this improvement, the fluctuation matrix can be constructed more quickly—the $f \times f$ submatrices need only be calculated for half of the beads—but the full $Nf \times Nf$ matrix must still be diagonalized because we must still include all the fluctuation modes.

We expect the bottleneck for such computations to be in the calculation of the PES, and the method is easily parallelized such that the potential and gradient for each bead is computed on separate CPUs.

A good initial geometry is provided by (Rommel et al., 2011)

$$x_{i,j} = x_j^{\ddagger} + \Delta x \, z_j \cos(\pi i / N), \tag{3.41}$$

where $(z_1, \ldots, z_f)$ is the unstable eigenvector of the (*not* mass-weighted) Hessian at the transition state, and again Δx is chosen manually to reduce the computational effort of the optimization.

In order to compute instantons efficiently with large numbers of beads, the solutions from previous calculations were used to provide good initial guesses. First, a ring polymer with N beads is formed by folding the converged half instanton back on itself. Then the geometry can be converted to normal-modes coordinates $\tilde{\mathbf{q}}$ using an FFT routine and n extra modes added each with nil values. The geometry $\tilde{\mathbf{q}}$ will have to be renormalized by multiplying by $\sqrt{(N+n)/N}$ so that when it is transformed back to Cartesian coordinates, one has an instanton which traces the original path but with a higher-density of beads. The half instanton is easily extracted from this ring polymer by removing the doubled-back beads and is used to restart the transition-state search.

Results

Figure 3.8 shows an instanton calculated for each of the mechanisms studied. The *trans* instanton has a lower action than that of the *cis* instanton and so the *trans* mechanism dominates. As is usual in classical TST, the rate of the reaction is calculated as a sum over the rates of each mechanism. In fact, owing to permutations of the atoms, but enforcing a particular hydrogen to be exchanged, there are four equivalent saddle points for each of these two mechanisms and so the overall rate is multiplied by 4.

The rates computed by the instanton method are shown in Figure 3.9 for the reactions in two isotopic forms. As expected, the TST results are almost equivalent for the deuterated case because the barrier height is unchanged. However, the instanton method correctly finds that the rate of the deuterated reaction is lower, because of the lessening of quantum effects for larger masses. These results agree fairly well with those calculated by Wang et al. (2010) and we can therefore say that in this case, the one-dimensional approximation that they used was acceptable.

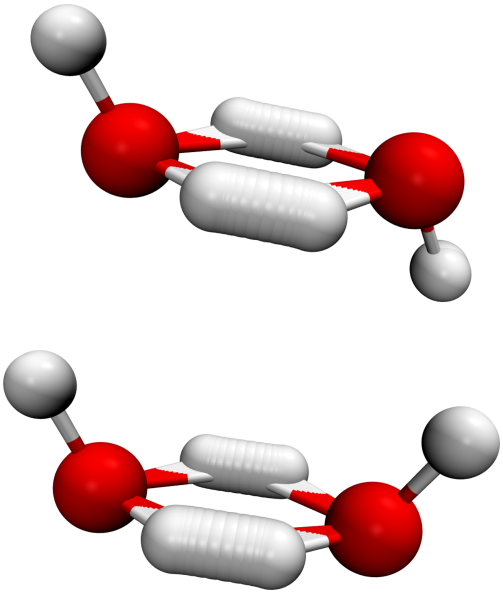

Figure 3.8 – A depiction of the 32-bead instantons for hydrogen exchange in $(H_2O)_2$ at 300 K, showing the *trans* (upper) and *cis* (lower) mechanisms. The geometries of each bead are printed overlapping one another.

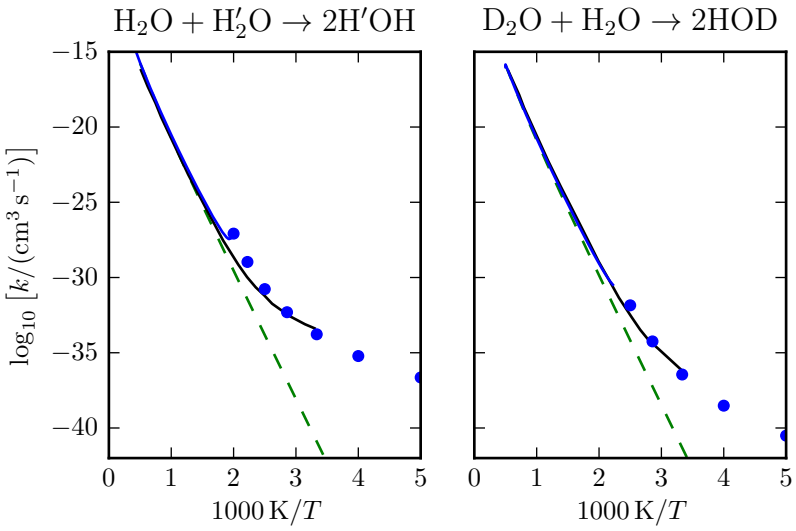

Figure 3.9 – The bimolecular reaction rate for hydrogen exchange in the water dimer. The dashed green line shows the Eyring TST results, the blue line the parabolic approximation and blue blobs the instanton results. For comparison, the results of Wang et al. (2010) using their one-dimensional potential $V(Q_{im})$ are shown in black.

3.4.3 Water trimer

As a final example of the use of the instanton method for calculating reaction rates, results are presented for hydrogen transfer in the water trimer, for which the minimum geometry is a triangular arrangement of water molecules (see Figure 6.5). Unlike in the previous example, it is the unimolecular reaction which is studied: a concerted triple hydrogen motion, simultaneously breaking and forming three covalent bonds.

This work was inspired by the calculations of Loerting et al. (1998) who used one-dimensional methods along two different tunnelling pathways chosen *a priori* to compute the rate. One pathway followed the minimum-energy path and the other took a straight-line path between the reactants and products. Owing to the imprecise nature of the chosen pathway, they received results which varied by many orders of magnitude. However, the instanton method automatically chooses the appropriate pathway and should return a more trustworthy value.

An unpublished trimer potential (Wang and Bowman, 2011) based on MP2/aVTZ calculations was used to describe the system. This is able to describe the breaking and forming of hydrogen bonds, unlike the PES described in §6.3.1. This PES is not equivalent to that used by Loerting et al. (1998) but does seem to be quite similar as is shown in Table 3.2.

The reactant partition function for the unimolecular system is calculated as in Eq. 2.41, and the computational details were equivalent to those used for the water dimer. An instanton for this system is depicted in Figure 3.10. The calculated rates are depicted in Figure 3.11 and fall somewhere between the two extremal values calculated by Loerting et al. (1998).

Table 3.2 – Properties of the minimum and stationary point on the water trimer surface.

Property	MP2/6-311++G(3pd,3df)[a]	PES[b]
Barrier [kcal/mol]	26.99	25.88
Min ZPE [kcal/mol]	46.16	46.02
TS ZPE [kcal/mol]	42.08	42.36
Imaginary Frequency [cm^{-1}]	1833i	1795i

[a] From Loerting et al. (1998).
[b] Using the potential of Wang and Bowman (2011).

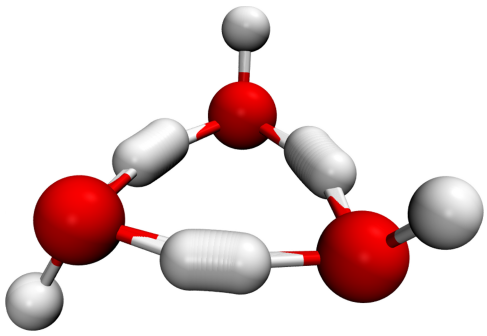

Figure 3.10 – The 32-bead instanton for the concerted proton transfer in water trimer at 300 K.

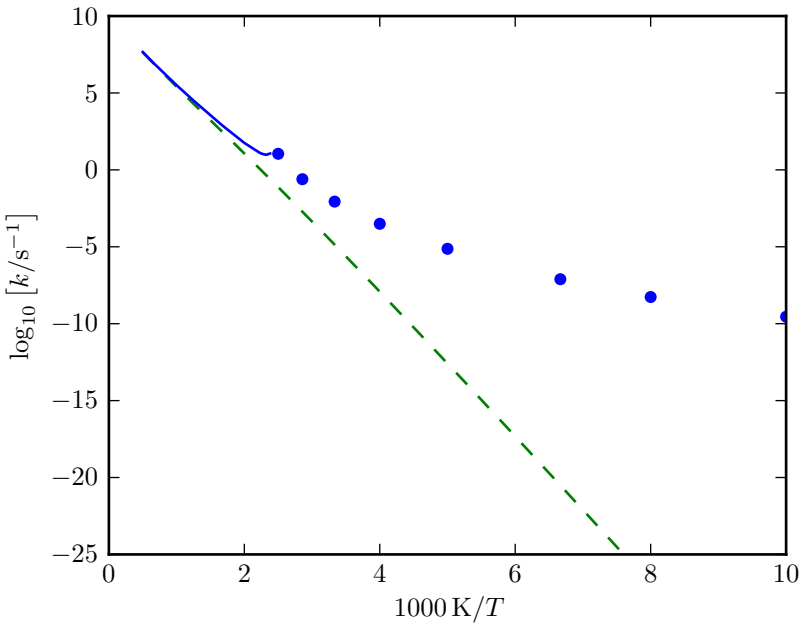

Figure 3.11 – The reaction rate for concerted hydrogen transfer in the water trimer. Results computed using 64 beads.

Chapter 4

Connection Between Ring-Polymer Molecular Dynamics and Instanton Theory

It is possible to show that there is a link between RPMD rate theory in the deep-tunnelling regime and the $\mathrm{Im}\,F$ instanton approach described in the previous chapter. We derive this result by defining a TST version of RPMD, using a conical dividing surface in the ring-polymer space, which is in turn related to a free-energy version of $\mathrm{Im}\,F$ theory within a factor of order unity. This solves the long-standing question of why RPMD performs so well for low-temperature rate calculations (Richardson and Althorpe, 2009).

4.1 Ring-polymer molecular dynamics

The method of RPMD can be used to approximate quantum-dynamical properties, while being based simply on the classical mechanics of ring polymers. It therefore scales well with system size such that it has been possible to apply the method to the computation of rate constants for both gas- and condensed-phase reactions (Collepardo-Guevara et al., 2008, 2009; Suleimanov et al., 2011).

It was noted in §2.1 that the ring-polymer partition function has the form of a classical partition function in an extended phase space $(\mathbf{p}, \mathbf{x})$. In

order to sample this configuration space efficiently, the beads can be made to follow classical trajectories subject to the Hamiltonian given in Eq. 2.16. Because these dynamics preserve the quantum Boltzmann distribution, this method has often been used in calculations of static equilibrium properties (Chandler and Wolynes, 1981; Parrinello and Rahman, 1984). However, the dynamics of the ring polymers have no obvious connection with the exact quantum dynamics described by the time-evolution operators $\mathrm{e}^{\pm \mathrm{i}\hat{H}t/\hbar}$, and for example, interference effects are completely neglected because there is no phase information.

Nevertheless, the *Ansatz* of the RPMD method is to take the artificial classical dynamics literally and to use them to approximate quantum-mechanical real-time Kubo-transformed correlation functions (Craig and Manolopoulos, 2004). This procedure is of course exact in the $t \to 0$ limit where real-time dynamics are suppressed and the statistics of the quantum Boltzmann operator $\mathrm{e}^{-\beta\hat{H}}$ is captured exactly as described in Chapter 2, but at longer times, it cannot be derived rigorously. However, there are a number of arguments which support its validity. In the high-temperature limit, where the beads collapse to a single point, classical mechanics is reproduced such that the theory gives the correct result. A real-time correlation function calculated by the RPMD approach has the same symmetry properties as the exact Kubo-transformed correlation function, i.e. they are both real and even functions of t. In a harmonic potential, the ring-polymer formulation of a correlation function for which at least one of the two operators is linear is also exact, and it is seen numerically that it is a good approximation for short times in anharmonic potentials.

In particular, the dynamics of ring polymers seem to yield good approximations to the Kubo-transformed flux-side correlation function and can therefore be used, in the long-time limit, to compute approximate thermal rate constants. Despite the non-linearity of both the flux and the side operators, it has been shown that the RPMD method gives the exact rate for a parabolic barrier at all temperatures for which a rate can be defined (Craig and Manolopoulos, 2005*a*). In this formulation, the calculated rate is independent of dividing surface and can be expected to be a good approximation in the shallow-tunnelling regime, i.e. for tunnelling through the top of the barrier (which is nearly parabolic), as also has been shown numerically. The theory also appears surprisingly good for obtaining rates in the

deep-tunnelling regime despite no long-time quantum coherence effects being included. Because of the dividing-surface independence in the long-time limit, the method was made more efficient without loosing accuracy by employing a centroid- rather than a bead-pinned form (Craig and Manolopoulos, 2005*b*), such that the short-time limit is equal to the centroid-based QTST of Voth, Chandler and Miller (1989). RPMD, however, systematically improves upon these centroid-based rate theories for asymmetric barriers at all temperatures, and it was noticed that the error in the RPMD method only increased linearly as a function of $1/T$, although no justification could, at the time, be given for such a good result. In this chapter, a link is provided between RPMD and $\mathrm{Im}\, F$ theory which provides a justification for the use of RPMD rate theory in the deep-tunnelling regime and solves this mystery.

Here, we consider only one-dimensional systems, but all the formulae could be generalized for systems with more degrees of freedom. The definition of the RPMD rate constant is equivalent to that of a formulation of classical rate theory in the extended phase space of the ring polymers,

$$k_{\mathrm{RPMD}}(\beta)Q_{\mathrm{r}}(\beta) = \lim_{t\to\infty} \frac{1}{(2\pi\hbar)^N} \int \mathrm{d}\mathbf{p} \int \mathrm{d}\mathbf{x}\, \mathrm{e}^{-\beta_N H_N(\mathbf{p},\mathbf{x})} \delta[\sigma(\mathbf{x})] v_\sigma(\mathbf{p},\mathbf{x}) h[\sigma(\mathbf{x}_t)], \tag{4.1}$$

where

$$v_\sigma(\mathbf{p},\mathbf{x}) = \frac{\mathrm{d}\sigma(\mathbf{x})}{\mathrm{d}t} = \frac{1}{m}\sum_{i=1}^{N} \frac{\partial\sigma(\mathbf{x})}{\partial x_i} p_i. \tag{4.2}$$

The term $\delta[\sigma(\mathbf{x})]v_\sigma(\mathbf{p},\mathbf{x})$ describes the flux of ring polymers through a dividing surface $\sigma(\mathbf{x}) = 0$ at initial time $t = 0$, $\sigma(\mathbf{x})$ is known as the reaction coordinate, and the Heaviside step function $h[\sigma(\mathbf{x}_t)]$ picks out the real-time trajectories for which the ring polymer ends on the product side of the reaction $\sigma(\mathbf{x}) > 0$ and discards those which do not. Like the classical rate theory on which it is based, $k_{\mathrm{RPMD}}(\beta)$ is invariant with respect to changes in the position and form of dividing surface as long as the surface correctly separates products and reactants in the long-time limit. However, a reaction coordinate which follows the centroid of the beads, i.e. $\sigma(\mathbf{x}) = \bar{q} - \sigma_0$, has almost always been chosen in previous implementations since it was shown to be far more efficient that the original bead-pinned version (Craig and Manolopoulos, 2005*b*). The location of the dividing surface along this coordinate is determined by the parameter σ_0, and the centroid coordinate $\bar{q} = \frac{1}{N}\sum_{i=1}^{N} x_i$ is related to the zeroth normal-mode coordinate by the simple

relationship $\bar{q} = q_0/\sqrt{N}$. However, a more general form of the dividing surface will be used in this work, which systematically improves the short-time limit of the RPMD rate, encourages faster convergence, and provides a platform from which it is possible to make clear a justification for the method.

4.2 Ring-polymer transition-state theory

In order to show the relationship between RPMD and the $\mathrm{Im}\, F$ rate theory, it will be necessary to consider a TST-type approximation to Eq. 4.1 which we name ring-polymer transition-state theory (RPTST) (Richardson and Althorpe, 2009),

$$k_{\mathrm{RPTST}}(\beta)Q_{\mathrm{r}}(\beta) = \frac{1}{(2\pi\hbar)^N}\int \mathrm{d}\mathbf{p}\int \mathrm{d}\mathbf{x}\, \mathrm{e}^{-\beta_N H_N(\mathbf{p},\mathbf{x})}\delta[\sigma(\mathbf{x})]v_\sigma(\mathbf{p},\mathbf{x})h[v_\sigma(\mathbf{p},\mathbf{x})], \tag{4.3}$$

in which $h[\sigma(\mathbf{x}_t)]$ is approximated by its $t \to 0^+$ limit, $h[v_\sigma(\mathbf{p},\mathbf{x})]$. We know from classical rate theory that $k_{\mathrm{RPTST}}(\beta)$ will depend exponentially strongly on the form of the dividing surface and that it provides an upper bound to $k_{\mathrm{RPMD}}(\beta)$. The transmission coefficient, or dynamical correction factor, is defined as

$$\kappa_{\mathrm{trans}}(\beta) = \frac{k_{\mathrm{RPMD}}(\beta)}{k_{\mathrm{RPTST}}(\beta)} \leq 1, \tag{4.4}$$

and in order that RPTST give a good approximation to the RPMD rate, the dividing surface $\sigma(\mathbf{x})$ should be chosen such that $\kappa_{\mathrm{trans}}(\beta)$ is as close as possible to unity.

These concepts are already well-established as the RPMD rate can be calculated by any classical rate method. To date, a two step Bennett-Chandler approach (Frenkel and Smit, 1996, §16.2) has been used, i.e. $k_{\mathrm{RPTST}}(\beta)$ is computed with a centroid-based dividing surface followed by the propagation of trajectories starting from this dividing surface to obtain $\kappa_{\mathrm{trans}}(\beta)$ (Collepardo-Guevara et al., 2009). However, this dividing surface is not necessarily optimal, and if we choose $\sigma(\mathbf{x})$ sufficiently well, it may not be necessary to perform the calculation of the transmission coefficient at all.

If the dividing surface is chosen to be $\sigma(\mathbf{x}) = \bar{q}$, it can be shown that $k_{\mathrm{RPTST}}(\beta)$ is equivalent to the method of Voth, Chandler and Miller (1989). To prove this, we transform the momenta to normal-mode coordin-

ates $\mathbf{w} = (w_0, w_1, w_{-1}, \ldots, w_{N/2})$ using the same transformation as was used for the positional coordinates in Eq. 2.22, such that $v_\sigma = \bar{w}/m$ where $\bar{w} = \frac{1}{N}\sum_{i=1}^{N} p_i$ is the momentum of the centroid. This gives

$$\begin{aligned} k_{\mathrm{RPTST}}(\beta)Q_{\mathrm{r}}(\beta) &= \frac{1}{(2\pi\hbar)^N}\int \mathrm{d}\mathbf{w}\int \mathrm{d}\mathbf{x}\, \mathrm{e}^{-\beta_N H_N(\mathbf{p},\mathbf{x})}\delta[\bar{q}]\frac{\bar{w}}{m}h\Big[\frac{\bar{w}}{m}\Big] \\ &= \frac{1}{(2\pi\hbar)^N}\int \mathrm{d}\mathbf{w}\frac{w_0}{m\sqrt{N}}h[w_0]\mathrm{e}^{-\beta_N\sum_k w_k^2/2m}\int \mathrm{d}\mathbf{x}\, \mathrm{e}^{-\beta_N U_N(\mathbf{x})}\delta[\bar{q}] \\ &= \sqrt{\frac{1}{2\pi m\beta}}\left(\frac{m}{2\pi\beta_N\hbar^2}\right)^{N/2}\int \mathrm{d}\mathbf{x}\, \mathrm{e}^{-\beta_N U_N(\mathbf{x})}\delta[\bar{q}], \end{aligned} \tag{4.5}$$

where we have made use of the relation

$$\int_{-\infty}^{\infty}\mathrm{d}p\,\frac{p}{m}h[p]\mathrm{e}^{-\beta_N p^2/2m} = \frac{1}{\beta_N}. \tag{4.6}$$

More generally, but assuming that the reaction coordinate can be written as a normalized linear combination of coordinates, i.e. $\sigma(\mathbf{x}) = c_i x_i$, where $\sum_{i=1}^{N} c_i^2 = 1$,* such that the Jacobian of the transformation is unity, the RPTST rate is

$$\begin{aligned} k_{\mathrm{RPTST}}(\beta)Q_{\mathrm{r}}(\beta) &= \frac{1}{(2\pi\hbar)^N}\left(\frac{2\pi m}{\beta_N}\right)^{\frac{N-1}{2}}\frac{1}{\beta_N}\int \mathrm{d}\mathbf{x}\, \mathrm{e}^{-\beta_N U_N(\mathbf{x})}\delta[\sigma(\mathbf{x})] \\ &= \sqrt{\frac{1}{2\pi m\beta_N}}\left(\frac{m}{2\pi\beta_N\hbar^2}\right)^{N/2}\int \mathrm{d}\mathbf{x}\, \mathrm{e}^{-\beta_N U_N(\mathbf{x})}\delta[\sigma(\mathbf{x})], \end{aligned} \tag{4.7}$$

which is the form that we shall employ.

4.3 Harmonic RPTST rate

In the same way that the steepest-descent approximation was applied to the $\mathrm{Im}\,F$ rate in Chapter 3, a harmonic approximation to $k_{\mathrm{RPTST}}(\beta)$ can also be defined, which we name the h-RPTST rate. Here, we again choose to take the steepest-descent integral about the instanton geometry $\tilde{\mathbf{x}}$ with its unstable mode s_1 identified as the reaction coordinate $\sigma(\mathbf{x})$. By nature of the instanton geometry being a saddle point, it maximizes $U_N(\mathbf{x})$ in the direction of the reaction coordinate even when the other modes take their minimal values, as they must do in order to define the steepest-descent

*Note that, according to this definition, the usual centroid-based dividing surface is not normalized.

integral. This approximately minimizes the RPTST rate, which, as explained above, gives the result closest to that of RPMD. Using Eq. 4.7, transforming to the instanton's normal-mode coordinates $\{\mathbf{s}_k\}$, with the origin at $\tilde{\mathbf{x}}$ and applying the steepest-descent approximation gives

$$\begin{aligned} k_{\text{h-RPTST}}(\beta)Q_{\text{r}}(\beta) &= \sqrt{\frac{1}{2\pi m\beta_N}}\left(\frac{m}{2\pi\beta_N\hbar^2}\right)^{N/2} \mathrm{e}^{-\beta_N U_N(\tilde{\mathbf{x}})} \\ &\quad \times \int_{-\infty}^{\infty} \mathrm{d}s_1\, \delta[s_1] N\sqrt{B_N} \prod_{k=3}^{N} \int_{-\infty}^{\infty} \mathrm{d}s_k\, \mathrm{e}^{-\beta_N m\eta_k^2 s_k^2/2} \\ &= N\sqrt{\frac{B_N}{2\pi m\beta_N}}\left(\frac{m}{2\pi\beta_N\hbar^2}\right)^{N/2} \prod_{k=3}^{N} \sqrt{\frac{2\pi}{m\beta_N\eta_k^2}}\, \mathrm{e}^{-\beta_N U_N(\tilde{\mathbf{x}})} \\ &= \frac{N}{2\pi\beta_N\hbar}\sqrt{\frac{mB_N}{2\pi\beta_N\hbar^2}} \prod_{k=3}^{N} \frac{1}{\beta_N\hbar\eta_k}\, \mathrm{e}^{-\beta_N U_N(\tilde{\mathbf{x}})}, \end{aligned} \tag{4.8}$$

where the factor $N\sqrt{B_N}$ comes from the integral over s_2 (cf. §3.1.1).

Comparison with the $\operatorname{Im} F$ instanton rate (Eq. 3.25) shows that

$$k_{\text{inst}}(\beta) = \alpha_{\text{h}}(\beta) k_{\text{h-RPTST}}(\beta), \tag{4.9}$$

where

$$\alpha_{\text{h}}(\beta) = \frac{2\pi}{\beta\hbar|\eta_1|}, \tag{4.10}$$

and that the only disparity between the two methods is in the treatment of the imaginary mode.

At the cross-over temperature, where the instanton is collapsed, $\eta_1 = \omega_{\text{b}}$ and $\alpha_{\text{h}}(\beta_c) = 1$. Therefore, the harmonic RPTST rate will be a good approximation to the instanton rate just below the cross-over temperature, but will degrade in quality as the temperature decreases further.

4.4 Connection between RPTST and Im F theory

To find the relationship between RPTST and $\operatorname{Im} F$ theory without making the harmonic approximation of Chapter 3, we evaluate $\operatorname{Im} Q(\beta)$ by steepest descent along just the reaction coordinate $\sigma(\mathbf{x})$ but exactly in the other degrees of freedom (Mills et al., 1997). It is still necessary to evaluate the integral by the method of steepest descent in this direction because the analytic continuation is not defined otherwise.

First, we rewrite Eq. 2.14 as

$$Q(\beta) = \int_{-\infty}^{\infty} \mathrm{d}u \, \mathrm{e}^{-\beta_N F(u)}, \tag{4.11}$$

where the free energy is given by

$$F(u) = -\frac{1}{\beta_N} \ln Q_{\sigma=u} \tag{4.12}$$

and the constrained partition function by

$$Q_{\sigma=u} = A \int \mathrm{d}\mathbf{x} \, \mathrm{e}^{-\beta_N U_N(\mathbf{x})} \delta[\sigma(\mathbf{x}) - u], \tag{4.13}$$

where we have introduced a shorthand for the prefactor

$$A = \left(\frac{m}{2\pi\beta_N \hbar^2} \right)^{N/2}. \tag{4.14}$$

As we intend to evaluate the analytic continuation of Eq. 4.11 by steepest descent about $u = 0$, the reaction coordinate $\sigma(\mathbf{x})$ should be chosen to maximize the free energy at this point $F(0)$. This is equivalent to requiring that $\sigma(\mathbf{x}) = 0$ is the optimal dividing surface in the RPTST calculation, which can also be written in terms of $F(0)$.

Expanding $F(u)$ as a Taylor series about its maximum $F(0)$ and truncating to second order gives

$$Q(\beta) \approx \int_{-\infty}^{\infty} \mathrm{d}u \, \mathrm{e}^{-\beta_N \left[F(0) + \frac{1}{2} F''(0) u^2 \right]}, \tag{4.15}$$

where the primes on $F''(0)$ indicate differentiation with respect to u. This expression for $Q(\beta)$ is obviously extremely divergent, but we are able to obtain an expression for its imaginary part by following the same procedure used for $k_{\mathrm{inst}}(\beta)$ in §3.1.2 to analytically continue the integral over the reaction coordinate, i.e. by multiplying $u > 0$ by i. This yields

$$\mathrm{Im}\, Q(\beta) \approx \frac{1}{2} \sqrt{\frac{2\pi}{\beta_N |F''(0)|}} \, \mathrm{e}^{-\beta_N F(0)} \tag{4.16}$$

$$= \sqrt{\frac{\pi}{2\beta_N |F''(0)|}} \left(\frac{m}{2\pi\beta_N \hbar^2} \right)^{N/2} \int \mathrm{d}\mathbf{x} \, \mathrm{e}^{-\beta_N U_N(\mathbf{x})} \delta[\sigma(\mathbf{x})]. \tag{4.17}$$

Substitution of this expression into Eq. 3.9 yields the free-energy instanton rate

$$k_{\sigma\text{-inst}}(\beta)Q_{\mathrm{r}}(\beta) = \frac{1}{\beta\hbar}\sqrt{\frac{2\pi}{\beta_N|F''(0)|}}\left(\frac{m}{2\pi\beta_N\hbar^2}\right)^{N/2}\int \mathrm{d}\mathbf{x}\,\mathrm{e}^{-\beta_N U_N(\mathbf{x})}\delta[\sigma(\mathbf{x})], \tag{4.18}$$

and therefore, by comparison with Eq. 4.7 and assuming that $\sigma(\mathbf{x})$ is normalized to give unit Jacobian,

$$\alpha(\beta) = \frac{k_{\sigma\text{-inst}}(\beta)}{k_{\mathrm{RPTST}}(\beta)} = \frac{2\pi}{\beta\hbar}\sqrt{\frac{m}{|F''(0)|}}. \tag{4.19}$$

This is the relationship that we have been seeking, and it shows that in the deep-tunnelling regime and with the optimal dividing surface, RPTST is an approximation to the free-energy instanton rate $k_{\sigma\text{-inst}}(\beta)$ obtained by assuming $\alpha(\beta) \approx 1$. As discussed in §4.3, $\alpha_{\mathrm{h}}(\beta)$ tends to unity just below T_{c}, and because it is the steepest-descent approximation to $\alpha(\beta)$ and therefore quite similar, we expect that roughly the same properties hold for $\alpha(\beta)$. Therefore, RPTST will be a good approximation to $k_{\sigma\text{-inst}}(\beta)$ just below cross-over but will degrade in quality at lower temperatures. Of course, above the cross-over temperature, this relationship does not hold; $\mathrm{Im}\,F$ has a completely different form (see Appendix A), which is chosen such that it is equivalent to RPTST. It is therefore very good at describing shallow tunnelling through the parabolic top of the barrier and correctly tends to the classical TST rate at high temperatures.

4.5 Connection between RPMD and Im F theory

The results derived above allow us to define the sought-after connection between RPMD and the $\mathrm{Im}\,F$ rate theories in the deep-tunnelling regime,

$$k_{\mathrm{RPMD}}(\beta) = \frac{\kappa_{\mathrm{trans}}(\beta)}{\alpha(\beta)}k_{\sigma\text{-inst}}(\beta), \tag{4.20}$$

where $\kappa_{\mathrm{trans}}(\beta)$ is the transmission coefficient calculated through the optimal dividing surface and is therefore close to unity. This expression explains why RPMD rate theory has been found to perform so unexpectedly well below T_{c}—because, in this regime, the RPMD rate is a good approximation

to $k_{\sigma\text{-inst}}(\beta)$. However, because for complex systems the optimal dividing surface can be difficult to calculate, it may still be preferable to compute $k_{\text{RPMD}}(\beta)$ as this is dividing-surface independent.

Although at high temperatures, RPMD is likely to give the best approximation to the exact rate because it correctly describes classical or parabolic-tunnelling recrossing dynamics, below the cross-over temperature, $k_{\text{RPMD}}(\beta)$ has the more rigorous derivation and, as shown below, gives more accurate results. However, if the system involves too much recrossing, neither $\text{Im}\, F$ nor RPMD will be a good approximation to the exact rate as the former ignores the long-time effects and the latter employs artificial dynamics.

4.6 Numerical implementations of RPMD, RPTST and free-energy instanton rate theories

Numerical tests were carried out on one-dimensional systems in order to investigate the properties of $\kappa_{\text{trans}}(\beta)$ and $\alpha(\beta)$ and their effects on the RPMD rate. We also investigated methods for locating the optimal dividing surface needed to compute the RPTST and the free-energy instanton rates. In this section we present the results and conclusions of these applications.

Two model systems were placed under study: one with a symmetric barrier given in §3.2, and the other described by the same expression (Eq. 3.29) but with the following parameters in reduced units ($\hbar = m = 1$): $A = -18/\pi$, $B = 13.5/\pi$ and $a = 8/\sqrt{3\pi}$ (Craig and Manolopoulos, 2005*b*). The transition state is at $x^\ddagger = -(a/2)\ln 2$ where the frequency is $\mathrm{i}\omega_b = \mathrm{i}$, and therefore the cross-over temperature is at $\beta_\text{c} = 2\pi$. The exothermic reaction was studied, i.e. the reactants are defined to be at $x < x^\ddagger$.

4.6.1 Locating the optimal dividing surface

In order to calculate the RPTST rate, we need to locate the optimal dividing surface $\sigma(\mathbf{x}) = 0$ on which the free energy is a maximum. It will be an almost impossible task to search through a large ring-polymer space to find such a free-energy maximum, especially since the optimal dividing surface may be curved, but there is a standard procedure for achieving a good approximation to $\sigma(\mathbf{x})$ in variational transition-state theory (VTST) (Truhlar and Garrett, 1984), whereby the reaction is assumed to travel approximately along the

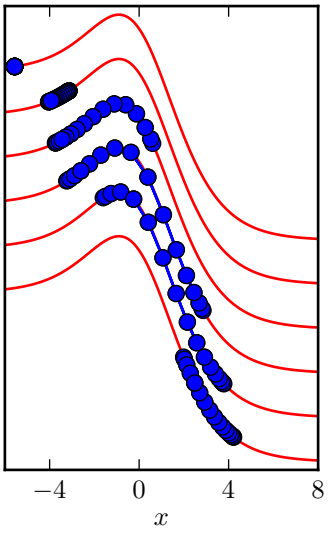

Figure 4.1 – Six snapshots of the minimum-energy pathway for a ring polymer traversing an asymmetric barrier below the cross-over temperature. The instanton geometry is represented in the third schema from the top.

minimum-energy pathway between reactants and products. The unstable mode of the transition state is chosen as the reaction coordinate, the dividing surface as the plane orthogonal to this, and the free energy is maximized in this direction only.

The minimum-energy reaction pathway for a ring polymer with potential $U_N(\mathbf{x})$ was computed by following the direction of steepest-descent down from the transition state in both directions. Above the cross-over temperature, the beads are collapsed all the way along this path such that there are no significant deviations from a classical calculation and the reaction coordinate is described by the centroid mode q_0 alone. However, below T_c, the ring polymer stretches as is shown by the example pathway in Figure 4.1 and the higher modes are also excited. The transition state (and maximum of $U_N(\mathbf{x})$ along the pathway) is of course the instanton geometry $\tilde{\mathbf{x}}$ and the unstable mode is s_1.

As explained in §3.1.1, between the temperatures T_c and $T_c/2$, a collapsed ring polymer at the top of the barrier $x_i = x^\ddagger$ has three unstable modes, q_0 and $q_{\pm 1}$. We therefore expect that in this regime, the geometry of a ring polymer in the vicinity of the barrier will be dominated by only these three

normal modes, and that only they will significantly contribute to s_1.

We shall attempt to construct a good approximation to the optimal dividing surface, using only these modes, but because of the degeneracy of the $q_{\pm 1}$ modes, it is expedient to convert to a cylindrical coordinate system by defining a "stretching" mode

$$r = \sqrt{q_1^2 + q_{-1}^2}, \tag{4.21}$$

which is orthogonal to the centroid mode q_0 and independent of cyclic permutation of the beads, which is instead described by the angle θ such that

$$q_1 = r\cos\theta, \qquad\qquad q_{-1} = r\sin\theta. \tag{4.22}$$

In the $N \to \infty$ limit, the ring-polymer potential $U_N(\mathbf{x})$, and hence the free energy, are independent of θ.

In this coordinate system, we have explained that the optimal dividing surface will approximately be a function of only q_0 and r. As an illustration to the problem, we can define a free-energy surface as

$$F(q^*, r^*) = -\frac{1}{\beta_N} \ln Q(q^*, r^*), \tag{4.23}$$

where

$$Q(q^*, r^*) = \left(\frac{m}{2\pi\beta_N\hbar^2}\right)^{N/2} \int\cdots\int \mathrm{e}^{-\beta_N U_N(\mathbf{x})} \times \delta[q_0 - q^*]\,\delta[r - r^*]\,\mathrm{d}q_0\, r\mathrm{d}r\,\mathrm{d}\theta\,\mathrm{d}q_2\,\mathrm{d}q_{-2}\ldots\mathrm{d}q_{N/2}. \tag{4.24}$$

This is computed by Monte Carlo importance sampling (see below) in the cylindrical normal-mode coordinates with q_0 and r fixed, whereas θ is selected from a uniform distribution between 0 and 2π. The surfaces are plotted at two different temperatures for both the symmetric and asymmetric barriers (see Figures 4.2 and 4.3). For both systems, the saddle point moves away from a collapsed $r = 0$ geometry to a stretched instanton when the temperature drops below cross-over, as a consequence of $\omega_{\pm 1}$ becoming imaginary. The optimal dividing surface for the symmetric barrier is not affected by this change, because of the symmetry in the free-energy surface. However, for

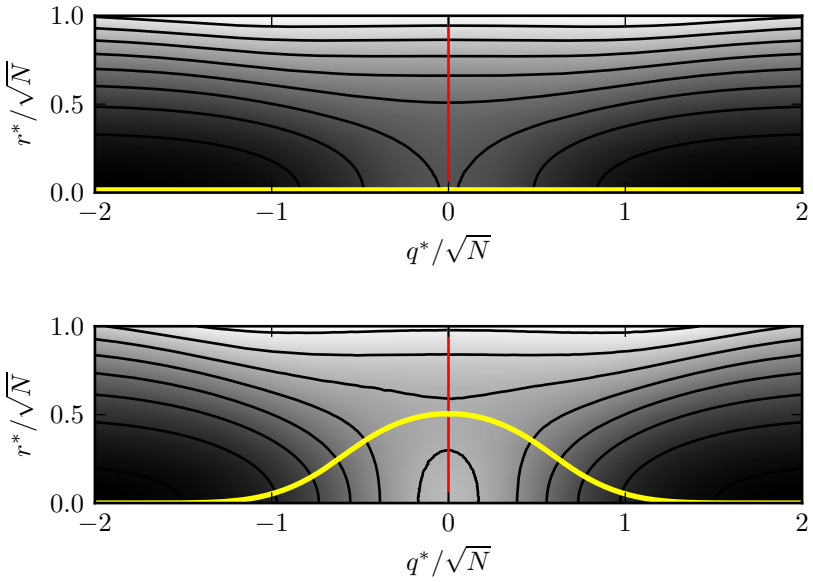

Figure 4.2 – The free-energy surface for the symmetric Eckart barrier above and below cross-over at $\beta = 6$ (upper) and $\beta = 10$ (lower). The steepest-descent paths from the instanton geometry are depicted in yellow and the dividing surfaces perpendicular to this in red.

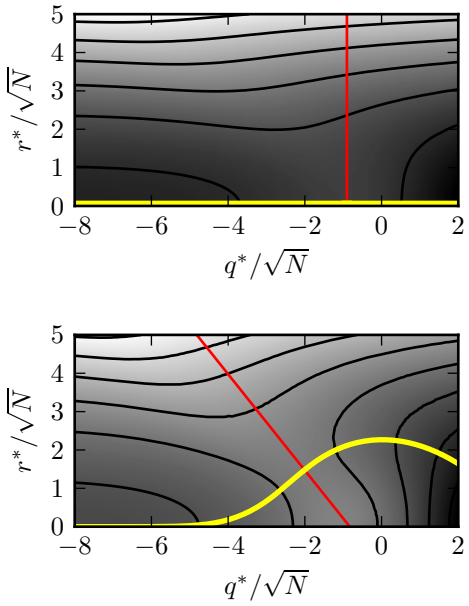

Figure 4.3 – As Figure 4.2 for the asymmetric Eckart barrier.

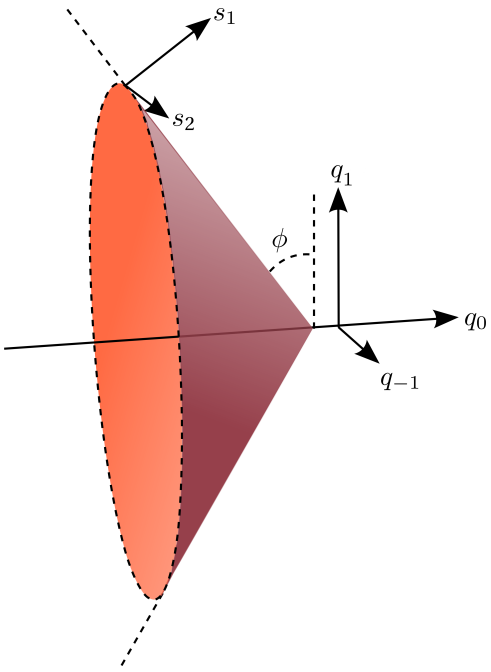

Figure 4.4 – Approximate form of the optimal free-energy dividing surface $\sigma(\mathbf{x})$ for an asymmetric barrier. The conical surface is plotted in the space of the modes q_0 and $q_{\pm1}$ and has circular symmetry in the plane of (q_1, q_{-1}). Also shown are the directions of the normal modes s_1 and s_2 at one particular instanton geometry.

the asymmetric barrier below T_c, $\sigma(\mathbf{x})$ must take on a strong dependence on r in order to follow the free-energy ridge. In all cases, the optimal dividing surface is approximately perpendicular to the minimum-energy path and therefore the unstable mode of the saddle point.

Because the free energy is independent of θ, the dividing surface for the low-temperature asymmetric case is not planar but conical in the space of the ring-polymer normal modes, as shown in Figure 4.4. The set of equivalent instanton geometries related by cyclic permutation lie on the circle which is the intersection between the cone and a plane perpendicular to q_0. Picking an arbitrary point on this circle and calculating its normal modes yields s_1 and s_2 which are depicted on the figure. The normal mode s_1 is perpendicular to the surface of the cone and s_2 points tangentially around the circle.

4.6.2 Approximate dividing surfaces

The simplest form of ring-polymer dividing surface is based only on the centroid mode,

$$\sigma(\mathbf{x}) = q_0 - \sigma_0 = 0, \tag{4.25}$$

where σ_0 is chosen to maximize the free energy. This form has been frequently used in previous path-integral calculations and with this definition, RPTST reduces to VCM, and $k_{\sigma\text{-inst}}(\beta)$ to the rate derived by Gillan (1987) as shown by Makarov and Topaler (1995).

As we have explained, above the cross-over temperature, the unstable mode of the collapsed saddle point $x_i = x^\ddagger$ is dominated by q_0, and so we expect the centroid surface to lead to an accurate rate. However, unless the system is symmetric, the modes $q_{\pm 1}$ will also contribute at low temperatures. Between β_c and $2\beta_c$ these are the only modes which are expected to be important, and so a good approximation to the optimal dividing surface can be written as a linear combination of these contributing modes,

$$\sigma(\mathbf{x}) = q_0 \cos\phi + r \sin\phi - \sigma_0 = 0, \tag{4.26}$$

where r is defined in Eq. 4.21 and ϕ is a parameter which should be chosen variationally to make Eq. 4.26 resemble as closely as possible the optimal dividing surface. This dividing surface and all proceeding formulae reduce to the centroid-based case (Eq. 4.25) if $\phi = 0$.

In order to compute the rate with these dividing surfaces the constrained partition function $Q_{\sigma=0}$ from Eq. 4.13 was calculated by integrating over all but one of the free-ring-polymer normal modes $q_{k\neq 0}$ using importance sampling.* The centroid mode q_0, however, was chosen so as to make the

*Monte Carlo importance sampling (Frenkel and Smit, 1996, §3.1.1) computes integrals using the relation

$$\frac{\int \mathrm{d}x\, f(x)w(x)}{\int \mathrm{d}x\, w(x)} = \langle f(x)\rangle^w = \frac{1}{L}\sum_{l=1}^{L} f(x^l), \tag{4.27}$$

where the values of x^l are chosen randomly with a probability $w(x^l)$ and where L is the sample size. The standard error in the result is computed as

$$\sqrt{\frac{\langle f(x)^2\rangle^w - \left(\langle f(x)\rangle^w\right)^2}{L-1}}. \tag{4.28}$$

delta function non-zero.

$$\begin{aligned} Q_{\sigma=0} &= A \int \mathrm{d}\mathbf{x}\, \mathrm{e}^{-\beta_N U_N(\mathbf{x})} \delta[q_0 \cos\phi + r \sin\phi - \sigma_0] \\ &= \frac{A}{\cos\phi} \int \mathrm{d}\mathbf{q}\, \mathrm{e}^{-\beta_N \sum_{i=1}^{N} V(x_i)} \mathrm{e}^{-\beta_N \sum_k m\omega_k^2 q_k^2/2} \delta\left[q_0 - \frac{\sigma_0 - r\sin\phi}{\cos\phi}\right] \\ &= \sqrt{\frac{m}{2\pi\beta_N\hbar^2}} \frac{1}{\cos\phi} \prod_{k\neq 0} \frac{1}{\beta_N \hbar\omega_k} \left\langle \mathrm{e}^{-\beta_N \sum_{i=1}^{N} V(x_i)} \right\rangle_{\sigma=0}^{\text{free}} \\ &= \sqrt{\frac{m}{2\pi\beta_N\hbar^2}} \frac{1}{N\cos\phi} \left\langle \mathrm{e}^{-\beta_N \sum_{i=1}^{N} V(x_i)} \right\rangle_{\sigma=0}^{\text{free}}, \end{aligned} \tag{4.29}$$

where the angular brackets $\langle \cdots \rangle_{\sigma=0}^{\text{free}}$ describe a Monte Carlo average computed over the modes $q_{k\neq 0}$ randomly selected from a normal distribution with mean 0 and variance $1/\beta_N m\omega_k^2$ but with a constraint on the centroid mode. The frequencies ω_k are those of a ring polymer in free space, i.e. Eq. 2.23 with $\omega_\mathrm{s} = 0$. In practical terms, we compute

$$Q_{\sigma=0} = \sqrt{\frac{m}{2\pi\beta_N\hbar^2}} \frac{1}{LN\cos\phi} \sum_{l=1}^{L} \mathrm{e}^{-\beta_N \sum_{i=1}^{N} V(x_i^l)},$$

where $\mathbf{x}^l$ is computed from $\mathbf{q}^l$ by the inverse normal-mode transformation and $q_k^l \sim \mathcal{N}(0, 1/\beta_N m\omega_k^2)$ for all k except $k = 0$ for which

$$q_0^l = \frac{\sigma_0 - \sqrt{\left(q_1^l\right)^2 + \left(q_{-1}^l\right)^2} \sin\phi}{\cos\phi}.$$

The rate is found by substituting this constrained partition function into Eq. 4.7 or Eq. 4.18 as appropriate.

In previous implementations $k_{\mathrm{RPTST}}(\beta)$ has been computed using thermodynamic integration with a constraint on the centroid or umbrella integration (Kästner and Thiel, 2005) with biased molecular dynamics. However, for these one-dimensional test systems, it was even simpler to use the importance sampling method described here. This situation will be reversed for larger and more complex systems.

We consider first the centroid dividing surface Eq. 4.25 which has only one parameter to be chosen. The value of σ_0 is obviously equal to 0 for the symmetric Eckart barrier because of the symmetry of the free-energy surface. For the asymmetric case, however, it is not obvious in general where to place

the dividing surface, and σ_0 should be chosen so as to maximize the free energy $F(0)$. In the classical limit, the optimal location is at the barrier top $x^\ddagger$, but it moves towards the reactants (defined such that the reaction is exothermic) as the temperature is lowered. This is because the ring-polymer beads spread out more at lower temperatures and would start to sample the lower-energy product side if the dividing surface were not moved away.

With the improved form of the dividing surface given in Eq. 4.26, a method already in common use for variational TST (Truhlar and Garrett, 1984) was employed, in which a plane orthogonal to the unstable mode of the saddle point is moved along the unstable mode to maximize the free energy on the plane. A similar method can be applied to the ring-polymer potential surface $U_N(\mathbf{x})$ although in this case there exists a ring of identical saddle points—the instanton geometries. The following method was used: one particular permutation of the instanton saddle point was located on the surface using the stream-bed walk algorithm (Nichols et al., 1990). The resulting geometry $\tilde{\mathbf{x}}$ was transformed to normal-mode coordinates $\tilde{\mathbf{q}}$ as defined by Eq. 2.22. The eigenvector corresponding to the negative eigenvalue was taken to be the local direction of the reaction coordinate, and the dividing surface cone defined such that it was orthogonal to this direction at $\tilde{\mathbf{x}}$. The angle ϕ is the pitch of the conical dividing surface and can be computed using

$$\phi = -\tan^{-1} \frac{\sqrt{\tilde{q}_1^2 + \tilde{q}_{-1}^2}}{\tilde{q}_0}. \tag{4.30}$$

This definition accounts for the degeneracy of $q_{\pm 1}$, which results in the zero-frequency mode at the instanton geometry, and the conical shape describes the optimal dividing surface well because this preserves the circular degree of freedom linking all the cyclic permutations and therefore maximizes the free energy. The free energy calculation will include ring polymers which either lie collapsed near to the barrier or are stretched out but shifted towards the reactants. On the other hand, a flat plane does not give a good approximation to the optimal dividing surface and samples ring polymers which lie deep into the low-energy product side leading to an unphysically low value of the free energy.

To obtain the optimal value of σ_0 which maximizes the free energy for a given ϕ , we shall need to be able to compute the derivative with respect to the reaction coordinate, for which a small mathematical aside is required.

The chain rule gives

$$\frac{\partial}{\partial\sigma} = \frac{\partial q_0}{\partial\sigma}\frac{\partial}{\partial q_0} + \frac{\partial r}{\partial\sigma}\frac{\partial}{\partial r} + \frac{\partial\theta}{\partial\sigma}\frac{\partial}{\partial\theta}. \tag{4.31}$$

The space spanned by (q_0, r, θ) is also spanned by (σ, ρ, θ) where ρ is defined to be orthogonal to the reaction coordinate,

$$\sigma = q_0\cos\phi + r\sin\phi - \sigma_0, \tag{4.32}$$

$$\rho = -q_0\sin\phi + r\cos\phi - \rho_0. \tag{4.33}$$

These simultaneous equations are solved for q_0 and r to give

$$\frac{\partial q_0}{\partial\sigma} = \cos\phi, \qquad \frac{\partial r}{\partial\sigma} = \sin\phi, \qquad \frac{\partial\theta}{\partial\sigma} = 0. \tag{4.34}$$

Using Eq. 4.22, we also find

$$\frac{\partial}{\partial r} = \frac{\partial q_1}{\partial r}\frac{\partial}{\partial q_1} + \frac{\partial q_{-1}}{\partial r}\frac{\partial}{\partial q_{-1}} = \cos\theta\frac{\partial}{\partial q_1} + \sin\theta\frac{\partial}{\partial q_{-1}}, \tag{4.35}$$

where $\theta = \tan^{-1}(q_{-1}/q_1)$ and therefore

$$\frac{\partial}{\partial\sigma} = \cos\phi\frac{\partial}{\partial q_0} + \sin\phi\cos\theta\frac{\partial}{\partial q_1} + \sin\phi\sin\theta\frac{\partial}{\partial q_{-1}}. \tag{4.36}$$

Finding the optimal value of σ_0 is equivalent to locating the maximum of $F(u)$ defined with the more general form of the dividing surface (Eq. 4.26). We therefore computed the mean force

$$-F'(u) = -\frac{\partial F(u)}{\partial u} = \frac{1}{\beta_N}\frac{1}{Q_{\sigma=0}}\frac{\partial Q_{\sigma=u}}{\partial u}. \tag{4.37}$$

Following Frenkel and Smit (1996, 16.2.1),

$$\frac{\partial Q_{\sigma=u}}{\partial u} = A\int \mathrm{e}^{-\beta_N U_N(\mathbf{q})}\,\frac{\partial\delta[\sigma-u]}{\partial u}\,\mathrm{d}\mathbf{q} \tag{4.38a}$$

$$= -A\int \mathrm{e}^{-\beta_N U_N(\mathbf{q})}\,\frac{\partial\delta[\sigma-u]}{\partial\sigma}\,\mathrm{d}\mathbf{q} \tag{4.38b}$$

$$= -A\int\cdots\int \mathrm{e}^{-\beta_N U_N(\mathbf{q})}\,\frac{\partial\delta[\sigma-u]}{\partial\sigma}\,r\,\mathrm{d}\sigma\,\mathrm{d}\rho\,\mathrm{d}\theta\,\mathrm{d}q^{N-3}, \tag{4.38c}$$

where $\mathrm{d}q^{N-3}$ is a shorthand for $\mathrm{d}q_{1-N/2}\ldots\mathrm{d}q_{-2}\,\mathrm{d}q_2\ldots\mathrm{d}q_{N/2}$, and we have

used the result that the Jacobian for the transformation from $\mathbf{q}$ to a set of coordinates including the reaction coordinate σ is $|J| = r$. Integrating along σ by parts gives

$$\frac{\partial Q_{\sigma=u}}{\partial u} = A \int \cdots \int \frac{\partial}{\partial \sigma} \left(r \mathrm{e}^{-\beta_N U_N(\mathbf{q})} \right) \delta[\sigma - u] \, \mathrm{d}\sigma \, \mathrm{d}\rho \, \mathrm{d}\theta \, \mathrm{d}q^{N-3} \tag{4.39a}$$

$$= A \int \left(\frac{\partial r}{\partial \sigma} - r\beta_N \frac{\partial U_N}{\partial \sigma} \right) \mathrm{e}^{-\beta_N U_N(\mathbf{q})} \, \frac{\delta[\sigma - u]}{r} \, \mathrm{d}\mathbf{q} \tag{4.39b}$$

$$= A \int \left(\frac{\sin\phi}{r} - \beta_N \frac{\partial U_N}{\partial \sigma} \right) \mathrm{e}^{-\beta_N U_N(\mathbf{q})} \, \delta[\sigma - u] \, \mathrm{d}\mathbf{q}. \tag{4.39c}$$

There are (at least) two ways for computing integral in Eq. 4.39c. We could use importance sampling as used on the constrained partition function above, in which case

$$\frac{\partial Q_{\sigma=u}}{\partial u} = \sqrt{\frac{m}{2\pi\beta_N\hbar^2}} \frac{1}{N\cos\phi} \left\langle \left(\frac{\sin\phi}{r} - \beta_N \frac{\partial U_N}{\partial \sigma} \right) \mathrm{e}^{-\beta_N \sum_{i=1}^{N} V(x_i)} \right\rangle_{\sigma=u}^{\text{free}}, \tag{4.40}$$

where the derivative of the ring-polymer potential is defined by Eq. 4.36. However one can use a more efficient sampling procedure to obtain $F'(u)$ directly,

$$-F'(u) = \frac{1}{\beta_N} \left\langle \frac{\sin\phi}{r} - \beta_N \frac{\partial U_N}{\partial \sigma} \right\rangle_{\sigma=u}, \tag{4.41}$$

where the angular brackets $\langle \cdots \rangle_{\sigma=0}$ denote a canonical average at reciprocal temperature β_N subject to the classical Hamiltonian in Eq. 2.16 with the constraint $\sigma = u$. The ensemble average is taken over points selected from a constant-temperature constrained molecular-dynamics simulation.* To enforce the constraints, the RATTLE algorithm (Andersen, 1983) was found to be simple to apply, especially as in this case iterative steps are not required, whereas the energy was allowed to fluctuate according to the temperature using the Andersen thermostat (Andersen, 1980), as described in Appendix D.

The root of $F'(u)$, and therefore the maximum of $F(u)$ and minimum of $Q_{\sigma=u}$, was found using an algorithm based on Brent's method (Press et al., 1992, §9.3). In this way we obtain the value of σ_0 which will give the optimal dividing surface $\sigma = 0$ within our approximation and therefore give the maximal value of $\kappa_{\text{trans}}(\beta)$ such that $k_{\text{RPTST}}(\beta)$ is the best estimate of

*As we are assuming a linear reaction coordinate σ, no correction to the sampling bias is required (Frenkel and Smit, 1996, §15.1.1).

the RPMD rate and $k_{\sigma\text{-inst}}(\beta)$ of the Im F rate.

4.6.3 Computing $\alpha(\beta)$

The factor $\alpha(\beta)$ defined in Eq. 4.19 converts the RPTST rate into $k_{\sigma\text{-inst}}(\beta)$. It will only be necessary to include this factor when the temperature is below cross-over because the RPTST rate is well defined above T_c and only needs correcting in the deep-tunnelling regime.

The only non-trivial term in the definition is the second derivative of the free energy which can be written as

$$F''(0) = \left.\frac{\partial^2 F(u)}{\partial u^2}\right|_{u=0} = -\frac{1}{\beta_N}\left[\frac{Q''_{\sigma=0}}{Q_{\sigma=0}} - \left(\frac{Q'_{\sigma=0}}{Q_{\sigma=0}}\right)^2\right] = -\frac{1}{\beta_N}\frac{Q''_{\sigma=0}}{Q_{\sigma=0}}, \quad (4.42)$$

since $F'(0) = 0$ for the optimal choice of σ. Taking the approximate conical dividing surface in Eq. 4.26,

$$\begin{aligned}
Q''_{\sigma=u} &= A\int\left(\frac{\sin\phi}{r} - \beta_N\frac{\partial U_N}{\partial\sigma}\right)\mathrm{e}^{-\beta_N U_N(\mathbf{q})}\,\frac{\partial\delta[\sigma-u]}{\partial u}\,\mathrm{d}\mathbf{q} \\
&= -A\int\left(\frac{\sin\phi}{r} - \beta_N\frac{\partial U_N}{\partial\sigma}\right)\mathrm{e}^{-\beta_N U_N(\mathbf{q})}\,\frac{\partial\delta[\sigma-u]}{\partial\sigma}\,r\,\mathrm{d}\sigma\,\mathrm{d}\rho\,\mathrm{d}\theta\,\mathrm{d}q^{N-3} \\
&= A\int\frac{\partial}{\partial\sigma}\left[\left(\sin\phi - r\beta_N\frac{\partial U_N}{\partial\sigma}\right)\mathrm{e}^{-\beta_N U_N(\mathbf{q})}\right]\delta[\sigma-u]\,\mathrm{d}\sigma\,\mathrm{d}\rho\,\mathrm{d}\theta\,\mathrm{d}q^{N-3} \\
&= A\int\left[-r\beta_N\frac{\partial^2 U_N}{\partial\sigma^2} - 2\sin\phi\beta_N\frac{\partial U_N}{\partial\sigma} + r\left(\beta_N\frac{\partial U_N}{\partial\sigma}\right)^2\right] \\
&\qquad\times\mathrm{e}^{-\beta_N U_N(\mathbf{q})}\,\frac{\delta[\sigma-u]}{r}\,\mathrm{d}\mathbf{q},
\end{aligned} \quad (4.43)$$

such that

$$Q''_{\sigma=0} = A\int\left[-\beta_N\frac{\partial^2 U_N}{\partial\sigma^2} - 2\frac{\sin\phi}{r}\beta_N\frac{\partial U_N}{\partial\sigma} + \left(\beta_N\frac{\partial U_N}{\partial\sigma}\right)^2\right]\mathrm{e}^{-\beta_N U_N(\mathbf{q})}\delta[\sigma]\,\mathrm{d}\mathbf{q}. \quad (4.44)$$

The result is computed using either Monte Carlo importance sampling from

$$Q''_{\sigma=0} = \sqrt{\frac{m}{2\pi\beta_N\hbar^2}}\frac{1}{N\cos\phi} \times \left\langle \left[-\beta_N \frac{\partial^2 U_N}{\partial\sigma^2} - 2\beta_N \frac{\partial U_N}{\partial\sigma}\frac{\sin\phi}{r} + \left(\beta_N \frac{\partial U_N}{\partial\sigma}\right)^2 \right] \mathrm{e}^{-\beta_N \sum_i V(x_i)} \right\rangle^{\mathrm{free}}_{\sigma=0}, \tag{4.45}$$

or directly from a canonical average,

$$F''(0) = \left\langle \frac{\partial^2 U_N}{\partial\sigma^2} + 2\frac{\sin\phi}{r}\frac{\partial U_N}{\partial\sigma} - \beta_N \left(\frac{\partial U_N}{\partial\sigma}\right)^2 \right\rangle_{\sigma=0}. \tag{4.46}$$

In either case, the second derivative of U_N is computed by finite differences of the first derivative.

4.6.4 RPMD transmission coefficient

The final step in the calculation of the RPMD rate is the transmission coefficient

$$\kappa_{\mathrm{trans}}(\beta) = \frac{\lim_{t\to\infty} c_{\mathrm{fs}}(t)}{\lim_{t\to 0^+} c_{\mathrm{fs}}(t)}, \tag{4.47}$$

where the ring-polymer flux-side correlation function is

$$c_{\mathrm{fs}}(t) = \langle v_\sigma(\mathbf{w}_0, \mathbf{q}_0)\, h[\sigma(\mathbf{q}_t)]\rangle_{\sigma(\mathbf{q}_0)=0}\,. \tag{4.48}$$

The momenta and positions in normal-mode coordinates $\mathbf{q}_t$ and $\mathbf{w}_t$ are now treated explicitly as functions of real time t and the flux through the conical dividing surface is

$$v_\sigma(\mathbf{w}, \mathbf{q}) = \frac{1}{m}\left[w_0\cos\phi + \frac{q_1 w_1 + q_{-1}w_{-1}}{q_1^2 + q_{-1}^2}\sin\phi \right]. \tag{4.49}$$

Note that there are two types of ring-polymer trajectories involved in these expressions. The usual constant-temperature constrained molecular dynamics algorithm is used to sample the space (Appendix D) but every so often a real-time constant-energy unconstrained trajectory is computed from one of the sampled configurational points. The initial momentum $\mathbf{p}_0$ for this trajectory, however, is selected from the Maxwell-Boltzmann distribution

$\mathcal{N}(0, m/\beta_N)$. The trajectories are calculated using a combination of the velocity Verlet algorithm according to the Hamiltonian in Eq. 2.16 and an exact iterator for the harmonic parts of the potential as described by the procedure in Appendix C. The trajectories were propagated for long enough such that a plateau appeared in the function $c_{\mathrm{fs}}(t)$ and the ratio between the final and initial values was taken to be the transmission coefficient.

4.7 Results and comparisons of the methods

The results from the calculations, on the symmetric and asymmetric barriers, are presented in Tables 4.1 and 4.2 in the form of tunnelling-correction factors

$$c(\beta) = k(\beta)/k_{\mathrm{cl}}(\beta). \tag{4.50}$$

Table 4.3 gives the parameters used for defining the optimal dividing surfaces. As expected, $k_{\mathrm{RPMD}}(\beta)$ provides a lower bound to both the VCM and RPTST rates. However, RPTST is a significantly better estimate of the exact rate than VCM for the low-temperature asymmetric reaction when the conical dividing surface from Eq. 4.26 is used, and is almost equal to the RPMD rate, implying that the dividing surface chosen is very close to optimal. The h-RPTST calculations do a pretty good job of estimating the RPTST and RPMD rates for a fraction of the effort. The only major discrepancy in this harmonic approximation is just above the cross-over temperature when the ring-polymer surface becomes very flat. This occurs when the beads are collapsed, and the system is effectively treated as a parabolic barrier for which the exact rate diverges at T_{c}. The effect of the $\alpha(\beta)$ factor improves the results (relative to the exact rate) for both the harmonic instanton and free-energy instanton for both potentials at all relevant temperatures.

The factor $\alpha(\beta)$ is seen to increase the rates for the symmetric barrier but decrease the rates in the asymmetric case. To provide an explanation for this, we examine the trend of the harmonic approximation to $\alpha(\beta)$ as this is simpler but behaves in the same way. It is defined as, from Eq. 4.10,

$$\alpha_{\mathrm{h}}(\beta) = \frac{2\pi}{\beta\hbar|\eta_1(\beta)|}. \tag{4.51}$$

Figure 4.5 shows the variation of the parameter with decreasing temperature for both potentials.

Table 4.1 – Quantum correction factors $c(\beta)$ for the symmetric Eckart barrier. The cross-over temperature is given by $\beta_c\hbar\omega_b = 2\pi$, and the number of beads used in the calculations was $N = 60$. The exact quantum-mechanical rate constant (QM) was given by Eq. 3.28.

$\beta\hbar\omega_b$	RPMD	RPTST[a]	σ-inst	QM	Inst.	h-RPTST
2	1.17	1.17	...	1.22	...	1.19
4	1.87	1.87	...	2.07	...	2.20
6	4.35	4.36	...	5.20	...	21.4
8	16.2	16.4	21.2	21.8	22.0	17.5
10	104	107	142	162	137	90.2
12	1110	1160	1670	1970	1620	931

[a] Using the dividing surface Eq. 4.25 because, owing to symmetry, $\phi = 0$. This is equivalent to the method of Voth et al. (1989).

Table 4.2 – As Table 4.1 for the asymmetric Eckart barrier with $N = 256$.

$\beta\hbar\omega_b$	RPMD	VCM[a]	RPTST[b]	σ-inst	QM	Inst.	h-RPTST
2	1.18	1.18	1.18	...	1.20	...	1.19
4	1.96	1.98	1.98	...	2.01	...	2.20
6	5.28	5.61	5.61	...	5.32	...	21.3
8	28	36	30	28	26.1	28.1	33.1
10	320	540	330	260	251	232	321
12	5900	16000	6300	4200	4060	3690	5910

[a] Using the dividing surface Eq. 4.25. This is equivalent to the method of Voth et al. (1989).
[b] Using the dividing surface Eq. 4.26.

Table 4.3 – Parameters characterizing the optimal dividing surface for the asymmetric Eckart barrier with $q^\ddagger \approx -0.90$.

	VCM	RPTST	
β	σ_0	$\phi/^\circ$	σ_0
2	−0.97	0	−0.97
4	−1.06	0	−1.06
6	−1.24	0	−1.24
8	−1.58	32	−0.77
10	−2.03	39	−0.70
12	−2.47	43	−0.71

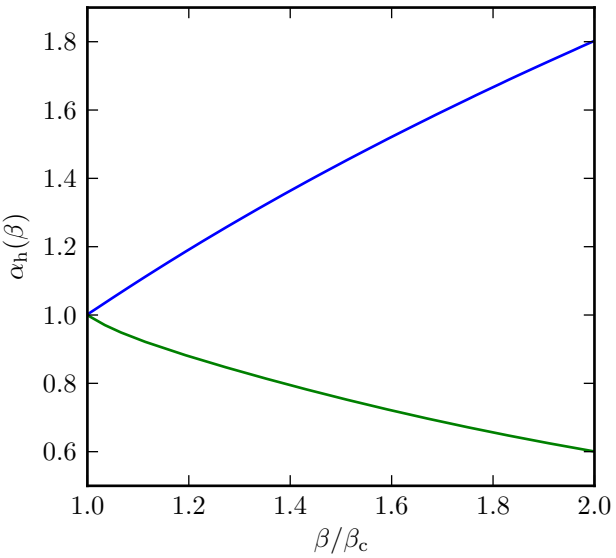

Figure 4.5 – Variation of $\alpha_{\mathrm{h}}(\beta)$ with temperature for the symmetric (blue line) and asymmetric (green line) Eckart barriers.

The reason why $\alpha(\beta)$ increases with β for symmetric but not for strongly asymmetric barriers can be examined by studying the variation of the eigenvalues and the centroid-only component of the Hessian, for which, see Figure 4.6. With respect to the centroid coordinate, the only effect on the Hessian is in the external potential V and so we write

$$\frac{\partial^2 U_N}{\partial q_0^2} = \frac{1}{N}\sum_{i=1}^{N}\frac{\partial^2 V}{\partial x_i^2}, \tag{4.52}$$

which is large and negative when the ring polymer is near the top of the barrier and decreases sharply in magnitude* as the temperature is lowered because the ring polymer spreads out into regions of positive curvature. Because cross-terms between the centroid and first normal mode,

$$\frac{\partial^2 U_N}{\partial q_0 \partial q_1} = \frac{\sqrt{2}}{N}\sum_{i=1}^{N}\frac{\partial^2 V}{\partial x_i^2}\sin\frac{2\pi i}{N}, \tag{4.53}$$

are forbidden by symmetry,† the centroid component of the Hessian dominates

*For this system, it appears to go like $1/\beta^4$. This relationship, however, was not found to hold for other symmetric systems.

†This is because beads i and $i + N/2$ contribute equally but with opposite signs.

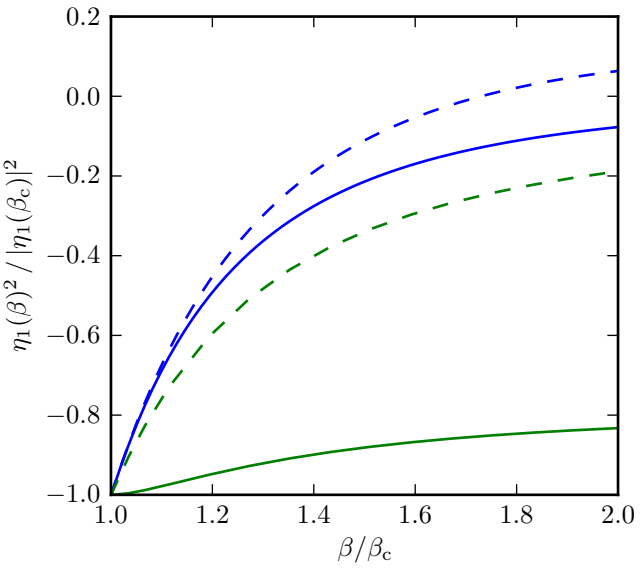

Figure 4.6 – Variation of the negative eigenvalue of the instanton with β for the symmetric (solid blue line) and asymmetric (solid green line) Eckart barriers. Also the variation of the second derivative of $U_N(\tilde{\mathbf{x}})$ with respect only to the centroid coordinate (Eq. 4.52) for both barriers is shown with dashed lines in the same colours.

for symmetric barriers and $\eta_1(\beta)^2$ follows this trend. The second derivative with respect to the centroid can become positive at low temperatures which can cause problems for some centroid-based TST methods (Cao and Voth, 1996). However, the generalized method presented here has no such difficulty since the higher (even-numbered) modes $q_{\pm k}$ come to the rescue and keep $\eta_1(\beta)^2$ negative.

In the case of the asymmetric barrier, the value of Eq. 4.52 also increases sharply (towards zero). The difference is, however, that now the cross-terms in Eq. 4.53 are allowed and mixing occurs with the first normal modes. Because the coupling term is large and real for a strongly asymmetric barrier, it dramatically reduces the eigenvalue $\eta_1(\beta)^2$, forcing it to change slowly with β such that $\alpha(\beta) \approx \beta_c/\beta$ as is seen in Figure 4.5.

This prediction that RPMD underestimates the rate for symmetric barriers and overestimates the rate for strongly asymmetric barriers is borne out by calculations on the symmetric reactions $H + H_2$ and $Cl + HCl$ and on the asymmetric reaction $F + H_2$ by Collepardo-Guevara et al. (2010) and Stecher (2010).

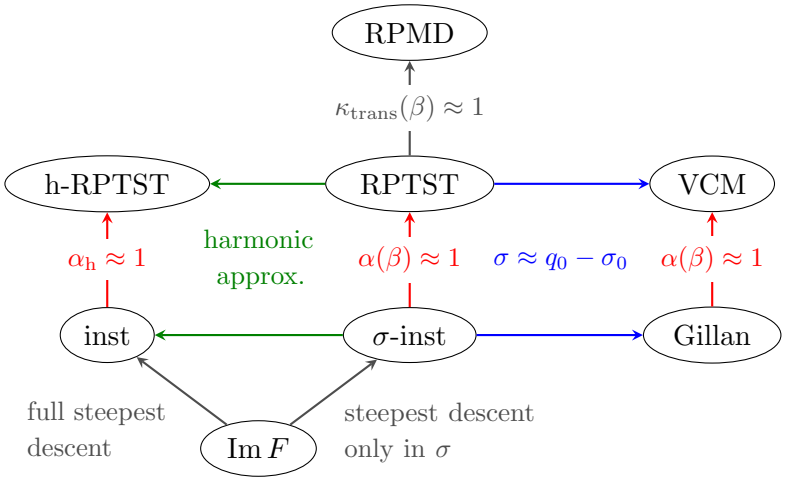

Figure 4.7 – A schematic showing the relationships between the different quantum rate theories mentioned in the text, where the arrows represent the approximations made. This applies only in the deep-tunnelling regime.

4.8 Summary

By taking the short-time limit of RPMD, we have obtained a new quantum transition-state theory named RPTST, equivalent to that of Voth et al. (1989) for symmetric barriers, but greatly improved in the case of asymmetric barriers in the deep-tunnelling regime. This was achieved by giving the first normal modes of the ring polymer equal importance to the centroid mode when the dividing surface was chosen. Using the improved dividing surface does not of course affect the RPMD rate but it does, however, improve the statistics necessary for convergence of the transmission coefficient $\kappa_{\mathrm{trans}}(\beta)$ enormously. For example, in order to accurately compute the second significant figure for the $\beta = 12$ entry in Table 4.2, only 10^4 trajectories were needed whereas full convergence was not quite reached even with 10^6 for the centroid dividing surface.

An important consequence of this work is a derivation of RPMD from Im F, explaining why RPMD performs so well in the deep-tunnelling regime. Above the cross-over temperature, where RPMD accurately includes parabolic tunnelling, RPTST is obviously an approximation to RPMD as it neglects the classical recrossing effects. However, below T_{c}, the fictitious ring-polymer dynamics cannot be expected to reproduce the quantum recrossing, and the transmission coefficient should be regarded not as a dynamical correction factor, but as a correction to the free energy owing to a poor choice of

dividing surface. For diffusive dynamical systems below cross-over, fictitious recrossing effects will also contribute to κ_{trans}. In these cases, it will be useful to compute the RPTST rate such that the two effects on the transmission coefficient can be more clearly discerned.

Assuming that we have chosen the optimal dividing surface (to which Eq. 4.26 seems very close), RPTST can be derived from the free-energy instanton rate $k_{\sigma\text{-inst}}(\beta)$ and hence from $\text{Im}\, F$ theory by taking the approximation that $\alpha(\beta) \approx 1$ which introduces only a small error if the trends in Figure 4.5 are held to be generally true. The concepts involved in this derivation are summarized in Figure 4.7 which also shows relations between RPMD, the centroid-based TST methods and the corresponding harmonic approximations.

Chapter 5

Instanton Calculation of Tunnelling Splittings

The ring-polymer instanton formalism can also be used to compute an approximation to the tunnelling splitting that occurs between two degenerate wells (Richardson and Althorpe, 2011). In this chapter we derive this result, first for one-dimensional and then multidimensional systems, giving examples of applications to polyatomic molecules. In Chapter 6 we shall extend the method for systems with more than two degenerate wells and present the results of its application to water clusters. The one-dimensional derivation follows similar steps to that used in the instanton literature (Benderskii et al., 1994), but owing to the relative simplicity of the ring-polymer formulation, it is far simpler to find a practical multidimensional generalization of the method.

Unlike the instanton rate theory based on the $\mathrm{Im}\, F$ premise, the theory presented here is founded on sounder principles. A system with two degenerate wells, such as is shown in Figure 5.1, has its zero-point energy levels E_0 split by the mixing of the two states as a consequence of tunnelling through the barrier. We define the partition function of the system $Q(\beta)$ and that of just one of the wells $Q_0(\beta)$, such that $2Q_0(\beta)$ can be considered the partition function of the system in the absence of tunnelling. In the low temperature

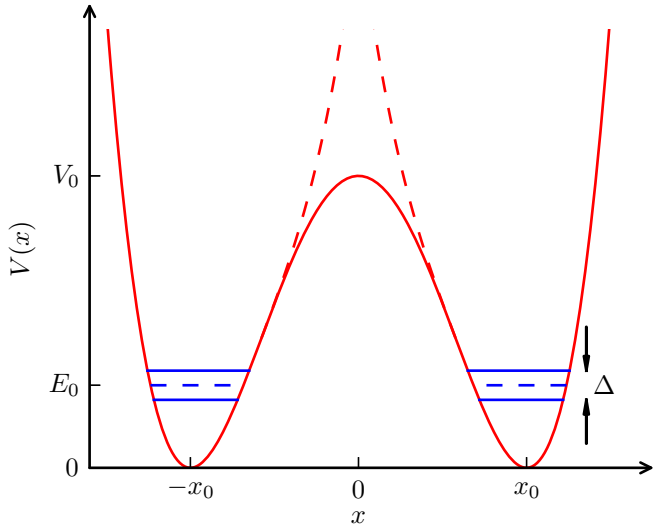

Figure 5.1 – A schematic representation of a double-well potential energy surface (solid red curve) with a tunnelling splitting Δ between its energy levels (solid blue lines) and the non-tunnelling system (dashed red curves) with zero-point energy E_0 (dashed blue lines).

limit at which only the zero-point energy level E_0 is occupied,

$$\lim_{\beta\to\infty} \frac{Q(\beta)}{2Q_0(\beta)} = \lim_{\beta\to\infty} \frac{\mathrm{e}^{-\beta(E_0-\Delta/2)} + \mathrm{e}^{-\beta(E_0+\Delta/2)}}{2\mathrm{e}^{-\beta E_0}} \tag{5.1}$$

$$= \lim_{\beta\to\infty} \cosh\left(\frac{\beta\Delta}{2}\right), \tag{5.2}$$

where $E_0 \pm \Delta/2$ are the energy levels resulting from the splitting. This expression provides the link between the tunnelling splitting which we wish to calculate and the partition functions of the system. It is valid as long as the splitting is much smaller than the energy-level spacing in the non-tunnelling system, which is true as long as the barrier is not too low or thin. The problem has therefore been recast into a computation of the low-temperature limit of partition functions.

5.1 Ring-polymer formulation

We choose to calculate $Q(\beta)$ and $Q_0(\beta)$ in the same vein as in §3.1.1, by the method of steepest descent. There are however a couple of differences between

the earlier application of the method and this. For the rate calculation, a ring-polymer formulation of the *imaginary* part of the partition function was derived using an analytic continuation of the reaction coordinate into the complex plane, such that it was necessary to locate the saddle point on $U_N(\mathbf{x})$. This is not so for the tunnelling-splitting calculations where the minima on the ring-polymer surface are needed to compute a *real* partition function, and in order to formulate the steepest-descent expression for the total partition function, we must take account of all such minima. We first derive an expression for $Q_0(\beta)$, before describing the equivalent formulation of $Q(\beta)$, and thus obtain the splitting Δ.

5.1.1 Non-tunnelling system

The non-tunnelling system is that of two unconnected potential wells with vibrational degrees of freedom and so the only ring-polymer minima which exist are the trivial solutions with the beads collapsed in one of the wells. That is $x_i = \pm x_0$, where $\pm x_0$ are the positions of the potential wells, and in the steepest-descent approximation, it leads to two harmonic vibrational partition functions (see §2.1.1), both of which are

$$Q_0(\beta) \simeq \prod_k \frac{1}{\beta_N \hbar \omega_k} \tag{5.3}$$

$$= \left(\frac{1}{\beta_N \hbar}\right)^N \frac{1}{\sqrt{\det \mathbf{G_0}}}, \tag{5.4}$$

where ω_k^2 (Eq. 2.23) are the eigenvalues of the mass-weighted Hessian, the elements of which are, from Eq. 2.18,

$$(G_0)_{ii'} = \frac{2\delta_{ii'} - \delta_{i\,i'-1} - \delta_{i\,i'+1}}{(\beta_N \hbar)^2} + \omega_\mathrm{s}^2 \delta_{ii'}, \tag{5.5}$$

ω_s is the harmonic frequency of each of the wells, and as before, the beads are cyclic.

5.1.2 Full system

These two solutions also contribute to $Q(\beta)$ as they are also minima in the full system. However, in the low-temperature limit, there are also ring-polymer minima which connect the two wells describing a periodic orbit passing back

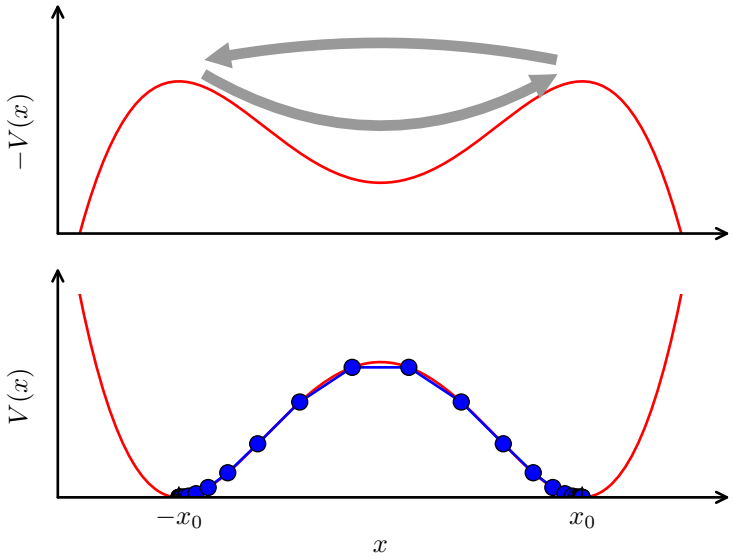

Figure 5.2 – The ring-polymer instanton minimum connecting two wells $\pm x_0$ (lower panel) is equivalent to a finite-difference approximation to the unstable periodic classical trajectory on the upside down surface depicted in the upper panel.

and forth between maxima on the upside down potential (see Figure 5.2). As $\beta \to \infty$ and the amount of imaginary time available to the trajectories increases, the trajectory spends longer and longer waiting almost stationary at $\pm x_0$ for an arbitrarily long stretch of time before embarking on its short journey to the other well. It is for this reason that instantons derive their name: because they occur almost instantaneously compared with the long wait between passes. Each pass called a "kink", and all follow identical trajectories. The number of kinks n in the periodic orbit must be even for the trajectory to be closed. However, n can be infinitely big, and so there is an infinite set of ring-polymer minima which contribute to $Q(\beta)$. Figure 5.3 gives a depiction of some examples of these ring-polymer minima.

We note that, in the long imaginary-time limit, the location of the kinks in the ring polymer is completely arbitrary, and that the instanton acts somewhat like an ideal gas of kinks (Vainshtein et al., 1982). It has also been compared to an infinite periodic Ising model where the system is either at x_0 (spin up) or $-x_0$ (spin down) and kinks exist between neighbouring sites of opposite spins (Polyakov, 1977). In order to calculate the partition function of such a system, one can enumerate over all the instantons with the same

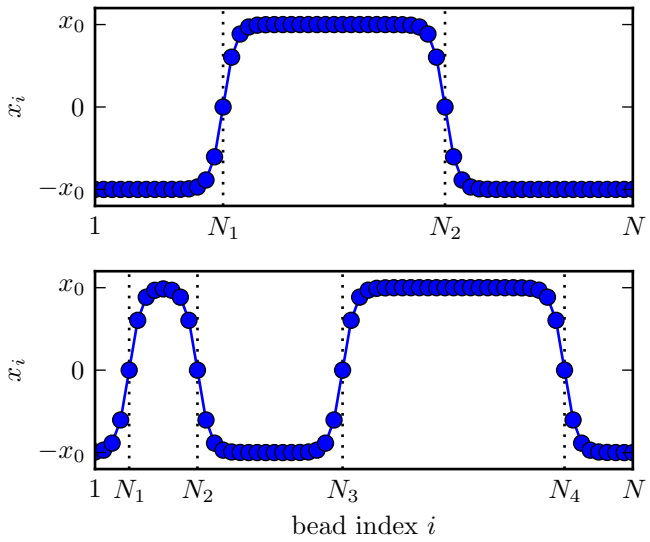

Figure 5.3 – The positions of the beads in a 2-kink (upper) and a 4-kink (lower) ring-polymer instanton which contribute to Q_2 and Q_4 respectively. One bead near the centre of each kink is labelled as is described in the text.

number of kinks n because, as we shall show, they will all contribute equally to the partition function. To proceed, we choose a particular n-kink ring polymer and label the bead at the centre of the first kink N_1, the bead at the centre of the second kink N_2, etc. In the infinite bead limit, the number of equivalent n-kink ring polymers is equal to the number of ways of choosing these n central beads from N in the correct order $N_1 < N_2 < \cdots < N_n$. We find therefore that, in the large-N limit, there are $2N^n/n!$ equivalent n-kink ring-polymer minima which contribute to $Q(\beta)$. The factor of 2 arises because the first bead could be either in the left- or right-hand-side well.

Thus the steepest-descent partition function evaluated over all possible minima can be written

$$\lim_{\beta\to\infty} Q(\beta) = \sum_{\substack{n=0 \\ \text{even}}}^{\infty} \frac{2N^n}{n!} Q_n, \tag{5.6}$$

where each Q_n represents the contribution from any one of the ring-polymer minima with n kinks in the $\beta \to \infty$ limit. As expected, the formula includes the two $n = 0$ minima which correspond to $2Q_0(\beta)$ in the low-temperature limit. This has dramatically reduced the number of minima to be considered

but the calculation is still not tractable in this form and we shall simplify it further.

We would like to compute a steepest-descent approximation to the n-kink partition function which would give something like

$$Q_n = \lim_{\beta\to\infty} \left(\frac{1}{\beta_N \hbar}\right)^N \frac{1}{\sqrt{\det \mathbf{G}}}\, \mathrm{e}^{-\beta_N U_N(\tilde{\mathbf{x}})}, \tag{5.7}$$

where the mass-weighted Hessian matrix (defined in Eq. 2.18) is calculated at the ring-polymer instanton geometry which minimizes Eq. 2.15 and describes n passes through the barrier. However this expression is not correct because, as explained previously in §3.1.1, some of the normal modes have a zero eigenvalue. We deal with this in the next section and correct the result.

5.1.3 Zero-frequency modes

There were no zero-frequency modes of the instanton used in the calculation of $Q_0(\beta)$ because all the beads were collapsed such that no permutational modes existed. However, the 2-kink ring-polymer minimum can be thought of as the $\beta \to \infty$ limit of the instantons of Chapter 3, which had one imaginary mode and one zero-frequency mode corresponding to a cyclic permutation of the beads. As the temperature is lowered, the imaginary mode reduces in magnitude until it becomes zero at $T = 0$, leaving a degenerate pair of zero-frequency modes.

In general, there are as many zero-frequency normal modes s_k as kinks in the instanton, where $k = 1, \ldots, n$, which only appear in the large-N, large-β limit such that, at the ends of the kink trajectory, there are many beads collapsed in the wells. The normal modes describe permutations of beads such that each bead in a kink takes on the position of its neighbour such that the kink, in a similar way to the motion of waves, retains its shape and moves such that a new bead is at its centre. The degenerate modes can be written in any linear combination, one such choice being

$$s_k = \frac{1}{\sqrt{B_M}} \sum_{i\in \mathrm{kink}\, k} (\tilde{x}_{i+1} - \tilde{x}_i) x_i, \qquad k = 1, \ldots, n, \tag{5.8}$$

such that only beads in the k^{th} kink contribute to the mode. The normaliza-

tion constants for these modes are

$$B_M = \sum_{i \in \text{kink } k} (\tilde{x}_{i+1} - \tilde{x}_i)^2. \tag{5.9}$$

Because the energy from Eq. 3.15 is conserved along the instanton trajectory, and we are free to set this to zero, the action from Eq. 3.16 can be written

$$S_{\text{kink}} = \int_{\tau_-}^{\tau_+} m \left(\frac{\mathrm{d}x}{\mathrm{d}\tau}\right)^2 \mathrm{d}\tau \tag{5.10}$$

$$= \lim_{N\to\infty} \frac{mB_M}{\beta_N \hbar}, \tag{5.11}$$

where S_{kink} is the action along just one kink and τ_- and τ_+ are imaginary times just before and after this kink. Using this definition of the normalization constant, the normal modes become

$$s_k = \sqrt{\frac{m}{\beta_N \hbar S_{\text{kink}}}} \sum_{i \in \text{kink } k} (\tilde{x}_{i+1} - \tilde{x}_i) x_i, \qquad k = 1, \ldots, n. \tag{5.12}$$

Rather than using steepest descent to integrate over these modes, we integrate over them analytically. It is readily seen that integrating s_k across the interval 0 to $\sqrt{\beta_N \hbar S_{\text{kink}}/m}$, moves the kink forward by one bead such that each bead i moves from $\tilde{x}_i$ to $\tilde{x}_{i+1}$. We have already enumerated all the possible permutations of the beads in the kinks, and so we need only integrate over this small interval. It is possible to do this analytically because no other terms in the expression depend on these modes. Each zero-frequency mode contributes a factor of $\sqrt{\beta_N \hbar S_{\text{kink}}/m}$ in place of the Gaussian integrals.

Therefore the correct formulation Eq. 5.7 is

$$Q_n = \lim_{\beta\to\infty} \left(\frac{m}{2\pi\beta_N\hbar^2}\right)^{\frac{N}{2}} \left(\frac{\beta_N \hbar S_{\text{kink}}}{m}\right)^{\frac{n}{2}} \prod_k{}' \sqrt{\frac{2\pi}{\beta_N m \eta_k^2}}\, \mathrm{e}^{-\beta_N U_N(\tilde{\mathbf{x}})} \tag{5.13}$$

$$= \lim_{\beta\to\infty} \left(\frac{S_{\text{kink}}}{2\pi\hbar}\right)^{\frac{n}{2}} \left(\frac{1}{\beta_N\hbar}\right)^{N-n} \frac{1}{\sqrt{\det{}' \mathbf{G}}}\, \mathrm{e}^{-\beta_N U_N(\tilde{\mathbf{x}})}, \tag{5.14}$$

where the primes indicate that the n zero frequencies have been removed from the product of eigenvalues.

5.1.4 Expression for the tunnelling splitting

Because the potential can be defined to be zero at $\pm x_0$ where the springs are collapsed, the only contributions to $U_N(\tilde{\mathbf{x}})$ come from the beads in the kinks. That is,

$$U_N(\tilde{\mathbf{x}}) = \frac{nS_{\text{kink}}}{\beta_N \hbar}, \tag{5.15}$$

where S_{kink} is the action along the kink trajectory and can be calculated from the minimum of some *linear*-polymer potential.

We introduce a linear polymer formed of M beads with the coordinates $\mathbf{x} = (x_1, \ldots, x_M)$ described by the potential surface

$$U_M(\mathbf{x}) = \frac{m}{2(\beta_N \hbar)^2} \sum_{i=1}^{M-1} (x_{i+1} - x_i)^2 + \sum_{i=1}^{M} V(x_i). \tag{5.16}$$

Note that we use the same time step $\beta_N \hbar$ as in the N-bead ring-polymer, but redefine β such that the imaginary time available for the instanton is still $\beta\hbar$ and therefore $\beta_N = \beta/M$. The action along the kink is defined as

$$S_{\text{kink}} = \beta_N \hbar U_M(\tilde{\mathbf{x}}), \tag{5.17}$$

where $\tilde{\mathbf{x}}$ is the position of the local minimum of Eq. 5.16 which describes one pass through the barrier. This definition is equivalent to that of Eq. 5.11 in the limit that $\beta \to \infty$ and $\beta_N \to 0$. Checking that the two definitions are equal is a good way of ensuring convergence, but unless specified otherwise, we shall always use Eq. 5.17 as it comes directly from the minimization.

The end-points are not fixed to the bottom of the wells because, although it is possible in one-dimension, one cannot know *a priori* what overall rotation a multidimensional system will undergo along the kink, and therefore exactly to which points to fix the ends. If the correct end points x_{A} and x_{B} are known ($\pm x_0$ in this case), the fixed-ended version can be defined as

$$U_M^{\text{fix}}(\mathbf{x}) = U_M(\mathbf{x}) + \frac{1}{2(\beta_N \hbar)^2} \left[(x_1 - x_{\text{A}})^2 + (x_{\text{B}} - x_M)^2 \right], \tag{5.18}$$

which, when converged, gives the same action as the loose-ended version because the beads are collapsed at the ends of the polymer.

We can also factorize the ratio of determinants of an n-kink ring-polymer minimum and the collapsed ring polymer into contributions from single-kink

linear-polymer minima. The proof is given in Appendix E, but it seems reasonable that when the kinks are separated by long stretches of imaginary time, i.e. when a large density of fully-relaxed beads exists between the kink beads, the fluctuations are decoupled and can be separated out. We write

$$\lim_{\beta\to\infty} \frac{\det' \mathbf{G}}{\det \mathbf{G_0}} = \Phi^{2n}, \tag{5.19}$$

where Φ is the ratio between the frequencies of the instanton and the collapsed state, defined as

$$\Phi = \left(\frac{\det' \mathbf{J}}{\det \mathbf{J_0}} \right)^{\frac{1}{2}}, \tag{5.20}$$

and $\mathbf{J}$ is the mass-weighted Hessian of the fixed-ended linear-polymer potential $U_N^{\text{fix}}(\mathbf{x})$,

$$J_{ii'} = \frac{2\delta_{ii'} - \delta_{i\,i'+1} - \delta_{i\,i'-1}}{(\beta_N \hbar)^2} + \frac{\delta_{ii'}}{m} \frac{\partial^2 V(\tilde{x}_i)}{\partial \tilde{x}_i^2}. \tag{5.21}$$

Here the beads are not cyclic and so the corner elements $J_{1M} = J_{M1}$ are zero. $\mathbf{J_0}$ is the equivalent Hessian for the non-tunnelling system and rather than computing the determinant of this large matrix directly, we instead compute the product of its eigenvalues ω_k^2, which are taken from the exact expression

$$\omega_k = \sqrt{\frac{4}{\beta_N^2 \hbar^2} \sin^2\left(\frac{\pi k}{2M+2} \right) + \omega_{\text{s}}^2}, \qquad k = 1 \ldots M, \tag{5.22}$$

to save unnecessary computation.

It seems that Eq. 5.19 also holds if $\mathbf{J}$ and $\mathbf{J_0}$ are defined from the loose-ended linear-polymer potential $U_N(\mathbf{x})$. However, in this case one looses the ability to compute the eigenvalues of $\mathbf{J_0}$ analytically, making the proof and the computation more complicated.

As M becomes large, numerically computing Φ without care can lead to overflow errors. In practice, we compute the eigenvalues η_k^2 of $\mathbf{J}$ using a banded-matrix eigenvalue solver, remove the single zero frequency η_1, and use the formula

$$\Phi = \frac{1}{\omega_1} \prod_{k=2}^{M} \frac{\eta_k}{\omega_k}. \tag{5.23}$$

Using Eqs. 5.4 and 5.14, we are now able to separate the contributions

from each kink to the partition function as

$$\frac{Q_n}{Q_0} = \theta^n, \tag{5.24}$$

where

$$\theta = \frac{\beta_N \hbar}{\Phi} \sqrt{\frac{S_{\text{kink}}}{2\pi\hbar}}\, \mathrm{e}^{-S_{\text{kink}}/\hbar}, \tag{5.25}$$

and thus the ratio of partition functions (from Eq. 5.6) is

$$\lim_{\beta\to\infty} \frac{Q(\beta)}{2Q_0(\beta)} = \sum_{n=0,\text{even}}^{\infty} \frac{N^n}{n!}\theta^n \tag{5.26}$$

$$= \cosh(N\theta). \tag{5.27}$$

Comparison with Eq. 5.2 gives

$$\Delta = \frac{2}{\beta_N}\theta, \tag{5.28}$$

and therefore the sought-after expression for the tunnelling splitting in terms of the kinks

$$\Delta = \frac{2\hbar}{\Phi} \sqrt{\frac{S_{\text{kink}}}{2\pi\hbar}}\, \mathrm{e}^{-S_{\text{kink}}/\hbar}. \tag{5.29}$$

This formula gives the tunnelling splitting directly from the calculation of just one kink calculated at $\beta \to \infty$ with a large number beads such that the finite-difference step β_N is small enough to describe the trajectory well.

5.2 Numerical implementation

Because the analytic form of the instanton trajectory on a general PES will not be known and must be computed numerically, we shall need to check that the method converges with finite values M and β. In order to show this, numerical tests were performed on the one-dimensional double-well system described by the potential energy surface

$$V(x) = V_0 \left(\frac{x^2}{x_0^2} - 1\right)^2, \tag{5.30}$$

with mass m. The harmonic frequency in the wells is

$$\omega_\mathrm{s} = \sqrt{\frac{V''(x_0)}{m}} = \sqrt{\frac{8V_0}{mx_0^2}}. \tag{5.31}$$

For this particular double-well potential, shown in Figure 5.1, the zero-temperature kink is known exactly (Vainshtein et al., 1982):

$$x(\tau) = \pm x_0 \tanh \frac{\omega_\mathrm{s}}{2}(\tau - \tau_c), \tag{5.32}$$

and the action is

$$S_\mathrm{kink} = \int_{-x_0}^{x_0} \sqrt{2mV(x)}\,\mathrm{d}x = \frac{4}{3}x_0\sqrt{2mV_0}. \tag{5.33}$$

The lowest eigenvalue of the operator corresponding to the Hessian is of course zero, the next largest is $3\omega_\mathrm{s}^2/4$ and the remainder form a continuum such that

$$\Phi = \sqrt{\frac{1}{12\omega_\mathrm{s}^2}}. \tag{5.34}$$

The tunnelling splitting is given by Eq. 5.29.

The ring-polymer instanton method was employed to reproduce these values of the action, ratio and tunnelling splitting. The single-kink minima on the loose-ended linear-polymer surface $U_N(\mathbf{x})$ were located using the L-BFGS algorithm (Zhu et al., 1997) implemented in SciPy (Jones et al., 2001–), starting from an initial geometry of beads evenly spaced between $-x_0$ and x_0. The L-BFGS optimizer had no problems regarding the presence of a zero-frequency mode, which is of course a common situation for geometry optimization of molecular clusters with translational and rotational degrees of freedom. The convergence criterion for minimization was that the norm of the linear-polymer gradient dropped below 10^{-5} (in reduced units).

When β is too small, the kink solution is no longer a minimum on the surface and the optimization may force the linear polymer to collapse into one of the wells. However, if the initial guess is exactly symmetric about the point $x = 0$, and the optimization algorithm cannot break the symmetry, the solution may be a saddle point with one negative eigenvalue, and the turning points of the instanton orbit will be far from the wells. The correct instanton can be found in either case: by lowering the temperature until the negative

eigenvalue becomes close to zero and the minimum geometry is found. When M is too small and the springs are weak, the linear polymer may find a minimum (with no negative eigenvalues) where the beads cross the barrier in one large jump. There is no zero-frequency mode because the imaginary-time step $\beta_N\hbar$ is too large to approximate the trajectory's dynamics. If this occurs, the number of beads should be increased for convergence.

Results from these calculations (starting from a symmetric geometry) are presented in Tables 5.1 and 5.2 where it can be seen that they converge in the $\beta \to \infty$, $\beta_N \to 0$ limit to the results from the theory using the analytic form of the instanton.

Once β is larger than a certain amount, there is a particular diagonal convergence pattern, in which the values of S_{kink} and Φ are dependent only on β_N. Here, doubling both β and M, which keeps $\beta_N = \beta/M$ constant, does not change the linear-polymer minimum geometry at all, except that it adds extra beads to the ends, where they collapse at the bottom of the wells and contribute nothing to either the action or determinant. The computational requirements increase in complexity linearly with M, so in order to find the converged value whilst keeping the computation as small as possible, we find the lowest value of β at which the diagonal convergence pattern is apparent, and then increase M until the answer converges. In this example, it is seen that $\beta\hbar = 30$ provides sufficient time for the kink to connect the two wells whereas $\beta\hbar = 15$ is too short. Tunnelling splittings and the lowest two eigenvalues of the Hessian $\mathbf{J}$ are given in Table 5.3 for $\beta\hbar = 30$ for a range values of M. It is seen that the tunnelling splitting is converged to three significant figures for $M \geq 256$.

We have shown that the new ring-polymer instanton method can be converged to the same result as the instanton theory defined analytically at $T = 0$. However, in both cases there will be errors associated with the steepest-descent approximation. The instanton method captures the anharmonicity of the barrier but does not account for the anharmonicity of the wells. It will be useful to compare the instanton results with the exact solution of the Schrödinger equation. There are many ways of computing the exact quantum results for a one-dimensional system; we chose to compute the Hamiltonian matrix in a basis set of harmonic oscillator wave functions ϕ_n centred at $x = 0$ with widths chosen manually to reduce the size of the basis set needed for convergence. The tunnelling splitting was computed

Table 5.1 – Kink actions S_{kink} for the one-dimensional model of Eq. 5.30 with $x_0 = 5$, $V_0 = 1$ (in reduced units). The actions were calculated using a flexible-ended linear polymer with different numbers of polymer beads M and imaginary time durations $\beta\hbar$. The analytic instanton result (Eq. 5.33) gives $S_{\text{kink}} = 9.428$.

	$\beta\hbar$				
M	15	30	60	120	240
8	9.309	8.762	5.967	3.242	1.655
16	9.381	9.336	8.762	5.967	3.242
32	9.399	9.406	9.336	8.762	5.967
64	9.403	9.423	9.406	9.336	8.762
128	9.404	9.427	9.423	9.406	9.336
256	9.404	9.428	9.427	9.423	9.406
512	9.405	9.428	9.428	9.427	9.423

Table 5.2 – Determinant ratios Φ (in reduced units) corresponding to the kink actions of Table 5.1. The analytic instanton result (Eq. 5.34) gives $\Phi = 0.510$.

	$\beta\hbar$				
M	15	30	60	120	240
8	0.602	0.883	1.455	1.685	1.747
16	0.543	0.600	0.883	1.455	1.685
32	0.532	0.533	0.600	0.883	1.455
64	0.531	0.516	0.533	0.600	0.883
128	0.531	0.512	0.516	0.533	0.600
256	0.532	0.511	0.512	0.516	0.533
512	0.532	0.511	0.511	0.512	0.516

Table 5.3 – Convergence of the tunnelling splitting Δ (in reduced units) obtained from the kink actions and determinant ratios in Tables 5.1 and 5.2 corresponding to $\beta\hbar = 30$. Also shown are the analytic instanton and exact quantum results.

M	η_1^2	η_2^2	$\Delta \times 10^4$
8	6.7(−2)	0.197	4.19
16	2.8(−4)	0.236	3.58
32	−5.0(−7)	0.239	3.77
64	−3.3(−8)	0.240	3.84
128	−1.4(−7)	0.240	3.85
256	1.2(−7)	0.240	3.86
512	−1.0(−7)	0.240	3.86
analytic	0	0.240	3.86
quantum	...	...	3.42

indirectly as the difference between the energies of the two lowest levels. The lowest two wave functions of the system can be expressed as a linear combination of the basis set functions,

$$\Psi^{\pm}(x) = \sum_n c_n^{\pm} \phi_n(x), \tag{5.35}$$

where $c_n^{(\pm)}$ are chosen variationally to minimize the energy resulting from solution of the Schrödinger equation,

$$E^{\pm} = \sum_{ij} c_i^{\pm} H_{ij} c_j^{\pm}, \tag{5.36}$$

where

$$H_{ij} = \int_{-\infty}^{\infty} \phi_i(x) \left[-\frac{\hbar^2}{2m} \frac{\partial^2}{\partial x^2} + V(x) \right] \phi_j(x) \, \mathrm{d}x. \tag{5.37}$$

Following the variational approach of Hückel theory, the energies are minimized when they are eigenvalues of the matrix **H**. The integrals can be calculated analytically for a basis set of harmonic oscillator eigenfunctions and are used to construct **H**, which when diagonalized gives a spectrum of energies of which the lowest is E^+ and the next lowest E^-. The difference between these energies is the tunnelling splitting Δ.

Table 5.4 – Comparison of the instanton tunnelling splittings Δ (in reduced units) with the exact quantum splittings for different barrier heights V_0 in the model of Eq. 5.30 (with $x_0 = 5\sqrt{V_0}$). Note that the harmonic zero-point energy in the potential wells is 0.283 (reduced units).

	V_0			
	2	1	0.5	0.25
instanton	4.39(−8)	3.86(−4)	3.04(−2)	2.27(−1)
quantum	4.15(−8)	3.42(−4)	2.25(−2)	1.19(−1)
error	6%	13%	35%	91%

Table 5.4 shows the error implicit in the instanton approach caused by the steepest-descent approximation for a series of values of the barrier height. It is seen that for systems with high barriers, the instanton method performs much better than for those with low barriers. This is because, in the latter case, the well is more anharmonic over a short range and, for example, fluctuations of the linear-polymer collapsed in a well may even include paths which access the top of the barrier and visit the other well. This fluctuation is obviously poorly represented in the steepest-descent approximation. One could say that tunnelling was no longer a rare event, and that the validity of Eq. 5.2 breaks down if we are unable to define a non-tunnelling system. However, even for the lowest barrier tested, which is lower than the harmonic zero-point energy of the wells, the instanton splitting is still within a factor of 2 of the exact quantum result.

5.3 Extension to multiple dimensions

It is possible to generalize the ring-polymer instanton approach to calculate the tunnelling splitting in polyatomic molecules or clusters. We assume that the tunnelling occurs between two degenerate wells on the multidimensional potential energy surface. Systems with more than two wells and more complicated tunnelling-splitting patterns will be treated in Chapter 6.

A related multidimensional instanton method was derived by Mil'nikov and Nakamura (2001) who also showed that the derivation could be reproduced by a WKB approach. They made use of a method to locate the instanton using minimization techniques using a functional basis set to describe the trajectory, and because they did not make use of a ring-polymer

formulation, the derivation of the prefactor included far more complicated mathematics.

Molecules and clusters will also exhibit rotational spectra alongside the vibrational spectra which includes the tunnelling splittings (Atkins and Friedman, 2005, §10.3). In the case of a symmetric rotor, the rotational energy levels are identified by the total-angular-momentum quantum number J and the quantum number signifying the projection onto the principal axis, $K = 0, \pm 1, \ldots, \pm J$. The energy levels of spherical rotors, however, for which the three principle moments of inertia are equal, do not depend on K and in the case of linear rotors, only $K = 0$ is allowed. Each of these energy levels $E_{J,K}$ is degenerate and can take $2J + 1$ values of M_J (the projection onto a laboratory-fixed axis). An asymmetric rotor also has quantized energy levels but it is not possible to describe them in such a general way. However, our derivation below applies equally well to all types of rotor.

Because of Coriolis and centrifugal-distortion effects, the rotational and vibrational modes will be coupled together, which will affect the tunnelling splittings. There is therefore a progression of tunnelling splittings $\Delta(J, K)$ for each rotational level. Since it is often true that the rotational energy spacing is of the same order of magnitude as the tunnelling splitting, we cannot neglect all but the lowest rotational level at low temperature as was done for the vibrational levels. However, in most systems where we intend to treat the rearrangements of hydrogen atoms but with an almost fixed skeleton of heavier atoms, we expect the dependence on J and K to be small at low energies, and assuming a constant value for Δ over the required energy range gives

$$\lim_{\beta\to\infty} \frac{Q(\beta)}{2Q_0(\beta)} = \frac{\sum_J \sum_K \left[\mathrm{e}^{-\beta(E_{J,K}-\Delta/2)} + \mathrm{e}^{-\beta(E_{J,K}+\Delta/2)}\right]}{2\sum_J \sum_K \mathrm{e}^{-\beta E_{J,K}}} \tag{5.38}$$

$$= \cosh\left(\frac{\beta\Delta}{2}\right), \tag{5.39}$$

which is exactly what was found before. The instanton approach does not therefore require any modification in order to treat systems with rotational spectra although it should be understood that it computes an average, rotation-free tunnelling splitting.

The multidimensional formulation of the linear-polymer potential is

$$U_M(\mathbf{x}) = \sum_{j=1}^{f} \frac{m_j}{2(\beta_N \hbar)^2} \sum_{i=1}^{M-1} (x_{i+1,j} - x_{i,j})^2 + \sum_{i=1}^{M} V(x_{i,1}, \ldots, x_{i,f}), \quad (5.40)$$

and the fluctuation matrix corresponding to a single-kink minimum is given by

$$J_{ijj'j'} = \frac{2\delta_{ii'} - \delta_{i\,i'+1} - \delta_{i\,i'-1}}{(\beta_N \hbar)^2} \delta_{jj'} + \frac{\delta_{ii'}}{\sqrt{m_j m_{j'}}} \frac{\partial^2 V(\tilde{x}_{i,1}, \ldots, \tilde{x}_{i,f})}{\partial \tilde{x}_{i,j} \partial \tilde{x}_{i,j'}}. \quad (5.41)$$

The minimization procedure automatically locates kinks with zero linear and angular momentum. The centre of mass of the molecule, therefore, will be fixed along the entire path. However, it is not possible to know *a priori* the rotational arrangement of the end-point relative to the start without first computing the entire pathway. It is for this reason that the loose-ended linear-polymer potential is used in the minimization. The molecule performs as little rotation as possible, and is stationary at the ends of the path. It is simple to check the pathway using a molecular visualization package by creating a movie of the trajectory in imaginary time with each frame showing the M replicas in turn.

The greatest approximation involved in this method is probably still that of only including the harmonic fluctuations. The anharmonicity is of course included along the kink pathway (without it, no tunnelling splitting could exist) but perpendicular to this, the harmonic approximation is used. Note that this separation of degrees of freedom is performed automatically by the optimization and is not an *a priori* reduction of dimensionality.

5.4 Numerical applications

Here we apply the multidimensional theory to the standard test cases of the hydroperoxyl radical HO_2 and malonaldehyde to compare results with the method of Mil'nikov and Nakamura (2001). There have been many studies made of the tunnelling splitting in malonaldehyde by a variety of methods. Tautermann et al. (2002*a*) located the optimal semi-classical pathway using a simulated annealing approach. The splitting was calculated on an *ab initio* surface by the method of DMC (Wang and Bowman, 2008) and also by using

an exact method on a one-dimensional Hamiltonian in the imaginary-mode of the saddle point (Wang et al., 2008). MCTDH has also been used to compute the tunnelling splitting (Hammer et al., 2009) but was not able to employ an *ab initio* PES owing to the numerical effort which would be required.

The ring-polymer instanton approach which we shall apply is able to treat large systems in full dimensionality with expensive potentials. However, here we just apply the method to the same empirical malonaldehyde surface as was used by Mil'nikov and Nakamura (2001) in an attempt to reproduce their results, and leave applications to *ab initio* surfaces to the treatment of water clusters in the following chapter.

For both systems, we used Cartesian coordinates and included all degrees of freedom. The initial instanton geometry guess was chosen to be a linear interpolation between the two wells but once an instanton had been computed for a small number of beads, to reduce the number of iterations needed in each optimization, starting geometries based on previous optimized solutions were used, in the same way as was described in §3.4.2. This was done by forming a 2-kink ring polymer from the single-kink linear polymer by inserting a new bead in the position of each bead in the kink such that it doubles back on itself. The ring was transformed from Cartesian to free-ring-polymer normal-mode coordinates (Eq. 2.22), the array doubled in length by padding the high-frequency normal modes with zeros, multiplied by $\sqrt{2}$ (for the normalization), and transformed back to Cartesian coordinates to give a ring polymer which follows the same path as before but has half the time step $\beta_N\hbar$ between beads. The single-kink is easily extracted from this ring polymer by removing the doubled-back beads, and it is this linear polymer which is used as the starting geometry for the next minimization.

Using this method for choosing starting geometries dramatically reduces the number of iterations needed for high-M calculations. The minimizations were again performed using the L-BFGS algorithm.

The Hessian $\boldsymbol{\nabla}^2 V$ at the geometry of each bead was computed numerically and these were used to construct the mass-weighted Hessian or fluctuation matrix $\mathbf{J}$ of the linear-polymer. A banded-matrix linear algebra routine was used to compute the eigenvalues of which only one should be zero. In this case, the translational and rotational modes are not zero because it is the Hessian of the fixed-ended linear polymer which is computed. These

Table 5.5 – Kink actions S_{kink} and determinant ratios Φ in atomic units calculated for HO_2, as a function of the number of beads M and the imaginary-time duration $\beta\hbar$.

		$\beta\hbar$ / a.u.			
	M	1200	2400	3600	4800
Action	32	28.63	28.47	27.53	25.86
	64	28.67	28.69	28.61	28.47
	128	28.68	28.74	28.72	28.69
	256	28.69	28.75	28.74	28.74
	512	28.69	28.75	28.75	28.75
	1024	28.69	28.75	28.75	28.75
Ratio	32	46.4			
	64	45.8	44.5	45.9	
	128	45.8	43.7	44.1	44.6
	256	45.8	43.6	43.7	43.9
	512	45.8	43.4	43.6	43.7
	1024	45.8	43.5	43.6	43.6

instead form M discernible sets of six degenerate modes spaced throughout the eigenvalue spectrum. Only one eigenvalue, that of the permutational mode, should be lower than the lowest of these degenerate sets, and unless this was found to be true, the instanton was deemed not to be converged, and the value of Φ was not computed.

5.4.1 HO_2

The HO_2 calculations were performed on a double many-body expansion surface (DMBE) (Pastrana et al., 1990). The minimum-energy geometry for this molecule has a bent HOO configuration and the tunnelling pathway is well known to consist mainly of motion of the hydrogen atom from one oxygen to the other. This is accompanied by a small movement of the heavier oxygen atoms, which is necessary to conserve linear and angular momentum.

Table 5.5 gives the actions S_{kink} and determinant ratios Φ computed for different values of M and β. The same diagonal convergence pattern appears as in the one-dimensional case (§5.2), namely that once β is sufficiently large that the kink has sufficient imaginary time to connect the two wells, the results depend only on the imaginary-time step $\beta_N\hbar = \beta\hbar/M$. Table 5.5 shows that this stage is reacted when $\beta\hbar \geq 3600$ a.u. and that $\beta_N\hbar \leq 7$ a.u.

Table 5.6 – Tunnelling splittings Δ for HO_2 as a function of the number of beads M, obtained from the actions and ratios of Table 5.5 corresponding to $\beta\hbar = 3600$ a.u. Also shown are the instanton and exact quantum results of Mil'nikov and Nakamura (2001).

M	$\Delta \times 10^9/\mathrm{cm}^{-1}$
64	7.6
128	7.2
256	7.1
512	7.0
1024	7.0
inst.	6.3
quantum	6.2

is sufficient for numerical convergence.

As shown in Table 5.6, the tunnelling splitting Δ was calculated as $7.0 \times 10^{-9}\,\mathrm{cm}^{-1}$ in good agreement with the exact quantum result for the DMBE surface of $6.2 \times 10^{-9}\,\mathrm{cm}^{-1}$. This level of agreement is excellent, given the approximations made in the instanton approach. Our calculated value of Δ differs from the instanton result of Mil'nikov and Nakamura (2001) by about 10%. However, the latter was obtained using the exact $J = 0$ Hamiltonian, whereas our value, as mentioned above, is obtained by making the approximation that the rotation and tunnelling dynamics are separable. This may account, at least in part, for the difference between these two instanton results.

5.4.2 Malonaldehyde

The calculations were performed on the full-dimensional surface of Sewell et al. (1995), with the planar part of the surface modified to be equal to that of Guo et al. (1994) as was done by Mil'nikov and Nakamura (2001). Figure 5.4 shows the minimum-energy geometry calculated for this molecule.

One of the instantons calculated is plotted in Figure 5.5 in which it can be seen how the potential varies along the pathway. Unlike for the system described in §5.2, the potential is very flat at the ends of the pathway owing to a skeletal rearrangement of the heavier carbon and oxygen atoms which is necessary to ensure that the pathway starts and ends at the degenerate well minima. This makes the calculations more challenging as many beads

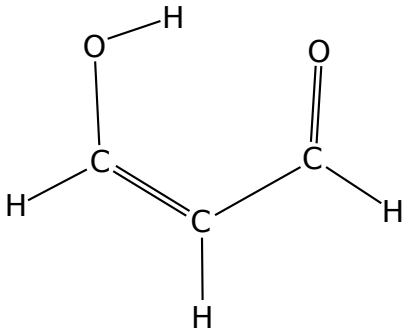

Figure 5.4 – The minimum-energy geometry of malonaldehyde which is planar. The tunnelling involves the hydrogen transferring between the two oxygen atoms.

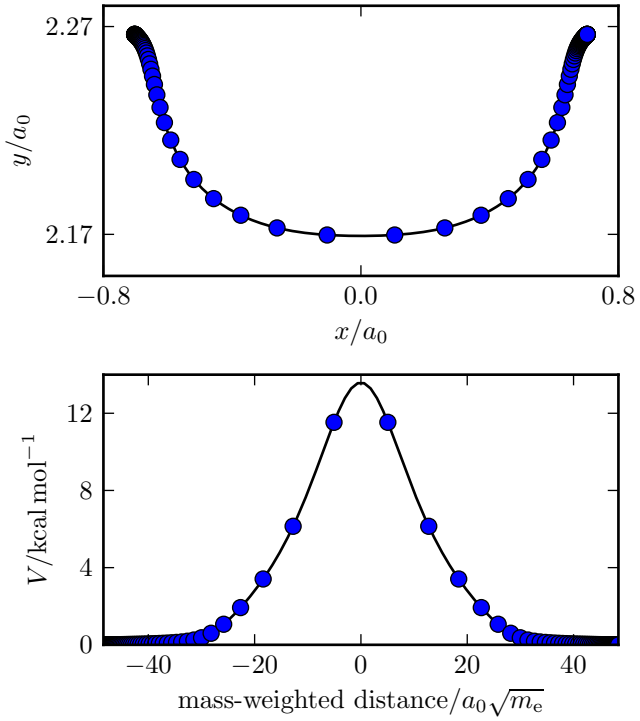

Figure 5.5 – The two plots represent the beads in linear-polymer instantons calculated for malonaldehyde with $\beta\hbar = 6000$ a.u. and $M = 128$ (blue circles) and 1024 (all beads merged into a solid black curve). The upper panel shows the Cartesian positions of the tunnelling hydrogen atom, with the origin located at the centre of mass of the molecule and the coordinates x and y located in the plane of all the atoms. The lower panel shows the spread of the beads along the kink trajectory and the value of potential $V(x_{i,1}, \ldots, x_{i,f})$ at each bead.

Table 5.7 – Kink actions S_{kink} and determinant ratios Φ in atomic units calculated for malonaldehyde as a function of the number of beads M and the imaginary-time duration $\beta\hbar$.

		$\beta\hbar$ / a.u.			
	M	3000	6000	9000	12000
Action	64	8.03	7.82	7.40	6.98
	128	8.06	8.07	7.98	7.82
	256	8.06	8.10	8.09	8.07
	512	8.06	8.10	8.10	8.10
	1024	8.06	8.11	8.11	8.11
Ratio	64				
	128	2.97			
	256	2.92	3.04		
	512	2.92	2.99	2.98	
	1024	2.91	2.98	2.95	2.94

are needed for numerical convergence. For instance, Figure 5.5 shows that even with 128 beads, only a handful are located near the barrier top and cannot therefore describe the zero-frequency normal mode s_1 correctly. In malonaldehyde, this normal mode describes two types of motion with different timescales: the slow rearrangement of the CCO bond angles and the ends of the kink, and the rapid transfer of the hydrogen atom in the middle section. It is a noticeably different pathway from that of the minimum-energy path which passes through a transition state of only 10 kcal/mol but involves far more skeletal rearrangement leading to a wider effective barrier and a higher action than the instanton pathway.

There are a number of ways that this convergence could be improved by analogy with methods used to separate timescales in molecular dynamics simulations. To reduce the number of beads needed, one could use larger time steps at the ends of the pathways as has been done for the saddle-point ($\operatorname{Im} F$ rate theory) instantons (Rommel and Kästner, 2011). A related approach which enforces the beads to be evenly spaced in position rather than time is a reformulation of the action (cf. §1.2) in Hamilton-Jacobi form (Faccioli et al., 2006). The difficulty here arises because one needs a penalty function to force the beads to be evenly spaced, but because the length of the path, and hence the spacing of the beads, is not known before optimization, the penalty depends on the average spacing and therefore couples all the beads

Table 5.8 – Tunnelling splittings Δ for malonaldehyde as a function of the number of beads M, obtained from the actions and ratios of Table 5.7 corresponding to $\beta\hbar = 6000$ a.u. Also shown is the instanton result of Mil'nikov and Nakamura (2001).

M	Δ/cm^{-1}
256	50
512	50
1024	51
inst.	58

together (rather than just nearest neighbours) which decreases the efficiency of the minimization algorithm. Calculation of the determinant is no easier as the zero-frequency mode is not an eigenvector of the Hessian unless the beads are just as closely spaced as in the original formulation. These problems and ideas are left for future work.

However, despite this difficulty, it is still possible to converge the actions and determinant ratios by adding enough beads, as is shown in Table 5.7, and the calculations reported here were fairly quick, even using 1024 beads in each degree of freedom (and therefore a minimization with 27 648 degrees of freedom). As was seen for the one-dimensional and HO_2 calculations above, the diagonal convergence pattern appears for $\beta\hbar \geq 6000$ a.u., and only an imaginary-time step of $\beta_N\hbar \leq 24$ a.u. describes the s_1 mode sufficiently well that its eigenvalue is lower than all the other modes such that it can be identified and removed. The tunnelling splitting Δ was calculated to be 51 cm^{-1} (see Table 5.8) which is in reasonable agreement with the value of 58 cm^{-1} obtained in the instanton calculation of Mil'nikov and Nakamura (2001). The disagreement between these two sets of instanton results is probably the result of the different ways in which the two calculations treat the overall rotation of the molecule. Our calculations assume that the rotational parts of the partition functions cancel in the ratio $Q(\beta)/2Q_0(\beta)$ whereas the calculations of Mil'nikov and Nakamura (2001) use an approximate $J = 0$ Hamiltonian, obtained by fixing the axes with respect to the two oxygen atoms and the tunnelling hydrogen.

The results are in reasonable agreement with the experimental value of the tunnelling splitting, 21.6 cm^{-1} (Firth et al., 1991), given the approximate quality of the potential surface. The isotope ratio of the proton-transfer to

the deuteron-transfer tunnelling splittings is calculated to be 6.8, in good agreement with that of Mil'nikov and Nakamura (2001) which was 6.7 and with the experimental result of 7.4 (Baughcum et al., 1984). Exact quantum results are not available for this surface, but we note that instanton results (Mil'nikov et al., 2004) obtained on a different potential surface (Yagi et al., 2001) are within a factor of 1.5 of accurate quantum results (Hammer et al., 2009). Similar agreement could thus be expected between the results of Table 5.8 and exact quantum results on the same surface.

Chapter 6

Tunnelling Splittings in Water Clusters

The derivation of the ring-polymer instanton method outlined in the previous chapter was based on a system where tunnelling occurred between two degenerate wells. In order to make a study of the tunnelling splitting in water clusters, it is necessary to extend the method to treat tunnelling between any number of wells (Richardson et al., 2011). The result is that the splitting pattern can be calculated as the eigenvalues of a Hückel-type matrix, each element of which corresponds to an instanton calculated as before between two wells. In the author's knowledge, this generalization has not been done before using any form of instanton or path-integral theory.

In this chapter, the generalization of the method is described and applied to the specific examples of water dimer, trimer and octamer in turn. Other methods which have been applied to computing tunnelling splittings in water clusters are also reviewed in the following sections.

6.1 Generalization of the ring-polymer instanton method

The zero-point energy E_0 for a molecular system with G degenerate wells, between which tunnelling takes place, splits into a set of G levels $\{E_\nu\}$ which cannot in general be described by a single tunnelling splitting Δ. Following

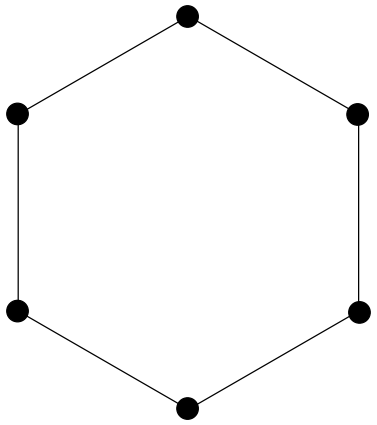

$$\mathbf{A} = \begin{pmatrix} 0 & 1 & 0 & 0 & 0 & 1 \\ 1 & 0 & 1 & 0 & 0 & 0 \\ 0 & 1 & 0 & 1 & 0 & 0 \\ 0 & 0 & 1 & 0 & 1 & 0 \\ 0 & 0 & 0 & 1 & 0 & 1 \\ 1 & 0 & 0 & 0 & 1 & 0 \end{pmatrix}$$

Figure 6.1 – Example graph of potential wells connected by kinks and the associated adjacency matrix $\mathbf{A}$.

this definition, Eq. 5.2 generalizes to

$$\lim_{\beta\to\infty} \frac{Q(\beta)}{GQ_0(\beta)} = \lim_{\beta\to\infty} \frac{1}{G} \sum_{\nu=1}^{G} \mathrm{e}^{-\beta(E_\nu - E_0)}. \tag{6.1}$$

As in the previous chapters, we intend to take the steepest-descent approximation of the ring-polymer formulation of the partition functions. The low-temperature limit of the partition function of the tunnelling system $Q(\beta)$ evaluated by the method of steepest descent can be divided into contributions from each ring-polymer minimum (see §5.1.2). This set of minima, or periodic orbits, includes a subset which start (and end) in each of the wells ν but may take any number of kinks and pass through any number of the other wells on the way, as they have an infinite amount of imaginary time available.

For enumerating these ring polymers, it can be useful to make an analogy with some standard results of graph theory. Figure 6.1 shows the graph representation of an example system where the potential wells are depicted by vertices and kinks by edges (Wilson, 1996). The sequence of kinks and wells visited by the ring-polymer minima are described by closed walks taken along the edges between the vertices. As before, there is also a factor of $N^n/n!$ (which is neglected in the graph-theory representation) to account for the number of ways of arranging the beads in the ring-polymer minimum while still tracing the same sequence of kinks. If we define $Q_{n,\nu}$ as the contribution

of the closed paths of n kinks which start and finish at well ν, we may write

$$\lim_{\beta\to\infty} Q(\beta) = \sum_{\nu=1}^{G}\sum_{n=0}^{\infty}\frac{N^n}{n!}Q_{n,\nu}. \tag{6.2}$$

To count the total number of different sequences of n kinks, that is in the parlance of graph-theory, the number of distinct walks which start and finish at a particular vertex, we use the *adjacency matrix* $\mathbf{A}$ which is defined such that $A_{\lambda\mu}$ is equal to the number of edges between vertices λ and μ. Therefore the elements of the adjacency matrix $A_{\lambda\mu}$ give the number of single-kink pathways which directly connect the wells λ and μ.* In the same way, it is seen that $\sum_{\kappa=1}^{G} A_{\lambda\kappa}A_{\kappa\mu}$ provides the number of sequences of two kinks which connect the wells λ and μ via any intermediate κ. And indeed $(\mathbf{A}^n)_{\lambda\mu}$ is the number of possible sequences connecting these wells in n kink-steps (Bondy and Murty, 1976, §1.6). We require only pathways that start and end in the same well for the partition function and therefore use the formula $(\mathbf{A}^n)_{\nu\nu}$ to count them.

Following the arguments given in §5.1, we can factorize the contribution to $Q_{n,\nu}$ made by each n-kink orbit into a product of n weights $\theta_{\lambda\mu}$ each associated with a different kink in the sequence. The $\theta_{\lambda\mu}$ are defined analogously to θ in Eq. 5.25, such that the action S_{kink} is that of the kink joining λ to μ and the ratio Φ is obtained from the normal mode frequencies of the linear polymer representing this kink, as described by Eq. 5.20. To obtain the total weight associated with all the n-kink orbits which contribute to $Q_{n,\nu}$, we define the *tunnelling matrix* $\mathbf{W}$ by

$$W_{\lambda\mu} = A_{\lambda\mu}h_{\lambda\mu}, \tag{6.3}$$

where

$$h_{\lambda\mu} = -\frac{1}{\beta_N}\theta_{\lambda\mu}. \tag{6.4}$$

It then follows that

$$\frac{Q_{n,\nu}}{GQ_{0,\nu}} = \frac{1}{G}[(-\beta_N\mathbf{W})^n]_{\nu\nu}, \tag{6.5}$$

*When $A_{\lambda\mu} > 1$, we shall assume that these kinks can be mapped onto one another by symmetry operations. The treatment could be generalized for systems where more than one kink joined a pair of wells along pathways unrelated by symmetry. However, it will probably be common that one kink will have a low action and will dominate, in which case the other higher-action kinks can be neglected.

since the adjacency matrix element $A_{\lambda\mu}$ in $W_{\lambda\mu}$ ensures that the quantity $[(-\beta_N \mathbf{W})^n]_{\nu\nu}$ is the sum over the weights $\theta_{\lambda\mu}$ associated with all orbits contributing to $Q_{n,\nu}$. We thus obtain

$$\begin{aligned}\lim_{\beta\to\infty} \frac{Q(\beta)}{GQ_0(\beta)} &= \frac{1}{G}\sum_{n=0}^{\infty}\frac{N^n}{n!}\sum_{\nu=1}^{G}[(-\beta_N\mathbf{W})^n]_{\nu\nu} \\ &= \frac{1}{G}\,\mathrm{tr}\left[\mathrm{e}^{-\beta\mathbf{W}}\right]. \end{aligned} \tag{6.6}$$

Comparison with Eq. 6.1 reveals that the eigenvalues of $\mathbf{W}$ give the desired approximations to the energy splittings $E_\nu - E_0$.

This general formulation is consistent with the method presented in Chapter 5 for a $G = 2$ system, for which

$$\mathbf{A} = \begin{pmatrix} 0 & 1 \\ 1 & 0 \end{pmatrix} \tag{6.7}$$

and

$$\mathbf{W} = -\frac{1}{\beta_N}\theta\mathbf{A}. \tag{6.8}$$

Substitution into Eqs. 6.1 and 6.6 then yields the same identity as was found before:

$$\lim_{\beta\to\infty}\frac{1}{2}\sum_{\nu=1}^{2}\mathrm{e}^{-\beta(E_\nu-E_0)} = \frac{1}{2}\,\mathrm{tr}\left[\mathrm{e}^{N\theta\mathbf{A}}\right] \tag{6.9}$$

$$\lim_{\beta\to\infty}\frac{\mathrm{e}^{-\beta(E_1-E_0)}+\mathrm{e}^{-\beta(E_2-E_0)}}{2} = \frac{1}{2}\,\mathrm{tr}\sum_{n=0}^{\infty}\frac{(N\theta)^n}{n!}\mathbf{A}^n \tag{6.10}$$

$$\lim_{\beta\to\infty}\cosh\left(\beta\Delta/2\right) = \cosh\left(N\theta\right), \tag{6.11}$$

since $\mathrm{tr}\,[\mathbf{A}^n]$ is equal to 0 when n is odd and to 2 when n is even and $\Delta/2 = E_2 - E_0 = E_0 - E_1$ (see Figure 5.1). The eigenvectors of $\mathbf{W}$ are $(1, \pm 1)/\sqrt{2}$, demonstrating that the wells contribute symmetrically in the lower state and antisymmetrically in the upper state as expected.

For more complex systems with more than two wells, the molecular symmetry group comprising all feasible permutation-inversion operations, that is those which can be achieved without passing over insuperable energy barriers (Longuet-Higgins, 1963), can be used to find the set of G wells between which kinks can be computed. This is kept low by excluding all

pathways which are compelled to break strong bonds or rearrange heavy atoms as the kinks describing these rearrangements will have large actions and a negligible effect on the tunnelling-splitting pattern. There are G^2 elements of $\mathbf{W}$ but only a few matrix elements $h_{\lambda\mu}$ need be computed because many of them are related by symmetry and thus contribute identical factors. Because by definition all the wells are degenerate and have the same topology, we only have to consider kinks between any one well and each of the others. This implies that the maximum number of matrix elements which must be calculated is only $G - 1$.

If more than one symmetrically-equivalent kink joins a pair of wells, only one need be computed and the adjacency matrix is defined to account for this degeneracy. In general it is necessary to perform a linear-polymer minimization before one can know whether kinks will have symmetric partners. Creating a plot of the potential at the geometry of each bead, viewing the kink in a molecular visualization package (with each bead represented by a time step) and identifying the symmetry elements of the molecular geometry both in the wells and along the pathways can be useful to check for this. A further use of symmetry is that the eigenvectors of $\mathbf{W}$ span the same irreducible representations as the corresponding wave functions (since they give the signs and magnitudes of the contributions made by the various wells), and can hence be used to assign the symmetry labels to the energy levels E_ν.

This completes the extension of the ring-polymer instanton method of Chapter 5 to treat tunnelling between more than two wells. A similar approach to define the tunnelling matrix $\mathbf{W}$ has been used previously (Coudert and Hougen, 1988; Wales, 1993*b*), in particular in conjunction with the WKB method (Watanabe et al., 2004; Takahashi et al., 2005) starting from an *a priori* model of the tunnelling. The difference is that these methods compute the matrix elements along one-dimensional predefined tunnelling paths, unlike the ring-polymer instanton method which obtains $\mathbf{W}$ completely from first principles. In the author's knowledge, this is the first time that the path-integral (Marchi and Chandler, 1991) or instanton approach, in either its functional-determinant (Vainshtein et al., 1982; Mil'nikov and Nakamura, 2001) or ring-polymer form (Chapter 5), has been generalized to treat tunnelling splittings in systems with more than two wells.

In the following sections, this extended ring-polymer instanton approach

is applied compute the tunnelling-splitting patterns of a selection of water clusters including the dimer, trimer and octamer. The other water clusters, on which we reflect briefly below, are left for future work.

6.2 Application to water dimer

The water dimer $(H_2O)_2$ and its isotopomer $(D_2O)_2$ provide ideal test cases for the ring-polymer instanton method as the splitting pattern is non-trivial but well understood (Dyke, 1977; Coudert and Hougen, 1988), and the various tunnelling splittings span four orders of magnitude. The dimer has been studied extensively by spectroscopy to quantify the experimental splitting pattern (Fraser et al., 1989; Zwart et al., 1991) as well as its deuterated form (Suenram et al., 1989; Karyakin et al., 1993; Paul et al., 1998). Many theoretical studies have also computed the tunnelling splittings for the dimer using a range of techniques including the direct solution of the Schrödinger equation with either fixed monomers (Althorpe and Clary, 1994, 1995; Fellers et al., 1999; Chen et al., 1999; Groenenboom et al., 2000; Huang et al., 2008) or an adiabatic separation of the intermolecular and intramolecular modes (Leforestier et al., 2002). There have also been approaches based on model Hamiltonians (Coudert and Hougen, 1988), diffusion Monte Carlo (Gregory and Clary, 1995*a*), and the WKB approximation (Watanabe et al., 2004). We were able to use a selection of different potential energy surfaces and compare the ring-polymer instanton results to these experimental and theoretical splittings, providing a good test for the quality both of the method and of the potentials.

It is well-known that the water dimer's minimum geometry has a "trans-linear" geometry with C_s symmetry (Dyke et al., 1977) as depicted in Figure 6.2. The water molecule whose hydrogen atom forms a hydrogen bond is called the *donor* monomer; the other is the *acceptor*. The molecular symmetry group of the water dimer predicts that there are $G = 8$ degenerate isomers connected by feasible pathways, i.e. those which do not break covalent bonds (Dyke, 1977), and that only five of these pathways are not related by symmetry. These permutation-inversion isomers are usually labelled $\nu = 1, \ldots, 8$ (Coudert and Hougen, 1988), with the geometry of well $\nu = 1$ taken to be that of Figure 6.2. The geometries of the other seven wells can be generated from this by applying elements of the molecular symmetry group

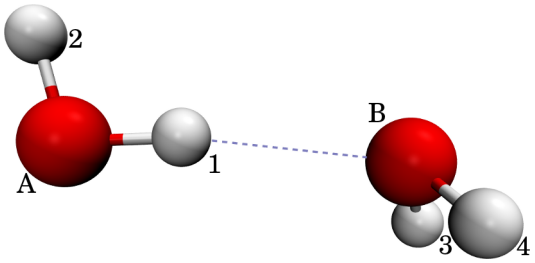

Figure 6.2 – The minimum-energy geometry of the water dimer labelled so as to represent well $\nu = 1$.

(Longuet-Higgins, 1963).

Only five elements of the tunnelling matrix **W** are independent and need to be calculated by the instanton method. They are by convention taken to correspond to tunnelling between wells $1 \to \nu$, with $\nu = 2, 3, 4, 5, 7$ (Coudert and Hougen, 1988).

The three most important (for the splitting pattern) low-lying transition states of the water dimer were first studied by Smith et al. (1990) using *ab initio* potential energy surfaces, and the unconstrained minimum-energy pathways for these rearrangements were calculated by Wales (1999). The instanton approach, however, is able to locate the minimum-action pathways for all five rearrangements, some of which are similar but not equivalent to the minimum-energy pathways, as we shall show.

6.2.1 The potential energy surface

The correct water dimer potential energy surface is known to be difficult to reproduce (Millot et al., 1998) so before attempting to calculate kinks, it is expedient to test for the correct topology of the potentials.

We attempted to locate the minimum-energy geometry and the lowest four transition states using the following potentials:

HBB2

This recently-developed water dimer PES (Shank et al., 2009) is based on a fitting of about 30 000 CCSD(T) *ab initio* single-point energies with a correction at long range to reproduce the experimental dissociation energy. Invariance with respect to permutations of identical atoms is built in fundamentally to the definition. Quantum calculations on the HBB1 surface (Huang et al., 2008), of which HBB2 is a refinement,

give a splitting pattern in close agreement with experiment. This is the most accurate, and also the most computationally expensive, of the potentials described here.

CC-pol-8s

Cencek et al. (2008) fitted this rigid-monomer water dimer potential to 2510 *ab inito* points using a functional form to describe the interactions between eight sites on each of the monomers. Quantum calculations on this PES are also in close agreement with experiment. However, a flexible-monomer version has not yet been constructed.

TTM3-F

The flexible, polarizable, Thole-type model potential of Fanourgakis and Xantheas (2008) was parameterized to describe the vibrational spectra of a selection of water clusters and also of liquid water.

VRT(MCY-5f)

This empirical potential is designed only to describe the water dimer and is based on the rigid-molecule MCY functional form (Matsuoka et al., 1976) and a flexible-monomer potential. It was parameterized such that a pseudo-spectral Hamiltonian method, using an adiabatic separation between the slow and fast modes, would produce the experimental vibrational-rotational energy levels including the tunnelling-splitting pattern (Leforestier et al., 2002).

q-TIP4P/F

This is a flexible version of the commonly-used four-site empirical TIP4P water potential which has been parameterized by Habershon et al. (2009) to give the correct liquid structure, diffusion coefficient and infrared absorption frequencies in the bulk from ring-polymer simulations.

RWK

This multipolar empirical dimer potential described by Coker and Watts (1987) is based on very simple functions, and can be used in a flexible or rigid form. It was commonly used for computations of the tunnelling-splitting pattern before the potentials described above were developed.

The HBB2 potential is expected to be the most accurate but is also considerably slower to compute than the others. However, most optimizations were still completed in less than 24 hours on a single CPU. All the potentials tested located a global minimum with the correct structure and symmetry. Nonetheless, there were noticeable differences in the calculated transition states. The saddle points calculated by the HBB2 potential are shown in Figure 6.3 and their energies according to the three of the potentials are given in Table 6.1.

The energies and symmetries of the stationary points calculated by HBB2 are, by nature of the way the surface was defined, very close to those of accurate *ab initio* calculations, whereas TTM3-F has the wrong topology and an unrealistic local minimum along the $1 \rightarrow 5$ pathway. CC-pol-8s is the only other potential which correctly identifies the symmetry of the lowest saddle point as C_1. However, as it is defined only for rigid water molecules, it may not be an appropriate choice of PES for a study of tunnelling splittings. The optimization algorithm can easily be extended to locate instantons on these surfaces, but the fluctuation matrix becomes difficult to define except in Cartesian coordinates. The VRT(MCY-5f) potential describes most of the surface correctly, but has an incorrect plane of symmetry in the transition state along the $1 \rightarrow 4$ pathway. As well as incorrectly including a plane of symmetry in the (34) transition state, no transition state for the $1 \rightarrow 7$ permutation was located at all on either the q-TIP4P/F or RWK surfaces. There is no transition state for the (12) permutation according to any of the potentials. The minimum-energy pathway for this rearrangement, calculated using the nudged-elastic-band method, goes instead via the $\nu = 5$ well using the permutation (AB)(1324) twice followed by (34).

Nonetheless, the instanton approach does not necessarily fail if a transition state is non-existent or wrongly assigned, because a minimum-action pathway between two wells can exist even without a transition state. In this work, we concentrate on the three potentials included in Table 6.1: HBB2, probably the most accurate surface currently available; TTM3-F which is a commonly-used cheaper potential and will provide a strong test of the method as it has incorrect topology; and VRT(MCY-5f), because we shall be able to compare our instanton results with more accurate methods previously used on this system (Keutsch et al., 2003*b*). Despite differences in topology, all five instantons were successfully located on each of the three surfaces.

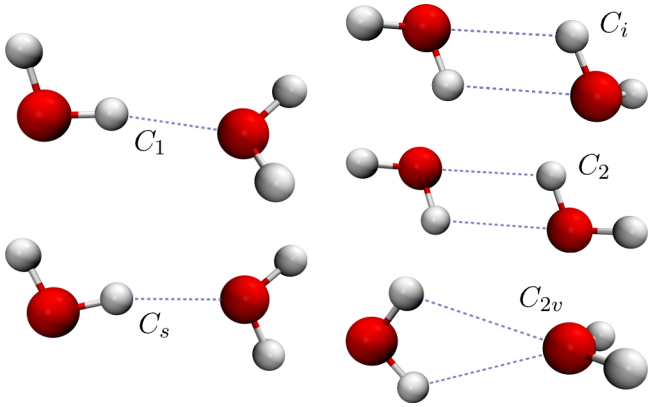

Figure 6.3 – Key saddle-point geometries on the HBB2 potential energy surface for the water dimer labelled by their point-group symmetry. Note that the C_s saddle point is second order, whereas the others are first order.

Table 6.1 – Saddle points of the water dimer calculated for three different potential energy surfaces. The pathways linked by the first-order saddle points are indicated along with the permutation which is described with respect to the labels in Figure 6.2. The point group of the saddle point is given along with the calculated barrier height $V^{\ddagger}$ (in kJ/mol).

		HBB2		TTM3-F		VRT(MCY-5f)	
Permutation	$1 \to \nu$	Sym.	$V^{\ddagger}$	Sym.	$V^{\ddagger}$	Sym.	$V^{\ddagger}$
(34)	4	C_1	2.2	C_s	0.9	C_s	1.7
...	...	C_s	2.5[a]	...	...	...	...
...	...	...	...	C_i	0.9[b]	...	...
(AB)(1324)	5	C_i	3.1	C_1	1.7	C_i	1.8
(AB)(14)(23)	7	C_2	4.2	C_1	2.5	C_2	3.0
(12)(34)	2	C_{2v}	7.5	C_{2v}	10.4	C_{2v}	7.0
(12)	3	...	...	...	...	...	...

[a] Second-order saddle point
[b] Minimum

6.2.2 Details of the calculation

It was straightforward to find the five kinks using the techniques of Chapter 5, whereby the linear polymer is allowed to move freely, i.e. the ends are not fixed to the wells. The initial position of the polymer was taken to be the minimum-energy path between the wells, computed by steepest descent from the transition state. However, in the case of the $1 \rightarrow 3$ path, for which no transition state exists, the polymer was placed with half of its beads in each of the wells and a fixed-ended linear-polymer minimization (cf. Eq. 5.18) was run first before the geometry relaxed using the loose-ended version (Eq. 5.40). The optimization had no problems in locating the kink even in this difficult case.

All minimizations were carried out using the slightly modified L-BFGS algorithm (Nocedal, 1980; Liu and Nocedal, 1989) in OPTIM (Wales), for which the line search has been removed. This approach has the advantage that the Hessian matrix need only be calculated and diagonalized once per kink, that is, in order to determine the ratio of eigenvalues Φ, and it can be done efficiently because the matrix is banded. One can parallelize the optimization quite simply by computing the potential and gradient of each bead on separate CPUs. However, for large systems with a large number of beads, the eigenvalue calculation can become the slowest part of the algorithm, and this is not so easy to parallelize.

We started the searches for the kinks with a small number of beads at relatively high temperatures (typically $M = 32$ and $\beta = 10\,000$ a.u.), and then increased β and M until a table of the weights $\theta_{\lambda\mu}$ versus M and β was numerically converged along the diagonal (see Table 5.1); β was increased in steps of 5000 a.u. and M by factors of 2, starting from $M = 32$ and finishing with $M = 4096$. When increasing M, the search was started from the geometry obtained by interpolating M beads along the minimum geometry kink found in the previous $M/2$ run as explained in §5.4. A very small amount skeletal rearrangement was necessary to ensure that the cluster did not gain linear or angular momentum, which may explain why is was necessary to use such large values of M for convergence. However, as the action tends to converge faster than the determinant, one could obtain a very similar result with far fewer beads, the error being less than that already implicitly present in the method.

Symmetry labels were assigned to the energy levels by inspecting the

components of the eigenvectors of the tunnelling matrix **W** and comparing them with the permutation-inversion group table (Dyke, 1977). For example the *atomic* permutation $\mathcal{P} = (12)$ effectively permutes the *wells* $1, 2, 3, 4, 5, 6, 7, 8 \rightarrow 3, 4, 1, 2, 8, 7, 6, 5$. To find the symmetry of the energy level E_ν corresponding to the eigenvector $\mathbf{v}$, where $\mathbf{W}\mathbf{v} = E_\nu \mathbf{v}$, we computed $\langle \mathbf{v} | \mathcal{P}\mathbf{v} \rangle$ for each permutation $\mathcal{P}$, and compared the results with the characters from the group table.

6.2.3 Instanton tunnelling paths and the adjacency matrix

We located a kink connecting well 1 to each of the wells 2, 3, 4, 5 and 7, following the procedure described above. Some properties of the kinks, including the computed values of $h_{1\nu}$ (Eq. 6.4) are given in Tables 6.2 and 6.3 and the five kinks calculated here can be visualized as movies, which can be downloaded from the supplementary material to Richardson et al. (2011).

The $1 \rightarrow 4$ path is referred to as *acceptor tunnelling* and corresponds to an exchange of the hydrogen atoms 3 and 4 (in the notation of Figure 6.2). Previous work (Wales, 1999) found that this motion does not correspond to a simple internal rotation of the acceptor water molecule but rather to a concerted twist of the donor monomer and wag of the acceptor. The computed $1 \rightarrow 4$ kink is entirely consistent with this type of motion. The kink differs, however, from the minimum-energy path used in the WKB calculations of Watanabe et al. (2004) in that it passes through a point with a plane of symmetry close to the second-order C_s saddle point instead of going through the first-order C_1 saddle point (see Figure 6.3). This occurs because the action is smaller for the kink pathway which, although it passes through regions of higher potential energy, is shorter than the minimum-energy path, just as in the case of malonaldehyde. One effect of this difference which must be considered is that there are two symmetrically-equivalent kinks between wells 1 and 4, but four symmetrically-equivalent minimum-energy paths. As a result, the instanton calculations find that $A_{14} = 2$, whereas Taketsugu and Wales (2002) and Watanabe et al. (2004) use $A_{14} = 4$, which is the appropriate number for their calculation. The same situation was found using the CC-pol-8s potential.

The instanton predictions for the $1 \rightarrow 5$ and $1 \rightarrow 2$ tunnelling paths agree with previous work (Taketsugu and Wales, 2002), both in terms of the adjacency matrix ($A_{15} = A_{12} = 1$), and in terms of the tunnelling dynamics

Table 6.2 – Instanton tunnelling pathways (kinks) located on the HBB2 potential surface for $(H_2O)_2$. The pathways are numbered by the well ν in which the kink ends. The actions S_{kink}, eigenvalue ratios Φ and tunnelling matrix elements $h_{1\nu}$ were calculated from the kinks as described in the text.

				$-h_{1\nu}/\mathrm{cm}^{-1}$	
Pathway	$1 \rightarrow \nu$	$S_{\mathrm{kink}}/\hbar$	Φ/a.u.	inst.	expt.[a]
Acceptor tunnelling	4	5.74	120	5.5	2.3
Geared interchange	5	7.48	720	0.19	0.18
Anti-geared interchange	7	11.17	140	0.029	0.01
Bifurcation tunnelling	2	12.04	51	0.035	0.02
Donor exchange	3	15.94	18	0.0023	...

[a] Zwart et al. (1991)

Table 6.3 – Same as Table 6.2 for $(D_2O)_2$.

				$-h_{1\nu}/\mathrm{cm}^{-1}$	
Pathway	$1 \rightarrow \nu$	$S_{\mathrm{kink}}/\hbar$	Φ/a.u.	inst.	expt.[a]
Acceptor tunnelling	4	7.75	170	6.0(−1)	4.5(−1)
Geared interchange	5	10.44	900	9(−3)	9.4(−3)
Anti-geared interch.	7	15.54	170	4(−4)	3.7(−4)
Bifurcation tunnelling	2	16.82	67	2.7(−4)	2.3(−4)
Donor exchange	3	22.22	24	4(−6)	...

[a] Suenram et al. (1989); Karyakin et al. (1993); Paul et al. (1998)

along the paths. The most important of these paths is the $1 \rightarrow 5$ path, which corresponds to a *geared interchange* of the acceptor and donor monomers. The *anti-geared interchange* ($1 \rightarrow 7$) behaves similarly, but also performs an extra hydrogen permutation during the pathway and has $A_{17} = 1$. Its existence has been predicted from experimental measurements (Fraser et al., 1989), but is frequently neglected in theoretical studies because although its inclusion shifts the energy levels, it does not cause an extra splitting. The $1 \rightarrow 2$ pathway is called either *donor* or *bifurcation tunnelling* and exchanges the hydrogen atoms on the donor molecule accompanied by a wag of the acceptor. Unlike the minimum-energy paths that were obtained in previous work, the instanton paths for $1 \rightarrow 5$, $1 \rightarrow 7$ and $1 \rightarrow 2$ do not pass directly through the various saddles identified in Figure 6.3, but do pass close to them through points of C_i, C_2 and C_{2v} symmetry respectively.

The remaining $1 \rightarrow 3$ path has been little studied in the literature, and is thought to contribute only a small amount to the tunnelling pattern (Coudert and Hougen, 1988). No transition state leading to wells 1 and 3 exists and so the corresponding minimum-energy path does not connect the wells directly. Nevertheless a minimum-action path does exist and we were able to find an instanton kink describing this tunnelling pathway, which we call *donor exchange*. Unlike the other four paths, the $1 \rightarrow 3$ kink does not pass through a point with any symmetry, and for this reason (and also because the donor could rotate either clockwise or anticlockwise) there are other degenerate pathways such that $A_{13} = 4$.

All five kinks were located on each of the three potentials studied, and despite difference in the surface topologies, the instantons all followed similar pathways passing through points of the same symmetry. We can therefore conclude that the ring-polymer instanton method can be less sensitive to minor defects in the PES than methods based on steepest-descent pathways, but remains of course sensitive to major defects such as barrier height and shape, as it must be or it would not be able to make good estimates of the splitting pattern.

When arranged from largest to smallest, the tunnelling matrix elements retain the same order as was found by the WKB analysis. This is because the action of a pathway is still loosely connected to the height of the barrier, and the pathways did not deviate too strongly from the minimum-energy pathways. The instanton method will not therefore predict a qualitatively

different splitting pattern for the water dimer from those obtained by previous studies. However, this will not necessarily be true for other systems (see §6.3).

6.2.4 Tunnelling matrix elements and splitting pattern

The adjacency matrix obtained from the kinks gives rise to the following tunnelling matrix:

$$\mathbf{W} = \begin{pmatrix} 0 & h_{12} & 4h_{13} & 2h_{14} & h_{15} & h_{15} & h_{17} & h_{17} \\ h_{12} & 0 & 2h_{14} & 4h_{13} & h_{15} & h_{15} & h_{17} & h_{17} \\ 4h_{13} & 2h_{14} & 0 & h_{12} & h_{17} & h_{17} & h_{15} & h_{15} \\ 2h_{14} & 4h_{13} & h_{12} & 0 & h_{17} & h_{17} & h_{15} & h_{15} \\ h_{15} & h_{15} & h_{17} & h_{17} & 0 & h_{12} & 4h_{13} & 2h_{14} \\ h_{15} & h_{15} & h_{17} & h_{17} & h_{12} & 0 & 2h_{14} & 4h_{13} \\ h_{17} & h_{17} & h_{15} & h_{15} & 4h_{13} & 2h_{14} & 0 & h_{12} \\ h_{17} & h_{17} & h_{15} & h_{15} & 2h_{14} & 4h_{13} & h_{12} & 0 \end{pmatrix}. \qquad (6.12)$$

This matrix has exactly the same form as a tunnelling matrix first derived by Coudert and Hougen (1988) on the basis of an analysis of the minimum-energy paths, and which has been widely used for describing tunnelling in water dimer.* Their calculated minimum-energy paths actually gave rise to the same adjacency matrix as the instanton kinks because they also pass through the C_s saddle point, which was thought at the time to be first order. We emphasize that no reference was made to the Coudert and Hougen model when constructing $\mathbf{W}$, which was done entirely using the symmetry and connectivity of the wells and kinks.

The values of the elements $h_{1\nu}$, computed from the actions S_{kink} and eigenvalue ratios Φ of the kinks located on the HBB2 surface were given in Tables 6.2 and 6.3. These elements span four orders of magnitude, and it is clear from comparison with the experimental data that the instanton calculation has correctly predicted each of these magnitudes. Since the form of the tunnelling matrix $\mathbf{W}$ is correct, it follows that instanton calculations are likely to predict the correct splitting pattern (obtained by diagonalizing $\mathbf{W}$) which is shown in Figure 6.4. Tables 6.4 and 6.5 show that the instanton splitting patterns agree well with experiment, especially for the best potential

*Note that Coudert and Hougen (1988) employ the notation $h_{\nu v}$ in place of $h_{1\nu}$.

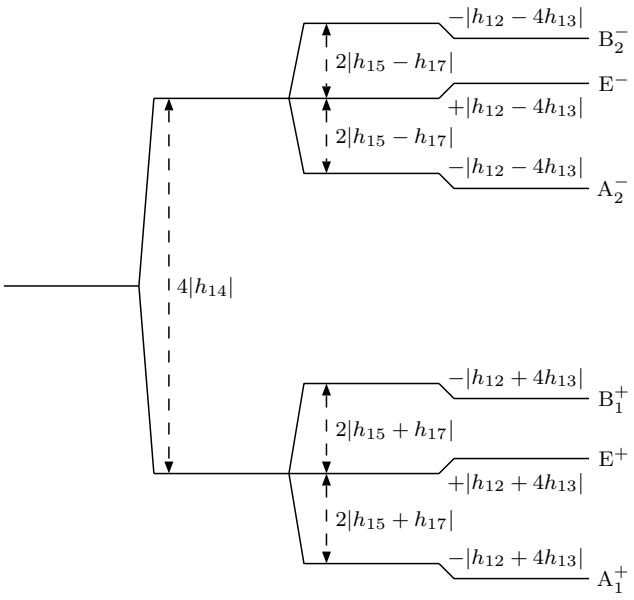

Figure 6.4 – Water dimer tunnelling-splitting pattern, obtained by diagonalizing the instanton tunnelling matrix **W** of Eq. 6.12. The values of the tunnelling elements $h_{1\nu}$ and of the splittings are given in Tables 6.2–6.5.

surface HBB2.

6.2.5 Quantitative comparison with quantum results and experiment

We do not expect the ring-polymer instanton method to give quantitative agreement with experiment because, as mentioned above, the method neglects anharmonicity perpendicular to the tunnelling path and assumes that the splittings depend only weakly on the rotational quantum numbers. Nevertheless, the agreement of the HBB2 instanton results with experiment and with the quantum results of Huang et al. (2008) is within a factor of two for $(H_2O)_2$, and even closer for $(D_2O)_2$, although the excellent agreement of the latter may be partly caused by a fortuitous cancellation of errors.

Two pieces of evidence suggest that most of the quantitative errors in the HBB2 instanton splittings result from the neglect of anharmonicity. First, the errors are a lot smaller for $(D_2O)_2$ than for $(H_2O)_2$, which is consistent with the expectation that deuteration reduces the fluctuations of the polymers around the wells. Second, the interchange splittings (those dependent mostly

Table 6.4 – Tunnelling splittings (in cm^{-1}) for $(H_2O)_2$ obtained from the instanton calculations on three different potential surfaces, compared with quantum results and with experiment. See Figure 6.4 for a diagram of the overall splitting pattern.

		HBB2		TTM3-F	VRT(MCY-5f)		
	Splitting	inst.	quantum[a]	inst.	inst.	quantum[b]	expt.[c]
Acceptor splitting	$4\|h_{14v}\|$	22	13	42	50	11.725	9.4
Interchange (lower)	$4\|h_{15}+h_{17}\|$	0.86	0.75	0.73	0.61	0.602	0.75
Interchange (upper)	$4\|h_{15}-h_{17}\|$	0.63	0.65	0.45	0.38	0.609	0.65
Bifurcation (lower)	$\|h_{12}+4h_{13}\|$	0.044	...	0.015	0.17	0.116	0.02
Bifurcation (upper)	$\|h_{12}-4h_{13}\|$	0.026	...	0.00041	0.12	−0.004	0.02

[a] Huang et al. (2008)
[b] Keutsch et al. (2003*b*)
[c] Zwart et al. (1991)

Table 6.5 – Same as Table 6.4 for $(D_2O)_2$.

		HBB2		TTM3-F	VRT(MCY-5f)		
	Splitting	inst.	quantum[a]	inst.	inst.	quantum[b]	expt.[c]
Acceptor splitting	$4\|h_{14}\|$	2.4	2.4	10.6	7.1	2.14	1.8
Interchange (lower)	$4\|h_{15}+h_{17}\|$	0.037	0.040	0.039	0.054	0.52	0.039
Interchange (upper)	$4\|h_{15}-h_{17}\|$	0.035	0.036	0.034	0.048	0.51	0.036
Bifurcation (lower)	$\|h_{12}+4h_{13}\|$	2.8(−4)	...	6(−5)	1.4(−3)	...	2.3(−4)
Bifurcation (upper)	$\|h_{12}-4h_{13}\|$	2.5(−4)	...	3(−5)	1.3(−3)	...	2.2(−4)

[a] Huang et al. (2008)
[b] Leforestier et al. (2002)
[c] Suenram et al. (1989); Karyakin et al. (1993); Paul et al. (1998)

on h_{15}) agree much better with experiment than the acceptor splittings do. This is because the barrier height (210 cm^{-1}) along the acceptor-tunnelling path is close to the change in harmonic zero-point energy (204 cm^{-1}), and the calculations on the model double-well system (see Table 5.4) showed that there are large errors for similarly low barriers. This effect is almost certainly why the instanton acceptor splitting is a factor of two too large in $(H_2O)_2$. This error is of course much smaller in $(D_2O)_2$, as deuteration decreases the fluctuations.

The instanton prediction for the acceptor splitting of $(D_2O)_2$ agrees to within 2% of the quantum result for the HBB2 potential. Whilst this extremely good agreement is probably fortuitous, it is not unreasonable that these two results should be close. In the quantum calculations, the OH bond-lengths were held fixed at their monomer equilibrium geometries, and this constraint (rather than deficiencies in the potential surface) is thought to explain the deviation from experiment (Huang et al., 2008). The instanton calculations allow the system to relax, such that the OH distances vary correctly along the instanton path. However, Huang et al. (2008) argue that the main error produced by fixing the OH bonds (in the quantum calculation) is neglect of zero-point energy along the tunnelling path. Effectively, the instanton calculations are also neglecting a large proportion of this zero-point energy difference, through their neglect of anharmonicity. Hence both calculations make a similar approximation, and it is not surprising that the results are very close.

The values of $h_{1\nu}$ are known to depend only weakly on rotational quantum numbers, except for h_{14} (Coudert and Hougen, 1988; Huang et al., 2008). The $1 \rightarrow 4$ pathway involves an effective internal twist of the two monomers, which causes h_{14} to depend strongly on the rotational quantum number K. In Tables 6.2 and 6.3, we have quoted the $K = 0$ experimental values for h_{14}. The instanton results may therefore include errors resulting from "contamination" from $K \neq 0$. We shall not attempt to analyse these errors here, which, from the discussion above, would seem to be minor in comparison with the errors caused by the neglect of anharmonicity.

Results from the other two potentials are not quite so promising, although they do still produce the correct qualitative splitting pattern. For the same reason as explained above, the acceptor splittings are overestimated, but the remaining errors are consequences of problems with the potential surfaces.

The VRT(MCY-5f) potential was fitted to give the correct values of the acceptor and interchange splittings calculated by a pseudo-spectral split Hamiltonian method (Leforestier et al., 2002). However, the bifurcation splittings are an order-of-magnitude out, showing that the PES does not correctly describe the true water dimer. The TTM3-F potential also performs surprisingly well seeing as it was designed to reproduce the thermodynamics of large clusters and of liquid water. For this potential, the interchange splittings are closer to the experimental results than the bifurcation splittings, presumably because the surface is more accurate at lower energies.

Spurred on by the good agreement with experimental and fully-quantum theoretical results, we can use the same techniques to apply the ring-polymer instanton method to systems for which the spectra is not so well understood experimentally and which are too large for the application of accurate quantum calculations.

6.3 Application to water trimer

The next system to which we apply the ring-polymer instanton method is $(H_2O)_3$ and its deuterated form $(D_2O)_3$. The splitting pattern of the water trimer has been measured both experimentally (Pugliano and Saykally, 1992; Liu et al., 1994) and in theoretical studies using DMC (Gregory and Clary, 1995*a*) and WKB (Takahashi et al., 2005). A good review can be found in Keutsch et al. (2003*a*). It is not possible to apply exact DVR-type approaches to systems with this many degrees of freedom, even if rigid monomers were used, as the size of the basis set needed would be too large.

These theoretical approaches were not however able to explain the existence of "anomalous" quartets in the spectrum, which we show is a consequence of a number of competing bifurcation pathways. In the DMC study, the nodal planes were defined such that there was no differentiation between the six possible excited states corresponding to the different bifurcation rearrangements. In this way, the information necessary for explaining the appearance of the spectrum was lost. In the WKB study, depending on the potential energy surface used, different minimum-energy rearrangement pathways were found such that two types of splitting pattern were suggested (Walsh and Wales, 1996), neither of which agreed completely with experiment. The method gives no way of calculating which of the many mixed patterns

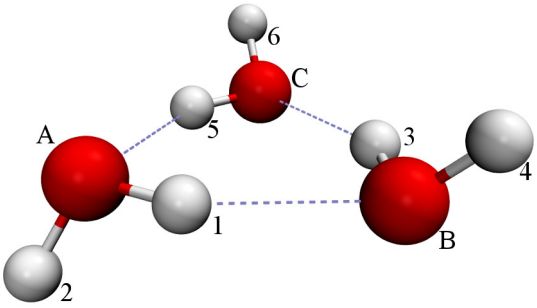

Figure 6.5 – The minimum-energy geometry of the water trimer.

suggested was correct (Keutsch et al., 2002). Seeing as the instanton method does not rely on predefined nodal planes or on the minimum-energy pathways between two isomers, it is able to resolve some of these problems as is shown below.

The stationary points of the water trimer were located using *ab initio* potentials by Fowler and Schaefer (1995). The equilibrium geometry is found to be a cyclic arrangement with C_1 symmetry where each monomer acts as a single hydrogen-bond donor and single acceptor as shown in Figure 6.5. The dangling hydrogen atoms on two of the monomers point up (u) relative to the plane: these are called the *majority* monomers, and are referred to individually as the *acceptor* and the *donor*, depending on their relation to the remaining *minority* monomer, in which the loose hydrogen points down (d).

There are 96 permutation-inversion isomers for the water trimer equilibrium geometry if covalent bonds are conserved (Wales, 1993*a*). The permutations include combinations of flipping a majority u to d and *vice versa*, exchanging the two hydrogen atoms in one monomer and changing the direction of the cyclic formation of hydrogen bonds. There are also higher-energy crown-shaped wells with uuu or ddd geometries (Fowler and Schaefer, 1995), but these have only a minor effect on the tunnelling-splitting pattern (Takahashi et al., 2005), which is dominated by tunnelling between the degenerate uud wells (and the equivalent ddu, udu, etc. wells).

6.3.1 Locating the kinks

Instantons were located using three different potential energy surfaces, two based on HBB2 combined with three-body terms, and a third, TTM3-F

(Fanourgakis and Xantheas, 2008). Of the former type, one will be called "PES(1,2,3)" (Wang et al., 2009; Wang and Bowman, 2010) and the other, which is less accurate but computationally less expensive, uses an efficient three-body fit based on an approximate form derived by Kumar and Skinner (2008), and is called "PES(1,2,KS/WB)". In both cases, the potentials were fitted to about 30 000 *ab initio* electronic energies.

The permutation-inversion isomers transform into one another under operations of the G_{96} molecular symmetry group. We ran preliminary calculations using a fixed-ended optimization on the best surface available, PES(1,2,3), to obtain a preliminary estimate of the relative importance of the 95 possible kinks connecting one well with each of the others. This was performed with 32 beads at a temperature of $\beta = 15\,000$ a.u., and the end-points were chosen such that the oxygen atoms remained stationary. We found that many of the kinks were unimportant to the tunnelling-splitting pattern, as expected, because they had large actions owing to the breaking of many hydrogen bonds, and therefore would give matrix elements which were too small to affect the splitting pattern significantly. However, we identified a total of seven kinks per well which could feasibly make a significant contribution. These kinks were then located precisely using the flexible-ended potential, following very similar procedures to those described in §6.2.2. Convergence was reached for each of the pathways with $M = 512$ and $\beta = 20\,000$ a.u., and all but one was found to contribute to the tunnelling-splitting pattern.

6.3.2 Properties of the instanton tunnelling paths

Various properties of the calculated kinks are summarized in Table 6.6, using the notation of Walsh and Wales (1996). Conflated series of snapshots, showing the motion along each of the these kinks, are shown in Figure 6.6 and movies of the kinks can be downloaded from the supplementary material to Richardson et al. (2011). The tunnelling paths described by the kinks replicate qualitatively the major tunnelling pathways as those previously identified in WKB calculations (Walsh and Wales, 1996; Takahashi et al., 2005), from where we borrow the notation. However, we emphasize that no prior assumptions were made about the nature of the kinks, which were found by minimizing the linear-polymer potential energy surface as described above. The resulting tunnelling matrix elements for $(H_2O)_3$ and $(D_2O)_3$ are

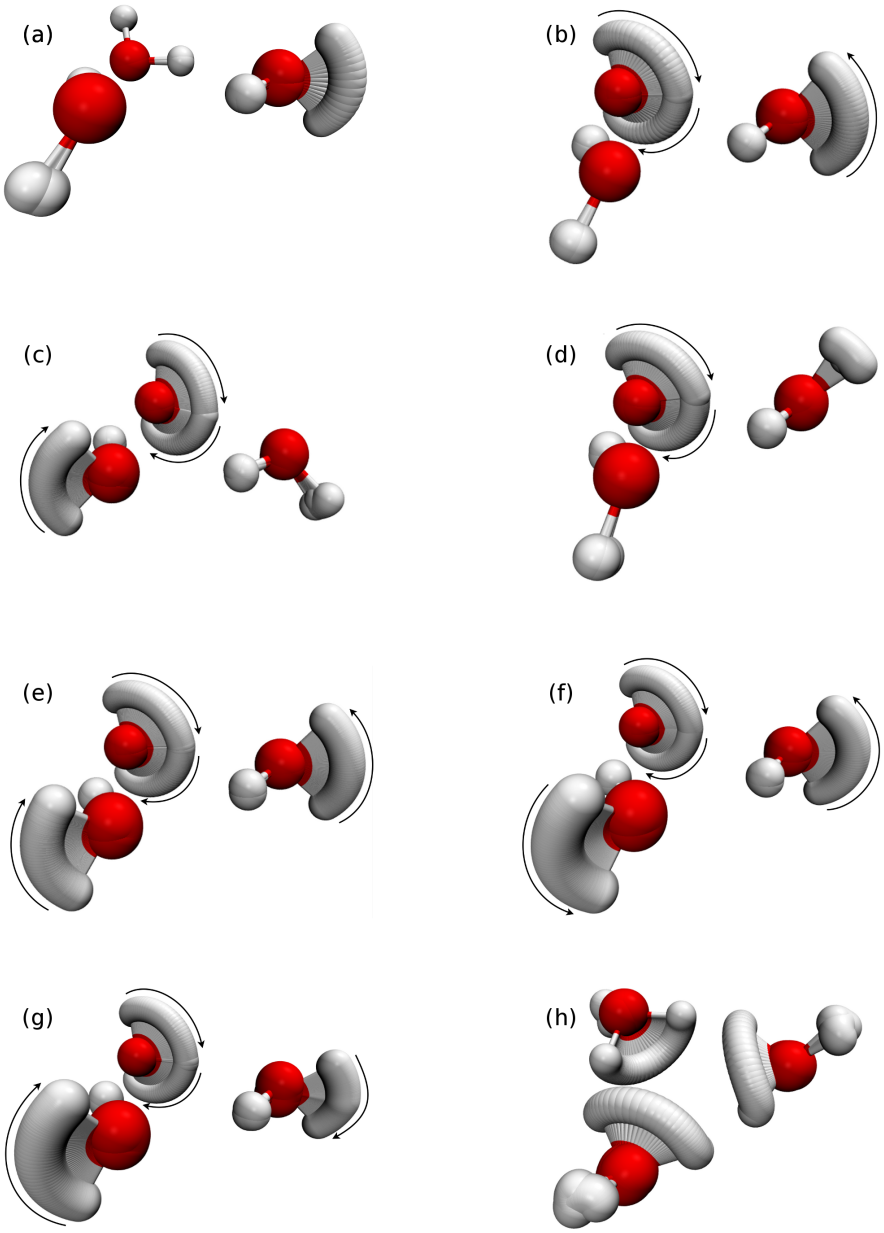

Figure 6.6 – Conflated snapshots of instanton tunnelling paths (kinks) obtained using the PES(1,2,3) surface for $(H_2O)_3$. The paths shown are (a) the flip, (b)–(g) the A1, A2, A3, B1, B2 and B3 bifurcations, and (h) the cwccw path. The arrows show the direction of motion of the hydrogen atoms. Note that the B2 path (f) does not contribute to the tunnelling because it is a saddle point on the linear-polymer surface (see text).

Table 6.6 – Instanton tunnelling pathways (kinks) located on the PES(1,2,3) potential surface for $(H_2O)_3$. Properties of the kinks are summarized in the first column, using the notation of Walsh and Wales (1996) for the bifurcations (min=minority monomer, don=donor monomer, acc=acceptor monomer, with the slash separating the forward and reverse paths where these differ). The actions S_{kink} and eigenvalue ratios Φ were calculated from the kinks as described in the text.

Pathway	Shorthand	$S_{\text{kink}}/\hbar$	Φ/a.u.
Flip	flip	2.35	300
Min + acc flip/don + min flip	A1	13.44	100
Min + don flip/acc + min flip	A2	14.85	11
Don + no flips/acc + no flips	A3	12.92	130
Min + double flip	B1	14.99	9
[Don + double flip	B2	16.13	...]
Acc + double flip	B3	16.57	2
Clockwise-counterclockwise	cwccw	42.93	3

given in Table 6.7, and the splitting patterns, obtained by diagonalization of **W**, in Table 6.8 and Figures 6.7 and 6.8.

The flip pseudo-rotation

Figures 6.7 and 6.8 show that the instanton splitting pattern has an overall quartet structure. This result agrees with previous experimental and theoretical studies of the trimer, in which this pattern has been shown to result from the flipping of one of the dangling hydrogen atoms. When this operation is performed six times in succession, two of the principal moments of inertia complete a full 360° rotation. For this reason the flipping process is dubbed a pseudo-rotation (Liu et al., 1994) and assigned pseudo-rotational quantum numbers $k = 0, \pm 1, \pm 2, 3$. The kink that was calculated for this pathway is shown in Figure 6.6a.

Since the (harmonic) zero-point energy in the wells is slightly greater (by 27 cm^{-1}) than the barrier height, the flip is not a tunnelling processes. Nevertheless, the instanton splitting agrees with experiment to within a factor of 2.3 for $(H_2O)_3$ and 1.8 for $(D_2O)_3$. This relatively good agreement should come as no surprise, since Eq. 6.1 is clearly still applicable to the flipping motion, provided one can define a $Q_0(\beta)$ from which paths that flip onto or over the barrier are excluded. The ability of the instanton approach to describe the flip is thus very similar to its ability to describe the acceptor

Table 6.7 – Instanton tunnelling elements $-h_{\lambda\mu}$ in cm^{-1}, calculated for $(H_2O)_3$ and $(D_2O)_3$ using three different potential energy surfaces.

	$(H_2O)_3$			$(D_2O)_3$
Pathway	PES(1,2,3)	PES(1,2,KS/WB)	TTM3-F	PES(1,2,3)
flip	50	60	47	18
A1	0.005	0.007	0.0019	2.0(−5)
A2	0.011	0.02	0.0024	3.1(−5)
A3	0.006	0.007	0.0010	3.5(−5)
B1	0.011	0.02	0.0053	3.0(−5)
B3	0.009	0.02	0.0055	1.7(−5)
cwccw	5(−14)	2(−13)	1.1(−13)	5.6(−21)

Table 6.8 – Calculated tunnelling-splitting pattern in cm^{-1} for both isotopomers of the water trimer using PES(1,2,3).

$(H_2O)_2$		$(D_2O)_2$	
Energy level	Irrep	Energy level	Irrep
100.0000	T_1^-	36.000015	A_1^-
100.0000	T_2^-	36.000005	T_1^-
100.0000	A_1^-	35.999995	T_2^-
100.0000	A_2^-	35.999985	A_2^-
50.0129	T_1^+	18.000048	T_1^+
50.0116	T_2^+	18.000039	E_2^+
50.0020	E_2^+	18.000022	T_2^+
49.9980	E_1^+	17.999978	T_1^+
49.9884	T_1^+	17.999961	E_1^+
49.9871	T_2^+	17.999952	T_2^+
−49.9669	T_1^-	−17.999884	T_1^-
−49.9700	E_2^-	−17.999926	T_2^-
−49.9869	T_2^-	−17.999937	E_2^-
−50.0131	T_1^-	−18.000063	E_1^-
−50.0300	E_1^-	−18.000074	T_1^-
−50.0331	T_2^-	−18.000116	T_2^-
−99.9360	A_2^+	−35.999781	A_2^+
−99.9787	T_2^+	−35.999927	T_2^+
−100.0213	T_1^+	−36.000073	T_1^+
−100.0640	A_1^+	−36.000219	A_1^+

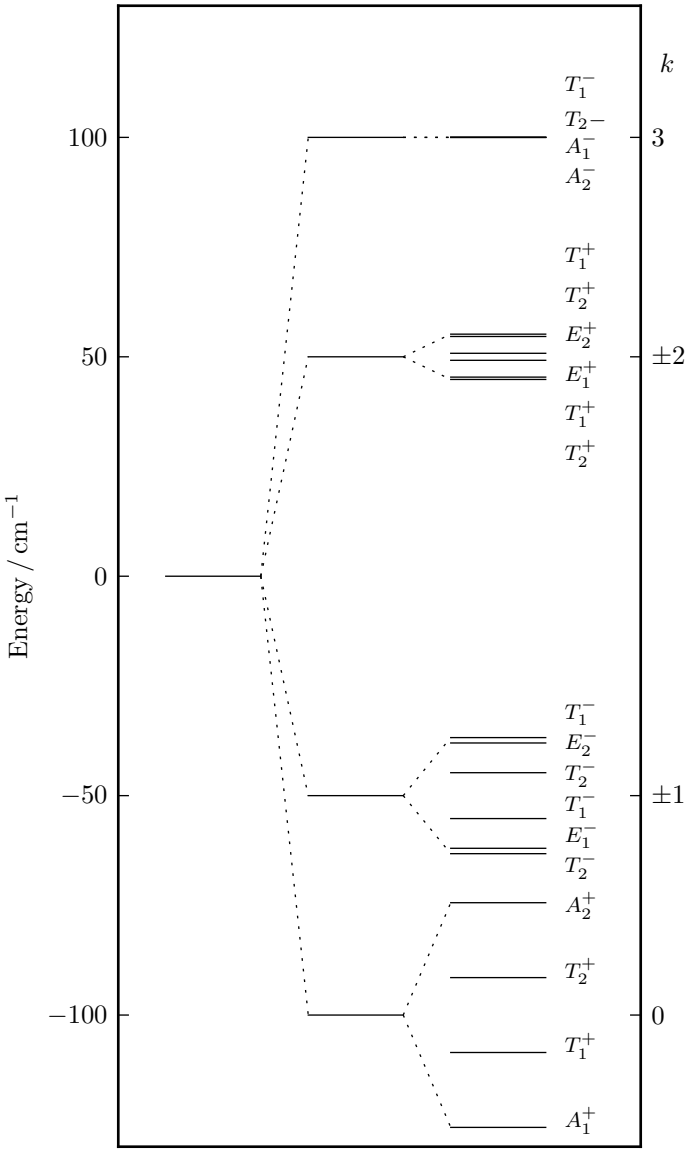

Figure 6.7 – Tunnelling-splitting pattern for $(H_2O)_3$, obtained by diagonalizing the instanton tunnelling matrix **W** of Eq. 6.3. The first set of lines is unscaled, and only the overall quartet splitting produced by the flip is visible. Magnification by a factor of 400 produces the second set of lines, which show the bifurcation splitting pattern. The values of the tunnelling elements $h_{1\nu}$ are given in Table 6.7. There is an accidental degeneracy for the $k = 3$ levels which disappears within the numerical errors of the calculation. The energy levels used to plot this figure are tabulated in Table 6.8.

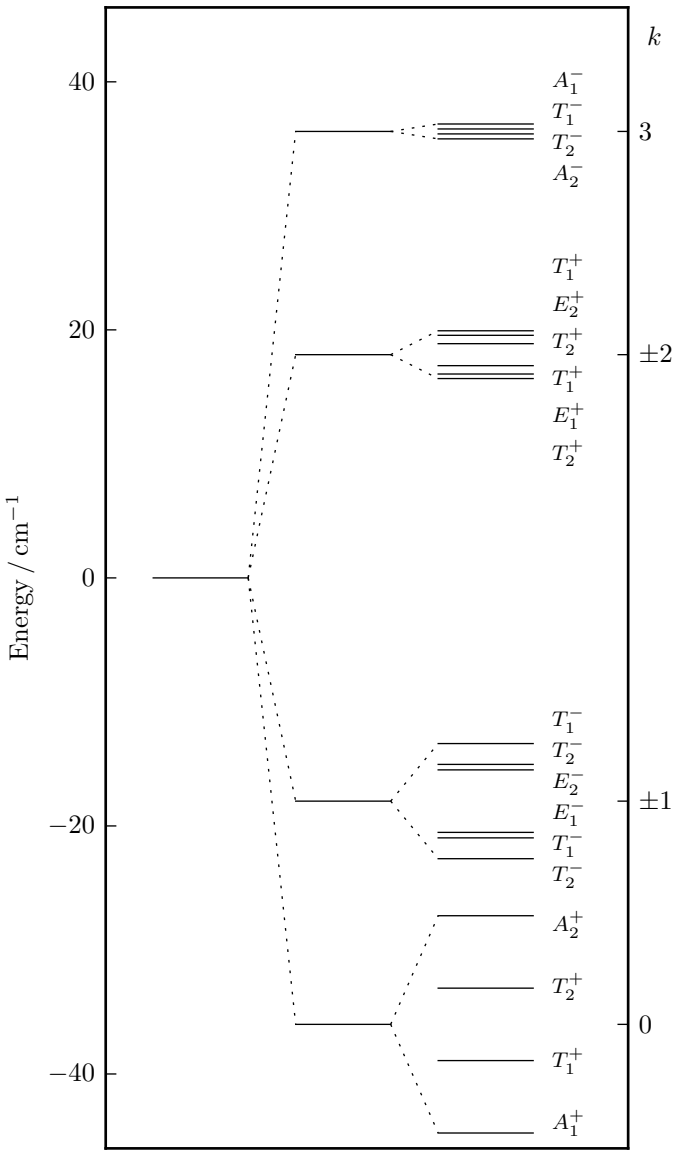

Figure 6.8 – Same as Figure 6.7 for $(D_2O)_3$. The second set of lines showing the bifurcation splittings have been magnified by a factor of 40 000.

tunnelling in water dimer (see §6.2.5), for which the zero-point energy of the wells is only slightly below the barrier. In fact, there is no clear distinction between these two types of process and they will both contain significant errors arising from the neglect of anharmonicity, because paths that have both ends fixed in one well can describe fluctuations onto or over the barrier. The relatively good agreement of the flip with experiment indicates that only a small proportion of the paths in $Q_0(\beta)$ manage to reach or cross the barrier. There would be a larger proportion of such paths if the flip were even more facile, which would lead to a breakdown of the instanton approximation.

Pathways also exist which describe double flips where two dangling hydrogen atoms flip at the same time. However, it was found that the actions were, as expected, about equal to twice that of the single-flip kink and would not therefore make a significant effect to the overall splitting pattern.

Bifurcation tunnelling

The more detailed structure in the instanton splitting patterns (Figures 6.7 and 6.8) is produced by the kinks labelled A1, A2, A3, B1 and B3 (see Figure 6.6 and Table 6.6). Each of these kinks gives the same qualitative description of the tunnelling as one of the paths identified in previous WKB calculations (Walsh and Wales, 1996; Takahashi et al., 2005), from where we have taken the notation.

These paths describe *bifurcation tunnelling* (previously known as *donor tunnelling*), meaning that the dangling hydrogen on one of the monomers swaps roles with the bonding hydrogen, such that the geometry of the cluster passes through a bifurcated structure rather than performing a C2 rotation (Wales, 1993*a*). There are six possible bifurcation rearrangements unrelated by symmetry which differ in the choice of bifurcated monomer and also the number of accompanying flips (see Figure 6.6 and Table 6.6). Three of these pathways are self-reversible, i.e. the monomers have the same roles within the cluster at the start and finish of the path, and are given the label B (as opposed to A for the others).

The contributions of the various bifurcation kinks to the splitting pattern are difficult to disentangle. Tables 6.6 and 6.7 show that the actions of these paths differ significantly, but that these differences are roughly compensated by changes in the values of the eigenvalue ratio Φ of Eq. 5.20. As a result, the five bifurcation paths make contributions to the splitting pattern of

roughly equal importance. This leads to a far more complex splitting pattern than would appear if tunnelling only occurred along one bifurcation pathway (Keutsch et al., 2002), and explains the appearance of the "anomalous" quartets with varying line-widths.

Previous studies (Walsh and Wales, 1996) identified an additional bifurcation path, denoted B2. There is in fact a stationary point corresponding to B2 on the linear-polymer surface (see Figure 6.6f and Table 6.6), but it is a first order saddle; linear polymers set to this geometry relax into combinations of the flip and the A1 path. As a result, semi-classical tunnelling between the wells connected by the B2 path proceeds via combinations of the flip and A1, *not* via B2. We therefore set the corresponding elements of $\mathbf{W}$ to zero. No changes needed to be made to incorporate the combined flip and A1 paths, since these are already included individually in $\mathbf{W}$, and the treatment of §6.1 ensures that all possible combinations of individual paths are included in $Q(\beta)$. We note that the other two potential energy surfaces tested also returned first-order saddles for B2, so we can be quite confident that the B2 path does not contribute significantly to the splitting pattern in water trimer.

Clockwise-counterclockwise tunnelling

No combination of the six instanton paths described above is able to convert a minimum-energy geometry of water trimer into the permutation-inversion isomer corresponding to reversal of the hydrogen-bonding pattern in the ring in Figure 6.5. The generator for this operation is (35)(46)(BC)*. As a result, the tunnelling can be described adequately using the G_{48} molecular symmetry group instead of G_{96} (Wales, 1993*a*), and the wells split into two sets, which are not coupled by $\mathbf{W}$. This finding is consistent with all recent studies of the water trimer (Keutsch et al., 2003*a*), in which tunnelling between these subsets is thought not to contribute to the splitting patterns.

Nevertheless, the possibility of a tunnelling path corresponding to this rearrangement in water trimer has been discussed in the literature (Pugliano and Saykally, 1992), and we applied the instanton method to locate the kink. The mechanism is a concerted breaking and reforming of all three of the hydrogen bonds in a motion described as *clockwise-counterclockwise* (cwccw) tunnelling. It was straightforward to locate the cwccw kink, which is shown in Figure 6.6h. As expected, the action of this kink is very large

(Table 6.6), and the tunnelling matrix element negligibly small (Table 6.7). For the purposes of calculating the tunnelling-splitting pattern, this pathway is considered unfeasible. Based on the preliminary tests (see §6.3.1), other pathways similar to this but accompanied by flips or even bifurcations will have similarly large actions and are also expected to have a negligible effect on the tunnelling-splitting pattern.

6.3.3 Construction of the tunnelling matrix

With six different feasible tunnelling pathways, the 48×48 tunnelling matrix $\mathbf{W}$ is quite a complicated object. However, it was not difficult to write a stand-alone algorithm which was able to construct the matrix using the values of $h_{\lambda\mu}$ from Table 6.6.

It was first necessary to label each of the 48 wells with a three letter word where each letter represents the state of one of the monomers and can take the following values: 'u' or 'd' depending on when the dangling hydrogen is up or down, or 'U' or 'D' if the monomer has bifurcated and the hydrogen atoms are swapped relative to the geometry shown in Figure 6.5. The words which include three ups or three downs were excluded and the remaining words labelled with a number from 1 to 48 and assigned to rows and columns of the matrix.

For each well λ, the following permutations were performed in turn: the flip of the majority acceptor and of the majority donor monomer, the bifurcations A1, A2 and A3, both forwards and backwards, and the B4 and B6 bifurcations. In each case, the index of the resulting well μ was determined, and the value of $h_{\lambda\mu}$ inserted into the position $W_{\lambda\mu}$. Because it was not found in any of the cases that more than one kink pathway connected a pair wells, all the adjacency matrix elements $A_{\lambda\mu}$ for these permutations were equal 1. This was repeated for the $(D_2O)_3$ results and these matrices diagonalized to retrieve the spectra given in Table 6.8 and Figures 6.7 and 6.8.

The symmetry labels were obtained by inspecting the symmetry of the eigenfunctions of $\mathbf{W}$, using the same procedure as for water dimer, although it was only necessary to consider the (12), (34), (56) and E^* permutations to collect enough information to be able to assign all the levels. The appropriate group table can be found in the study by Wales (1993*a*).

6.3.4 Comparison of splitting patterns with experiment

The instanton splitting patterns of Figures 6.7 and 6.8 are in good overall agreement with the results of experiment, (Pugliano and Saykally, 1992; Liu et al., 1994; Suzuki and Blake, 1994; Liu et al., 1996; Olthof et al., 1996; Viant et al., 1997; Keutsch et al., 2003*a*) in which far-infrared spectra for $(H_2O)_3$ and $(D_2O)_3$ and other isotopomers have been interpreted in terms of an overall quartet structure caused by the flip pseudo-rotation, each branch of which is further split by bifurcation tunnelling. The latter gives rise to quartets in the spectrum, which are either regular (equally spaced with equal line-widths) or "anomalous" (similar but inconstant spacing with varying line-widths) (Keutsch et al., 2002). The former are associated with the outer $k = 0, 3$ branches; the latter with the $k = \pm 1, \pm 2$ inner branches (for rotational quantum number $K = 0$).

Previous studies based on the WKB approximation, which define the tunnelling pathways to lie along minimum-energy paths (Takahashi et al., 2005), assumed that only one bifurcation pathway would contribute to the spectrum. If this were true, and the pathway was one of A1, A2 or A3, one would obtain a qualitatively different spectrum from that if it were one of B1, B2 or B3. By analysing the known experimental spectrum, it was shown that the A-type pattern was incorrect (Keutsch et al., 2002) because it leads to unevenly spaced $k = \pm 1, \pm 2$ quartets, whereas the experimental "anomalous" quartets are roughly evenly spaced. Although the B-type pattern does reproduce the evenly spaced quartets, it is not necessarily the only possible explanation. Our results in Figures 6.7 and 6.8, calculated from a combination of the five tunnelling pathways (of both A and B type), also show approximately evenly spaced patterns, provided one assumes that the inner sextets give rise to what appear to be quartets in the experimental spectrum. This case would also explain the varying line-widths of the "anomalous" quartets (Keutsch et al., 2002).

A more detailed comparison with experiment is difficult for the trimer, owing to complexities in the rovibrational spectrum caused by, amongst other things, a dependence of the $k = \pm 1, \pm 2$ bifurcation splitting pattern on Coriolis coupling (Keutsch et al., 2002). As mentioned above, the ring-polymer instanton method assumes that dependence of the splitting on overall rotation can be neglected, but the effects of rotational coupling are expected to be much weaker here than in the water dimer acceptor splitting

Table 6.9 – Tunnelling splittings in cm^{-1}, obtained from the instanton calculations, from previous DMC (Gregory and Clary, 1995*a*) and WKB (Takahashi et al., 2005) calculations, and from experiment (Liu et al., 1994; Keutsch et al., 2003*a*). The comparison of the bifurcation splittings is intended only as a rough guide (see text).

Pathway	instanton	DMC	WKB	expt.
$(H_2O)_3$ flip	100	22	37.93	43.52
$(D_2O)_3$ flip	36	9	30.84	20.54
$(H_2O)_3$ bifurcation	4.3(−2)	1.7(−2)	6.50(−3)	9.63(−3)
$(D_2O)_3$ bifurcation	1.4(−4)	4.0(−3)	2.54(−5)	1.66(−4)

(see §6.2.5).

Details of the $k = \pm 1, \pm 2$ bifurcation splitting pattern are sensitive to small changes in the elements $h_{\lambda\mu}$, since the pattern results from the interplay of several competing paths of roughly equal weight. It might be that neglect of anharmonicity in the instanton method introduces some small errors into the contributions made by some of the bifurcation paths. An attempt to replicate this pattern in detail would go therefore beyond the capabilities of the method.

One property, however, which the instanton approach should be able to describe well is the overall dependence of the bifurcation splitting on k. The instanton calculations predict that this splitting decreases markedly with increase in k (see Figures 6.7 and 6.8). This is contrary to the results which would be gained if only one B-type pathway dominated the spectrum (Takahashi et al., 2005). The disagreement arises because the instanton calculations predict that five of the bifurcation tunnelling paths contribute roughly equally to the splitting (see Table 6.7). Further work will be needed to decide if an analysis of the experimental data is consistent with Figures 6.7 and 6.8.

Table 6.9 gives numerical comparisons of the instanton tunnelling splittings with experiment and with the results of previous DMC and WKB calculations. Comparison of the flip splittings is straightforward, but comparison of the bifurcation splittings requires us to take into account the variation with k, which is present in the instanton results, but is not found in the WKB analysis (Takahashi et al., 2005), where only one pathway is considered. The DMC study treats all bifurcations in the same simulation, which gives an average splitting but not the spectral pattern. Table 6.7

gives the instanton bifurcation splittings corresponding to the $k = 0$ quartet, which is probably also where the experimental results are measured.

The instanton splittings are in good agreement with the experimental results and behave as we should expect from the derivation of the theory. As mentioned above, the $(H_2O)_2$ flip results are about a factor of two too large because of the low barrier, but the errors decrease for the deuterated case. The bifurcation splittings are also seen to be too large. This is probably because the surface is known to be very flat near the bifurcation transition state; it is for this reason that the number of flips in the minimum-energy pathways depend strongly on the PES. In particular, the values of Φ are very low for the A2, B1 and B3 pathways, and anharmonic effects are likely to be stronger in these cases. The results are seen, once again, to improve in the deuterated case.

The WKB results seem in excellent agreement for the $(H_2O)_2$ calculations. Indeed the reason why the WKB method does not particularly suffer from problems of anharmonicity for low barriers is because it neglects fluctuations about the pathway entirely. It is seen that they decrease in accuracy in the deuterated case, and that therefore the good agreement must have been at least partly fortuitous.

The DMC method is, by definition, exact but because of the necessity of sampling, the study used a significantly less accurate potential energy surface than PES(1,2,3) and enforced rigid monomers. This explains the observed error in the measurement of the flip and $k = 0$ bifurcation splitting.

The major advantage of the ring-polymer instanton method over the WKB and DMC methods is that no *a priori* model of the tunnelling needs to be determined such that the entire pattern is computed in a general way.

6.3.5 Comparison between different potential energy surfaces

We also took the opportunity to compare tunnelling splittings obtained from two less accurate (but computationally cheaper) potential energy surfaces with those obtained using PES(1,2,3). Table 6.7 gives the values of $h_{\lambda\mu}$ calculated using the PES(1,2,KS/WB) surface (Wang and Bowman, 2010) and the Thole-type model TTM3-F surface (Fanourgakis and Xantheas, 2008). It is seen that the PES(1,2,KS/WB) surface gives an adequate description of the tunnelling in water trimer, yielding values of $h_{\lambda\mu}$ that are within a factor of two of those obtained using PES(1,2,3).

The TTM3-F surface is designed to be inexpensive to evaluate in simulations of liquid water, and cannot realistically be expected to compete with PES(1,2,3) in accuracy. Nevertheless, this surface gives qualitatively the same prediction of the tunnelling dynamics as PES(1,2,3), yielding the same set of instanton paths as those shown in Figure 6.6 (including the B2 path, which is a first-order saddle, as for the other two surfaces), and yielding splitting patterns with the same overall structure as Figures 6.7 and 6.8. The splittings disagree with those obtained from PES(1,2,3) by at most a factor of six.

6.4 Application to water octamer

A number of theoretical investigations have been carried out on $(H_2O)_8$ but its tunnelling-splitting pattern has not before been computed. Stillinger and David (1980) performed the first geometry optimizations on the cluster using their polarizable water model (Stillinger and David, 1978). However, it was shown that with better potentials, the global minimum was found to have different structures (Brink and Glasser, 1984; Tsai and Jordan, 1991). It is now well accepted that the octamer has two low-lying minima with cage structures, i.e. a water molecule at each corner of a cuboid, and point groups D_{2d} or S_4, and that other minima have significantly higher energies (Wales and Ohmine, 1993; Xantheas and Aprà, 2004; Maeda and Ohno, 2007). This has also been confirmed by the experimental measurement of the infrared spectrum (Gruenloh et al., 1997).

For this study, the TTM3-F flexible water potential (Fanourgakis and Xantheas, 2008) was used which was shown to give order-of-magnitude estimates of tunnelling splittings in the previous applications (cf. §6.2 and §6.3). It is a refinement of TTM2-F which was shown to closely reproduce the *ab initio* binding energies and harmonic frequencies of the two lowest water octamer minima (Xantheas and Aprà, 2004). TTM3-F also correctly identifies these minima with point groups D_{2d} and S_4, where the latter isomer is only 0.005 kJ/mol higher in energy than the former. The harmonic frequencies ζ_j were calculated in both isomers which gave almost exactly the same harmonic zero-point vibrational energy of 509.2 kJ/mol of which 92.9 kJ/mol is in the intermolecular bonds.

In order to compute the tunnelling spectrum at low temperature, we need

only consider the D_{2d} and S_4 minima as these will be the only structures with any significant occupancy. There are an enormous number of possible tunnelling pathways between these wells, and we analyse the number of symmetry-related wells using the molecular symmetry group. This is the subgroup of permutation-inversion operations corresponding to pathways that are deemed feasible. Because of the mass terms in Eq. 5.16, any pathway which involves large displacements of oxygen atoms will correspond to large values of the action S_{kink}. The same is true for pathways which break covalent bonds, leading to high barriers. Such pathways are deemed unfeasible, will not lead to observable tunnelling splittings, and are excluded from the study.

The only pathways which can be considered feasible in water octamer are those which rotate individual monomers, exchanging the two hydrogen atoms. There are $2^8 = 256$ wells connected by these permutations for each isomer. Because of the presence of the S_4 symmetry element in both isomers, there are only two H_2O monomer environments: one in which the monomer donates two hydrogen bonds and accepts one (DAA), the other in which it accepts two and donates one (DAA) (Buck et al., 1998). Because of this symmetry, only four distinct pathways need to be calculated, two for D_{2d} and two for S_4.

6.4.1 Instanton pathways

These four pathways were optimized using the methods outlined in §6.2.2 with $M = 32$ and $\beta = 5000$ a.u. The initial starting point for each of the instanton tunnelling paths was taken to be the path in which half the beads were placed at the equilibrium geometry of well λ and the other half in well μ. A fixed-ended linear-polymer potential was used and the optimizer had no problems in pulling the central beads out of the wells and distributing them over the barrier as required. The computation was quite simple for this system because no skeletal rearrangement of the oxygen atoms was necessary.

The resulting instanton pathways are illustrated in Figure 6.9 and some results of the calculations are given in Table 6.10. The values of the tunnelling matrix elements obtained are too small to give rise to experimentally-measurable splitting patterns, and thus we did not try to obtain more accurate value of $h_{\lambda\mu}$ by converging M and β. We expect a fully-converged calculation to give slightly smaller actions but the matrix elements to remain at this order of magnitude. M and β were increased, along with a

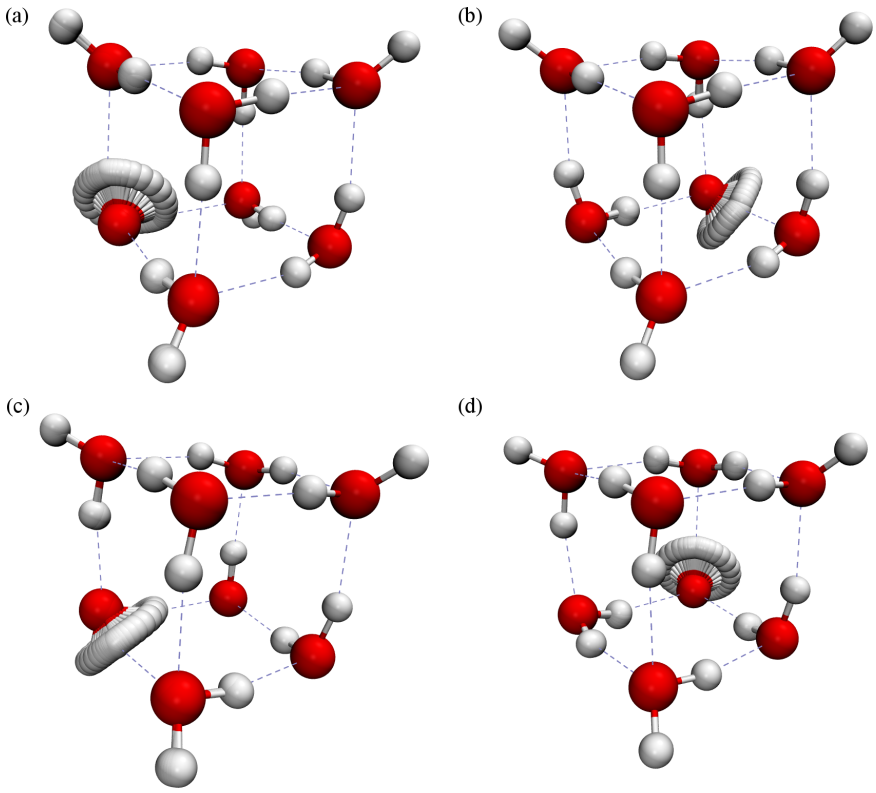

Figure 6.9 – Conflated snapshots of instanton tunnelling paths (kinks) for water octamer. The paths show the (a) D_{2d} (DDA), (b) D_{2d} (DAA), (c) S_4 (DDA) and (d) S_4 (DAA) rearrangements.

Table 6.10 – Actions, ratios and tunnelling matrix elements for the four pathways considered with $M = 32$ and $\beta\hbar = 5000$ a.u.

Pathway	$S_{\text{kink}}/\hbar$	Φ/a.u.	$-h_{\lambda\mu}/\text{cm}^{-1}$
D_{2d} (DDA)	33.98	23	3.9(−11)
D_{2d} (DAA)	28.67	118	1.4(−9)
S_4 (DDA)	33.93	25	3.7(−11)
S_4 (DAA)	28.99	123	9.8(−10)

releasing of the end-points of the linear polymer, only for the case of D_{2d} (DAA) but this resulted in very little change from the above figures. Further improvement could also be gained by using a better potential energy surface such as PES(1,2,3) which although it is a three-body potential and doesn't include higher-order terms, would still have provided a good description of the system (Wang et al., 2009). However, this is not expected to change the results by enough to make the pattern visible to experiment.

The reason for these small tunnelling splittings is obvious. In all four cases, at least two hydrogen bonds have to be broken along the tunnelling path which leads to a high action and therefore an unobservable tunnelling splitting. The DAA transitions are more labile probably because they do not bring their free hydrogen atoms so deep into the centre of the cluster. The pathways are similar to the bifurcations in the water trimer, except that the latter only break one hydrogen bond, and thus have an action about half of those for the octamer.

6.4.2 Tunnelling-splitting pattern

Although the tunnelling splittings are too small to be measured in current experiments, it may be useful for future studies to describe the resulting pattern, which is obtained by diagonalizing the tunnelling matrix $\mathbf{W}$.

Considering only the two feasible pathways described above leads to a sparse adjacency matrix $\mathbf{A}$ and therefore $\mathbf{W}$ has a simple structure which can be constructed using the following logic. Each of the 256 wells can be labelled by an eight-digit binary number where each bit describes the orientation of one of the monomers. Wells λ and μ are linked by a kink if and only if their binary codes differ in only one bit and in this case $W_{\lambda\mu}$ is set to $-2h_{\lambda\mu}$ (the factor of 2 is present because the rotation can be clockwise or anticlockwise). The splitting pattern is easily derived from diagonalizing this matrix, but is laborious to notate. However, since the DDA pathways are less-potent, the splitting pattern for each isomer is approximately

$$8h_{\mathrm{DAA}}\,(1), 4h_{\mathrm{DAA}}\,(4), 0\,(6), -4h_{\mathrm{DAA}}\,(4), -8h_{\mathrm{DAA}}\,(1),$$

where the degeneracies are in brackets.

Using the values of the matrix elements given in Table 6.10 for either isomer yields a tunnelling-splitting pattern for which the difference between

the highest and lowest energy levels is on the order of 2×10^{-8} cm^{-1}. This is far too small to be resolved by existing experimental techniques and so we expect both the D_{2d} and the S_4 isomers to exhibit spectra corresponding only to rotations and vibrations.

6.5 Other water clusters

Although the water dimer and trimer have been quite well studied, There is far less understanding of larger water clusters and application of the instanton method to these clusters would be very useful. The study of the octamer was inspired by difficulties in assigning the experimental spectrum (Saykally, 2012), and work is currently in progress on the heptamer and nonamer. Based on what we have learnt from the applications in this thesis, it is possible to make some predictions about the other water clusters (see Lee et al. (2000) for the relevant structures).

The tetramer forms a four-membered ring similar to the trimer's, but with point group symmetry S_4. Because there are an even number of dangling hydrogen atoms and therefore equal numbers of u and d, single flips are not degenerate rearrangements. Minimum-energy pathways describing bifurcations have not been found either (Keutsch and Saykally, 2001), and the expectation is that tunnelling motions occur in a concerted fashion, passing through second-order saddle points. However, minimum-action paths may exist where minimum-energy paths do not, and it has already been shown that the ring-polymer instanton method is able to pass through second-order saddles. We expect that a detailed study of this system will clarify the tunnelling dynamics.

Because the water pentamer's global minimum is a puckered ring geometry, it is necessary for the heavy oxygen atoms to move during the kinks (Keutsch and Saykally, 2001). This skeletal rearrangement means that many beads are needed to converge the instanton geometries and it may be necessary to develop new methods to space the beads more evenly before the splittings can be computed accurately. The asymmetry of the geometry also means that there will be a large number of kinks which contribute to the spectrum, for example there may be three different flips and a huge number of different bifurcations accompanied by zero, one, two, three or four flips (Wales and Walsh, 1996).

The hexamer global minimum is a cage structure, and there are four such structures very close (but not equal) in energy. No low-energy minimum-energy pathways corresponding to degenerate rearrangements have been found but only non-degenerate rearrangements including flips and bifurcations (Wales, 1999). The ring-polymer instanton theory may need to be extended to treat non-degenerate rearrangements before it can be applied to this system.

Water clusters larger than the hexamer also have cage structures for their global minima (Kim et al., 1999), which are less likely to require skeletal rearrangements than ring structures, and may only have few kinks which contribute. The action for a bifurcation in the octamer, where two hydrogen bonds were broken, was found to be roughly twice that of the bifurcation in the trimer, where one hydrogen bond was broken. This implies a very simple relationship between the number of hydrogen bonds broken and the magnitude of the tunnelling splitting such that it should be easy to guess which water clusters will give an observable splitting pattern and which will not. Following this premise, we conclude that the global minima of the water heptamer and nonamer should show a doublet in their tunnelling splittings, and the "butterfly" structure of the decamer a triplet, but it is unlikely that any splittings of the decamer's prism structure will be visible.

Chapter 7

Conclusions and Future Work

We have, in this work, shown how the application of RPMD rate theory can be justified in the deep-tunnelling regime by providing a link between its transition-state-theory limit (RPTST) and a free-energy version of the $\mathrm{Im}\,F$ instanton rate. We have explained why, for asymmetric reaction in the deep-tunnelling regime, a cone is the appropriate shape for the optimal dividing surface in the space of the ring-polymer normal modes, and shown that RPTST using this dividing surface leads only to a minor discrepancy (about 5%) from the RPMD rate for the one-dimensional systems tested. As a result of these findings, we have explained why CMD and QTST methods which use planar dividing surfaces based only on the centroid greatly overestimate the rate for these asymmetric reactions. It is shown that the only remaining difference between the two methods, RPMD and the free-energy instanton, is in the treatment of the unstable mode. This explains why RPMD has been seen to perform so well in the deep-tunnelling regime, and shows that RPMD is expected to underestimate the rate for symmetric barriers and overestimate it for strongly asymmetric barriers.

The saddle point on the ring-polymer surface is a finite-difference approximation to a periodic orbit in imaginary time—known as an instanton. These saddle points can be located using standard transition-state searches, and this provides a practical method for locating instantons in multidimensional systems. We followed the derivations in the standard instanton literature (Benderskii et al., 1994), but found that using the discretized

ring-polymer formulation from the start greatly simplified the derivation, avoiding functional determinants, and lead directly to a practical method for computing the rate of reactions. We call this the ring-polymer instanton method, and it is equivalent to the harmonic QTST developed simultaneously and independently by (Andersson et al., 2009).

We have performed numerical tests of the ring-polymer instanton method by computing the rates for the Eckart barrier and the collinear $H + H_2$ reaction, where the results compared very favourably with the exact quantum rate constants. The method was also applied to hydrogen exchange reactions in the water dimer and trimer. These applications were inspired by a prediction made by Bove et al. (2009) that concerted proton transfer occurs in the hexagonal rings in ice. However, we could not continue to study larger water systems because accurate potential energy surfaces which treat proton transfer were not available. For example, the polarizable surface of Stillinger and David (1978) and its derivatives (Halley et al., 1993) have unphysical minima either side of the transition states for the concerted transfer which makes it impossible to locate instantons. However, with better potentials, there is no intrinsic reason why the method cannot be used to calculate rates for proton transfer in a six-fold ring embedded in a ice structure with periodic boundary conditions, especially if the beads described only six of the molecules while the remainder are held fixed. However, the rates calculated for the trimer appear very low, and it is doubtful that the rate of a similar concerted proton transfer in a six-membered ring is large enough to have been the rearrangement observed by their experiment.

Work is in progress to link the method to the electronic-structure package MOLPRO (Werner et al., 2010) such that the potential could be computed "on the fly" and these systems could be treated; preliminary results show that this goal is feasible. With such a tool, one could easily apply the method to many problems. For example, it has recently been discovered that methylhydroxycarbene makes an unexpected rearrangement at low temperature, choosing to tunnel through a high barrier rather than pass over a lower barrier (Schreiner et al., 2011; Carpenter, 2011). This is the type of problem to which the ring-polymer instanton method could easily be applied and would be able to identify the pathway preferred at low temperature.

A related ring-polymer instanton method has also been derived for computing the tunnelling-splitting patterns of polyatomic molecules and molecu-

lar clusters. The most important application of these calculations has been on water clusters, for which there is considerable interest in gaining a better understanding of the interatomic forces. Theoretical calculations can aid the assignment of experimental spectra and the construction of higher quality potentials. In this work the water dimer, trimer and octamer were treated. The results on the dimer reproduced the experimental patterns well except for the tunnelling splitting through the smallest barrier. We have shown that this error, which was only about a factor of two, arises from a breakdown in the validity of defining a non-tunnelling system, and is to be expected for tunnelling through low barriers.

Although other techniques, including WKB and DMC, have been used to compute the splitting pattern for the water trimer, they had not been able to correctly identify the tunnelling pathways and hence describe the experimental spectrum. The WKB approaches, which used the minimum-energy pathways to describe the tunnelling, found that only one of the bifurcation pathways contributed to the spectrum, although the particular rearrangement depended on the PES used. The DMC approach fixed the node of the excited-state wave function to include all bifurcation rearrangements together and is therefore unable to describe the splitting pattern. The instanton method does not rely on *a priori* knowledge of the tunnelling pathway or the nodal planes of the wave function, and was therefore able to show that five, of the possible six, bifurcation pathways contribute to the pattern; this provides an explanation for the appearance so-called "anomalous" quartets.

Tunnelling splitting calculations on the octamer were prompted by recent experiments (Saykally, 2012), in the hope a theoretical approach would improve the understanding of the spectrum. In this case, no splittings which would be visible to experiment were found, but based on our experiences with this example, we expect that it will be possible to compute visible splittings in many other water clusters, including the heptamer and nonamer for which work is in progress. Water clusters have been studied up to $(H_2O)_{22}$ using the PES(1,2,3) potential (Wang et al., 2011) and there is no reason why the ring-polymer instanton method could not be applied to all of them.

Appendices

Appendix A

TST and shallow-tunnelling corrections

There are a number of forms of classical TST which treat the modes perpendicular to the reaction coordinate in different ways. All, however, assume that the system does not recross the dividing surface $\sigma(\mathbf{x}) = 0$ and that no tunnelling takes place along the reaction coordinate.

For an f-dimensional system described by Eq. 2.33,

$$k_{\mathrm{TST}}(\beta)Q_{\mathrm{r}}(\beta) = \frac{1}{(2\pi\hbar)^f}\int \mathrm{d}\mathbf{p}\int \mathrm{d}\mathbf{x}\,\mathrm{e}^{-\beta H(\mathbf{p},\mathbf{x})}\delta[\sigma(\mathbf{x})]v_\sigma(\mathbf{p},\mathbf{x})h[v_\sigma(\mathbf{p},\mathbf{x})]. \tag{A.1}$$

Converting to mass-weighted coordinates and taking the steepest-descent approximation gives harmonic transition-state theory (hTST):

$$k_{\mathrm{hTST}}(\beta)Q_{\mathrm{r}}(\beta) = \frac{1}{2\pi\hbar\beta}\prod_{j=2}^{f}\frac{1}{\beta\hbar\zeta_j}\,\mathrm{e}^{-\beta V^\ddagger}, \tag{A.2}$$

where we have assumed the reaction coordinate follows the imaginary mode corresponding to ζ_1 at the saddle point $\mathbf{x}^\ddagger$. If there are translational and rotational degrees of freedom at the transition state, these modes are excluded from the product, and the rate is multiplied by the appropriate factors (cf. §2.2.1).

Eyring's TST separates the integral along its normal modes and treats the modes perpendicular to the reaction coordinate using approximations to the quantum-mechanical partition functions. For a transition state with

vibrational modes only,

$$k_{\mathrm{Eyring}}(\beta)Q_{\mathrm{r}}(\beta) = \frac{1}{2\pi\hbar\beta}\prod_{j=2}^{f}\frac{1}{2\sinh\left(\beta\hbar\zeta_j/2\right)}\,\mathrm{e}^{-\beta V^{\ddagger}}, \tag{A.3}$$

and for a non-linear geometry with three translational, three rotational and $f-6$ vibrational degrees of freedom,

$$k_{\mathrm{Eyring}}(\beta)Q_{\mathrm{r}}(\beta) = \frac{1}{2\pi\hbar\beta}\left(\frac{M}{2\pi\beta_N\hbar^2}\right)^{3/2}\sqrt{\frac{8\pi\det\mathbf{I}}{\beta_N^3\hbar^6}}\prod_{j=8}^{f}\frac{1}{2\sinh\left(\beta\hbar\zeta_j/2\right)}\,\mathrm{e}^{-\beta V^{\ddagger}}, \tag{A.4}$$

where M, $\mathbf{I}$ and ζ_j are defined in §2.2.1.

Above T_{c} where classical thermodynamic fluctuations dominate, the $\operatorname{Im}F$ premise takes a different form. We assume that the rate can be determined by (Affleck, 1981)

$$k(\beta) \approx -\frac{\beta\omega_{\mathrm{b}}}{\pi}\operatorname{Im}F \approx \frac{\omega_{\mathrm{b}}}{\pi}\frac{\operatorname{Im}Q(\beta)}{\operatorname{Re}Q(\beta)}, \tag{A.5}$$

and that we can calculate an analytic continuation of the integral by steepest descent about the collapsed-bead saddle point $x_{i,j} = x_j^{\ddagger}$ in the same way as in Chapter 3. The only difference is that there is no zero-frequency mode. After converting to normal-mode coordinates (Eq. 2.22),

$$\operatorname{Im}Q(\beta) = \frac{1}{2}\left(\frac{1}{2\pi\beta_N\hbar^2}\right)^{N/2}\prod_{k,j}\sqrt{\frac{2\pi}{\beta_N|\omega_{k,j}|^2}}\,\mathrm{e}^{-\beta_N N V^{\ddagger}} \tag{A.6}$$

$$= \frac{1}{2}\prod_{k,j}\left|\frac{1}{\beta_N\hbar\omega_{k,j}}\right|\mathrm{e}^{-\beta V^{\ddagger}}, \tag{A.7}$$

such that

$$k(\beta)Q_{\mathrm{r}}(\beta) \approx \frac{1}{2\pi\beta_N\hbar}{\prod_{k}}'\prod_{j=1}^{f}\frac{1}{\beta_N\hbar\omega_{k,j}}\,\mathrm{e}^{-\beta V^{\ddagger}}, \tag{A.8}$$

where the imaginary frequency $\omega_{0,1} = \omega_{\mathrm{b}}$ is excluded from the product. This reduces to $k_{\mathrm{hTST}}(\beta)$ for $N = 1$ and gives the rate constant equivalent to Wigner's TST correction for tunnelling through a parabolic barrier (Wigner,

1932) in the large N limit:

$$k(\beta)Q_{\mathrm{r}}(\beta) \approx \frac{\omega_{\mathrm{b}}}{2\pi}\left|\prod_{k}\frac{1}{\beta_N\hbar\omega_{k,1}}\right|\prod_{k}\prod_{j=2}^{f}\frac{1}{\beta_N\hbar\omega_{k,j}}\,\mathrm{e}^{-\beta V^{\ddagger}} \tag{A.9a}$$

$$= \frac{\omega_{\mathrm{b}}}{2\pi}\frac{1}{2\sin\left(\beta\hbar\omega_{\mathrm{b}}/2\right)}\prod_{j=2}^{f}\frac{1}{2\sinh\left(\beta\hbar\zeta_j/2\right)}\,\mathrm{e}^{-\beta V^{\ddagger}} \tag{A.9b}$$

$$= \frac{\hbar\beta\omega_{\mathrm{b}}/2}{\sin\left(\hbar\beta\omega_{\mathrm{b}}/2\right)}\,k_{\mathrm{Eyring}}(\beta)Q_{\mathrm{r}}(\beta), \tag{A.9c}$$

where we have used the same relation as was used to derive Eq. 2.27 but with $\omega_s = \mathrm{i}\omega_b$. This is correct for a parabolic barrier and hence only applicable to systems above the cross-over temperature and explains the rationality behind Eq. A.5.

Appendix B

Optimization methods

There have been many methods developed for the optimization of functions going back at least to Newton; we shall discuss some of the most useful specifically in relation to locating instantons. By *optimization*, we mean both minimization of functions and transition-state searches as both of these are necessary for locating the instantons described in this thesis. It is generally accepted that minimization is a far easier because one only has to travel downhill in each degree of freedom (Wales, 2003). Note that *global* minimization, which is known to be a difficult problem in general, is not necessary for the work in this project. Indeed we know the global minimum from the outset: a collapsed ring-polymer at the bottom of the well, but the loose-ended instanton in a double well system is a *local* minimum. With expensive potentials, all the algorithms can be greatly sped-up by computing the ring-polymer potential in a parallelized way with each bead geometry assigned to a separate CPU. Unfortunately, however, there is no simple way of performing the diagonalizations needed to calculate the determinant in a parallel manner. Any number of the following methods could be used in the optimization, including manually prodding the geometry, because once the gradient goes to zero and the correct number of negative eigenvalues appear, the geometry must be correct.

All the methods are iterative, moving the system closer to the solution one step at a time. Newton-like methods, also known as mode-following methods, employ a local quadratic approximation and use the Hessian to choose a direction in which to make a step. One example is the stream-bed walk algorithm (Nichols et al., 1990) for which the Hessian is computed and

diagonalized at each iteration and a step chosen downhill in the direction of all eigenvectors for minimizations but uphill in the direction of the lowest eigenvector only for transition-state searches. The step length depends on the signs and magnitudes of the first two eigenvalues. This routine can be quite slow when applied to expensive potentials, especially if the Hessian must be computed by finite-differences. However, when applied to the half ring-polymer form in Eq. 3.40, the ring-polymer Hessian can be diagonalized efficiently as a consequence of its banded nature. The algorithm for computing transition-states was modified slightly for situations where the geometry had two negative eigenvalues (as is quite common in ring-polymer searches where the second eigenvalue is often close to zero). That is, in the notation of the paper:

- take $\alpha = 1.0$ and $\lambda = (h_1 + 2h_2)/4$ if $h_2 > h_1/2$;
- take $\alpha = (h_1 - h_2)/h_2$ and $\lambda = (h_1 + 3h_2)/4$ otherwise.

Quasi-Newton methods avoid the computation of the Hessian at each step altogether by using an update formula* to give an approximation based on the previous geometries and gradients. Many update formulae have been suggested but the BFGS method seems to have been deemed the best for minimization problems. A variant of this is the limited-memory version L-BFGS (Nocedal, 1980), which avoids even storing the Hessian in memory and saves time by not performing the diagonalization. For transition-state searches, there is no obvious winner. In this project, we have tested a few alternative methods including the method of Baker (1986), the stream-bed walk algorithm with a Powell update, and the update scheme of Bofill (1994) which was found to be the most efficient for locating instantons in molecules with about ten atoms in the study by Rommel et al. (2011). However, this may not be the most efficient in all cases, because even when exploiting a banded-matrix eigenvalue solver, diagonalization can be the bottleneck in the algorithm for systems with very large numbers of atoms. It is sometimes necessary to project out the zero-eigenvalue modes corresponding to translation, rotation and permutation of the ring polymer, especially for Bofill's scheme, which involves inverting the Hessian. For these algorithms, an initial guess for the Hessian must be supplied. We

*See Fletcher (1987) for the definitions of the various update formulae mentioned.

have found that it is often more efficient to use the correct Hessian rather than an approximation in this case. The updated Hessian resulting from the optimization algorithm is usually not accurate enough for use to compute the ring polymer's fluctuations, and so it should be recalculated.

To avoid diagonalization of the Hessian, one can employ a modified eigenvector-following algorithm which uses an iterative method to compute the lowest eigenvalue and its associated eigenvector. Alternatively, one does not need to calculate the Hessian at all, but can still estimate the lowest eigenvector using a conjugate-gradient approach (Munro and Wales, 1999). These methods are related to the dimer method (Henkelman and Jónsson, 1999) and its improved version (Kästner and Sherwood, 2008), with which transition states can be located using minimization algorithms on a pair of geometries separated by a fixed "bond", along which the gradient is reversed. It is no surprise that these methods are less stable than the Newton and quasi-Newton algorithms, but we predict that they will nonetheless become more useful as instanton theory is applied to larger and larger systems.

Minimizations can also be performed without any reference to a Hessian using methods based on molecular dynamics with friction terms designed to stop the trajectory at the bottom of a well. These inertial engines, which include quick-min (Henkelman and Jónsson, 1999) and FIRE (Bitzek et al., 2006), have very little overhead per iteration, but typically take more steps than the Newton-type methods. In cases where the ring-polymer surface is rough, they have been beneficial, as they are able to jump over small barriers in order to fall into the correct well (a Beccara et al., 2010). However, for the uses of instantons in this work, the surfaces are smooth, and this is not a problem.

The nudged elastic band and string methods (Sheppard et al., 2008) are excellent for computing minimum-energy paths and thereby locating unknown transition states between two minima. However, these double-ended searches are less useful for finding instantons, as we already have a pretty good idea of where the instanton is—near the classical transition state. It may be possible, however, to apply them to locate minimum-action paths, i.e. instantons in double wells used to compute tunnelling splittings.

Appendix C

RPMD velocity Verlet

The ring-polymer trajectories were calculated using a symplectic integrator based on alternating free harmonic ring-polymer and external-force steps (Craig and Manolopoulos, 2004). The velocity Verlet algorithm was used to calculate the Newtonian dynamics in normal-mode phase space $(\mathbf{w}, \mathbf{q})$, using the following (python-like) pseudo-code:

```
w += dt * Fext / 2
q[0] += dt * w[0] / mass
z[1:] = (q[1:]-1j*w[1:]/mass/omega[1:]) * exp(1j*omega[1:]*dt)
q[1:] = z[1:].real
w[1:] = - mass * (z[1:].imag * omega[1:])
q *= sqrt(N/2)
q[0] *= sqrt(2)
q[N-1] *= sqrt(2)
for j in range(f):
    x[:,j] = irfft(q[:,j])
Fextx = externalForce(x)
for j in range(f):
    Fextq[:,j] = rfft(Fextx[:,j])
Fextq *= sqrt(2/N)
Fextq[0] /= sqrt(2)
Fextq[N-1] /= sqrt(2)
w += dt * Fext / 2
```

where `dt` is the time step, `omega[:]` the frequencies of a free ring polymer, `rfft` the forward real Fourier transform and `irfft` its inverse. The function

`externalForce(x)` returns the force according to the PES for each bead geometry. NB in this code, the normal modes are arranged in order of increasing values of ω_k, i.e. `q[:]`$= (q_0, q_1, q_{-1}, q_2, q_{-2}, \ldots, q_{N/2})$.

Appendix D

Constrained RPMD

Following the method of RATTLE (Andersen, 1983), the $\sigma = 0$ constraint (Eq. 4.26) on the dynamics of the ring polymer, represented by normal-mode phase-space coordinates $(\mathbf{w}, \mathbf{q})$, is applied at each time step using the constraint force

$$\mathbf{G}(\mathbf{q}) = -\lambda \nabla \sigma(\mathbf{q}) = -\lambda \left(\cos\phi, \frac{q_1}{r}\sin\phi, \frac{q_{-1}}{r}\sin\phi, 0, \ldots, 0 \right). \tag{D.1}$$

The first part of the RPMD velocity Verlet step (cf. Appendix C) is taken to give $\mathbf{q}'_t$ and the constraint force added to give

$$\mathbf{q}_{t+\Delta t} = \mathbf{q}_t + \frac{\Delta t}{m}\mathbf{w}_t + \frac{\Delta t^2}{2m}[\mathbf{F}(\mathbf{q}_t) - \mathbf{G}_{\mathbf{q}}(\mathbf{q}_t)] \tag{D.2}$$

$$= \mathbf{q}'_t - \frac{\Delta t^2}{2m}\lambda_{\mathbf{q}} \nabla \sigma(\mathbf{q}_t), \tag{D.3}$$

where λ_q is chosen to solve the constraint at time $t + \Delta t$:

$$\sigma(\mathbf{q}_{t+\Delta t})^2 = (q_1^2 + q_{-1}^2)\sin^2\phi - (\sigma_0 - q_0\cos\phi)^2 = 0, \tag{D.4}$$

which is solved to give the correct root of the quadratic equation (Press et al., 1992, §5.6)

$$\lambda_{\mathbf{q}} = \frac{2c}{-b + \sqrt{b^2 - 4ac}}, \tag{D.5}$$

where

$$a = \frac{\Delta t^4}{4m^2}\left[(\nabla_1\sigma)^2 + (\nabla_{-1}\sigma)^2\right]\sin^2\phi - \frac{\Delta t^4}{4m^2}(\nabla_0\sigma)^2\cos^2\phi, \tag{D.6a}$$

$$b = -2\frac{\Delta t^2}{2m}(q_1'\nabla_1\sigma + q_{-1}'\nabla_{-1}\sigma)\sin^2\phi - 2\left(\sigma_0 - q_0'\cos\phi\right)\frac{\Delta t^2}{2m}\nabla_0\sigma\cos\phi, \tag{D.6b}$$

$$c = (q_1'^2 + q_{-1}'^2)\sin^2\phi - \left(\sigma_0 - q_0'\cos\phi\right)^2. \tag{D.6c}$$

There is a second constraint on the momenta

$$\mathbf{w}_{t+\Delta t} = \mathbf{w}_t + \frac{\Delta t}{2}[\mathbf{F}(\mathbf{q}_t) + \mathbf{G}_\mathbf{q}(\mathbf{q}_t) + \mathbf{F}(\mathbf{q}_{t+\Delta t}) + \mathbf{G}_\mathbf{w}(\mathbf{q}_{t+\Delta t})] \tag{D.7}$$

$$= \mathbf{w}_t' - \frac{\Delta t}{2}\lambda_\mathbf{w}\nabla\sigma(\mathbf{q}_{t+\Delta t}). \tag{D.8}$$

$\lambda_\mathbf{w}$ is chosen to force

$$m\frac{\mathrm{d}\sigma(\mathbf{q}_{t+\Delta t})}{\mathrm{d}t} = w_0'\cos\phi + \frac{q_1 w_1' + q_{-1}w_{-1}'}{r}\sin\phi = 0, \tag{D.9}$$

which gives

$$\lambda_\mathbf{w} = 2\frac{w_0'\cos\phi + (q_1 w_1' + q_{-1}w_{-1}')\sin\phi/r}{\Delta t\nabla_0\sigma\cos\phi + \Delta t(q_1\nabla_1\sigma + q_{-1}\nabla_{-1}\sigma)\sin\phi/r}. \tag{D.10}$$

Constant temperature dynamics are provided by the Andersen thermostat (Andersen, 1980) which resamples the momenta of the beads at random intervals, choosing new values for all modes w_k except $k = 0$ from the Maxwell-Boltzmann distribution $\mathcal{N}(0, m/\beta_N)$ and choosing w_0 to ensure the constraint expressed in Eq. D.9.

Appendix E

Factorization of the ratio of determinants in the tunnelling-splitting calculations

We wish to prove Eq. 5.19,

$$\frac{\det' \mathbf{G}}{\det \mathbf{G_0}} = \left(\frac{\det' \mathbf{J}}{\det \mathbf{J_0}}\right)^n, \tag{E.1}$$

where $\mathbf{G}$ is the Hessian for an n-kink minimum on an N-bead ring-polymer potential surface, $\mathbf{J}$ is the Hessian for a single-kink minimum on the corresponding M-bead fixed-ended linear-polymer surface, and $N = nM$. $\mathbf{G_0}$ and $\mathbf{J_0}$ are the corresponding Hessians that are obtained when all the beads are located at one of the wells. The proof holds in the $M \to \infty$ limit and is developed first for the simplest case of an instanton with $n = 2$ kinks in a one-dimensional system, from which we generalize to $n > 2$ and then to multidimensional systems.

We first expand $\det \mathbf{J}$ along the k^{th} row in terms of of its first and second square minors using the shorthand $\alpha_k = 2 + (\beta_N \hbar)^2 V''(x_k)/m$. For example

with $M = 7$ and $k = 4$,

$$
\begin{aligned}
(\beta_N\hbar)^{14}\det\mathbf{J} &= \begin{vmatrix}
\alpha_1 & -1 & \cdot & \cdot & \cdot & \cdot & \cdot \\
-1 & \alpha_2 & -1 & \cdot & \cdot & \cdot & \cdot \\
\cdot & -1 & \alpha_3 & -1 & \cdot & \cdot & \cdot \\
\cdot & \cdot & -1 & \alpha_4 & -1 & \cdot & \cdot \\
\cdot & \cdot & \cdot & -1 & \alpha_5 & -1 & \cdot \\
\cdot & \cdot & \cdot & \cdot & -1 & \alpha_6 & -1 \\
\cdot & \cdot & \cdot & \cdot & \cdot & -1 & \alpha_7
\end{vmatrix} \\
&= \begin{vmatrix}
\alpha_1 & -1 & \cdot & \cdot & \cdot & \cdot \\
-1 & \alpha_2 & \cdot & \cdot & \cdot & \cdot \\
\cdot & -1 & -1 & \cdot & \cdot & \cdot \\
\cdot & \cdot & -1 & \alpha_5 & -1 & \cdot \\
\cdot & \cdot & \cdot & -1 & \alpha_6 & -1 \\
\cdot & \cdot & \cdot & \cdot & -1 & \alpha_7
\end{vmatrix} + \alpha_4 \begin{vmatrix}
\alpha_1 & -1 & \cdot & \cdot & \cdot & \cdot \\
-1 & \alpha_2 & -1 & \cdot & \cdot & \cdot \\
\cdot & -1 & \alpha_3 & \cdot & \cdot & \cdot \\
\cdot & \cdot & \cdot & \alpha_5 & -1 & \cdot \\
\cdot & \cdot & \cdot & -1 & \alpha_6 & -1 \\
\cdot & \cdot & \cdot & \cdot & -1 & \alpha_7
\end{vmatrix} + \begin{vmatrix}
\alpha_1 & -1 & \cdot & \cdot & \cdot & \cdot \\
-1 & \alpha_2 & -1 & \cdot & \cdot & \cdot \\
\cdot & -1 & \alpha_3 & -1 & \cdot & \cdot \\
\cdot & \cdot & \cdot & -1 & -1 & \cdot \\
\cdot & \cdot & \cdot & \cdot & \alpha_6 & -1 \\
\cdot & \cdot & \cdot & \cdot & -1 & \alpha_7
\end{vmatrix} \\
&= \begin{vmatrix}
\alpha_1 & -1 & \cdot & \cdot & \cdot \\
-1 & \alpha_2 & \cdot & \cdot & \cdot \\
\cdot & \cdot & \alpha_5 & -1 & \cdot \\
\cdot & \cdot & -1 & \alpha_6 & -1 \\
\cdot & \cdot & \cdot & -1 & \alpha_7
\end{vmatrix} + \begin{vmatrix}
\alpha_1 & -1 & \cdot & \cdot & \cdot \\
-1 & \alpha_2 & \cdot & \cdot & \cdot \\
\cdot & -1 & \cdot & \cdot & \cdot \\
\cdot & \cdot & -1 & \alpha_6 & -1 \\
\cdot & \cdot & \cdot & -1 & \alpha_7
\end{vmatrix} + \alpha_4 \begin{vmatrix}
\alpha_1 & -1 & \cdot \\
-1 & \alpha_2 & -1 \\
\cdot & -1 & \alpha_3
\end{vmatrix} \begin{vmatrix}
\alpha_5 & -1 & \cdot \\
-1 & \alpha_6 & -1 \\
\cdot & -1 & \alpha_7
\end{vmatrix} \\
&\quad + \begin{vmatrix}
\alpha_1 & -1 & \cdot & \cdot & \cdot \\
-1 & \alpha_2 & -1 & \cdot & \cdot \\
\cdot & \cdot & \cdot & -1 & \cdot \\
\cdot & \cdot & \cdot & \alpha_6 & -1 \\
\cdot & \cdot & \cdot & -1 & \alpha_7
\end{vmatrix} + \begin{vmatrix}
\alpha_1 & -1 & \cdot & \cdot & \cdot \\
-1 & \alpha_2 & -1 & \cdot & \cdot \\
\cdot & -1 & \alpha_3 & \cdot & \cdot \\
\cdot & \cdot & \cdot & \alpha_6 & -1 \\
\cdot & \cdot & \cdot & -1 & \alpha_7
\end{vmatrix}. \qquad \text{(E.2)}
\end{aligned}
$$

The second and fourth terms are 0 because the columns are not linearly independent. This is most easily seen by considering adding scalar multiples of the third column to the others so as to make two columns identical within a constant factor. Therefore,

$$
(\beta_N\hbar)^{14}\det\mathbf{J} = \begin{vmatrix} \alpha_1 & -1 \\ -1 & \alpha_2 \end{vmatrix} \begin{vmatrix} \alpha_5 & -1 & \cdot \\ -1 & \alpha_6 & -1 \\ \cdot & -1 & \alpha_7 \end{vmatrix} + \alpha_4 \begin{vmatrix} \alpha_1 & -1 & \cdot \\ -1 & \alpha_2 & -1 \\ \cdot & -1 & \alpha_3 \end{vmatrix} \begin{vmatrix} \alpha_5 & -1 & \cdot \\ -1 & \alpha_6 & -1 \\ \cdot & -1 & \alpha_7 \end{vmatrix} + \begin{vmatrix} \alpha_1 & -1 & \cdot \\ -1 & \alpha_2 & -1 \\ \cdot & -1 & \alpha_3 \end{vmatrix} \begin{vmatrix} \alpha_6 & -1 \\ -1 & \alpha_7 \end{vmatrix}, \qquad \text{(E.3)}
$$

and more generally,

$$
(\beta_N\hbar)^{2M}\det\mathbf{J} \equiv p_{1:M} = \alpha_k p_{1:k-1} p_{k+1:M} - p_{1:k-2} p_{k+1:M} - p_{1:k-1} p_{k+2:M}, \qquad \text{(E.4)}
$$

where $p_{i:j}$ is the determinant of the submatrix of $(\beta_N\hbar)^2\mathbf{J}$ starting at row and column i and ending at row and column j. The N-bead cyclic determinant of $\mathbf{G}$ can be expanded in the same way along the first row; for example, with

$N = 5$, this gives

$$
\begin{aligned}
(\beta_N\hbar)^{10}\det\mathbf{G} &= \begin{vmatrix} \alpha_1 & -1 & \cdot & \cdot & -1 \\ -1 & \alpha_2 & -1 & \cdot & \cdot \\ \cdot & -1 & \alpha_3 & -1 & \cdot \\ \cdot & \cdot & -1 & \alpha_4 & -1 \\ -1 & \cdot & \cdot & -1 & \alpha_5 \end{vmatrix} \\
&= \alpha_1 \begin{vmatrix} \alpha_2 & -1 & \cdot & \cdot \\ -1 & \alpha_3 & -1 & \cdot \\ \cdot & -1 & \alpha_4 & -1 \\ \cdot & \cdot & -1 & \alpha_5 \end{vmatrix} + \begin{vmatrix} -1 & -1 & \cdot & \cdot \\ \cdot & \alpha_3 & -1 & \cdot \\ \cdot & -1 & \alpha_4 & -1 \\ -1 & \cdot & -1 & \alpha_5 \end{vmatrix} - \begin{vmatrix} -1 & \alpha_2 & -1 & \cdot \\ \cdot & -1 & \alpha_3 & -1 \\ \cdot & \cdot & -1 & \alpha_4 \\ -1 & \cdot & \cdot & -1 \end{vmatrix} \\
&= \alpha_1 \begin{vmatrix} \alpha_2 & -1 & \cdot & \cdot \\ -1 & \alpha_3 & -1 & \cdot \\ \cdot & -1 & \alpha_4 & -1 \\ \cdot & \cdot & -1 & \alpha_5 \end{vmatrix} - \begin{vmatrix} \alpha_3 & -1 & \cdot \\ -1 & \alpha_4 & -1 \\ \cdot & -1 & \alpha_5 \end{vmatrix} + \begin{vmatrix} -1 & \cdot & \cdot \\ \alpha_3 & -1 & \cdot \\ -1 & \alpha_4 & -1 \end{vmatrix} \\
&\qquad + \begin{vmatrix} -1 & \alpha_3 & -1 \\ \cdot & -1 & \alpha_4 \\ \cdot & \cdot & -1 \end{vmatrix} - \begin{vmatrix} \alpha_2 & -1 & \cdot \\ -1 & \alpha_3 & -1 \\ \cdot & -1 & \alpha_4 \end{vmatrix}
\end{aligned} \tag{E.5}
$$

and therefore, more generally,

$$
(\beta_N\hbar)^{2N}\det\mathbf{G} = \alpha_1 p_{2:N} - p_{3:N} - p_{2:N-1} \pm 2. \tag{E.6}
$$

The final term is positive or negative depending on whether N is even or odd. However, it is negligible in comparison with the other terms which grow exponentially with N.

The determinant of $\mathbf{J_0}$ and its submatrices can be evaluated in closed form (Kleinert, 2006, §2.3.2) by writing them as a product of eigenvalues and using 1.391.1 and 1.396.1 from Gradshteyn and Ryzhik (2000) to give

$$
q_A = \frac{\sinh(A+1)\tilde{\omega}}{\sinh\tilde{\omega}}, \qquad \tilde{\omega} = 2\sinh^{-1}\frac{\beta_N\hbar\omega_\mathrm{s}}{2}, \tag{E.7}
$$

where $\omega_\mathrm{s} = \sqrt{V''(\pm x_0)/m}$, and q_A is the determinant of the first A rows and columns of $(\beta_N\hbar)^{2N}\mathbf{J_0}$. In what follows A will correspond to a substantial fraction of the M beads, and hence we shall have

$$
\lim_{M\to\infty} q_A = \frac{\exp(A+1)\tilde{\omega}}{2\sinh\tilde{\omega}}. \tag{E.8}
$$

Now, almost all of the elements of the Hessian $\mathbf{J}$ are identical to those of $\mathbf{J_0}$, since, in the $M \to \infty$ limit, most of the beads in the linear polymer corresponding to $\mathbf{J}$ are at $\pm x_0$, and there is just a tiny section of the polymer along which the beads follow the kink trajectory linking $\pm x_0$. We can thus partition the polymer into three stretches in the intervals $1 < A < M - B < M$. The middle stretch contains $K = M - A - B$ beads, and contains the tiny fraction of beads extending between $\pm x_0$, which we take to be a much smaller number

than M. It then follows that, in the $M \to \infty$ limit,

$$p_{1:A} = q_A, \tag{E.9}$$

$$p_{M-B+1:M} = q_B, \tag{E.10}$$

and that cutting $p_{1:M}$ twice, using Eq. E.4, at rows A and $M-B+1$ gives

$$\begin{aligned} p_{1:M} &= (\alpha_A q_{A-1} - q_{A-2})\, p_{A+1:M} - q_{A-1} p_{A+2:M} \\ &= (\alpha_A q_{A-1} - q_{A-2})\,(\alpha_{M-B+1} p_{A+1:M-B} q_{B-1} - p_{A+1:M-B-1} q_{B-1} - p_{A+1:M-B} q_{B-2}) \\ &\quad - q_{A-1}\,(\alpha_{M-B+1} p_{A+2:M-B} q_{B-1} - p_{A+2:M-B-1} q_{B-1} - p_{A+2:M-B} q_{B-2}) \\ &= \mathrm{e}^{(M-K)\tilde{\omega}} \times (\text{linear combination of } p_{A+i:M-B-j}), \quad i,j \in \{1,2\}. \end{aligned} \tag{E.11}$$

One can therefore move the position of the kink along the the linear polymer without changing the value of $p_{1:M}$. We label all determinants that have A rows and columns and that contain at least one kink by p_A. Many rules follow from Eq. E.11, of which the most useful are (in the $M \to \infty$ limit):

$$p_M p_M = p_{M+1} p_{M-1}, \tag{E.12}$$

$$p_M q_{M-1} = p_{M-1} q_M, \tag{E.13}$$

$$p_N = \alpha p_{1:k-1} p_{k+1:N} - 2 p_{1:k-2} p_{k+1:N}, \tag{E.14}$$

$$(\beta_N \hbar)^{2N} \det \mathbf{G} = \alpha p_{N-1} - 2 p_{N-2}, \tag{E.15}$$

where $\alpha = 2 + (\beta_N \hbar \omega_\mathrm{s})^2$ and the k^{th} bead is located in one of the wells. From these relations, it follows that, for $n = 2$, i.e. $N = 2M$,

$$\begin{aligned} q_M^2 (\beta_N \hbar)^{2N} \det \mathbf{G} &= q_M^2 [\alpha p_{N-1} - 2 p_{N-2}] \\ &= q_M^2 [\alpha(\alpha p_{M-2} p_M - 2 p_{M-3} p_M) - 2(\alpha p_{M-3} p_M - 2 p_{M-4} p_M)] \\ &= q_M p_M [\alpha(\alpha p_{M-2} q_M - 2 p_{M-3} q_M) - 2(\alpha p_{M-3} q_M - 2 p_{M-4} q_M)] \\ &= q_M p_M [\alpha(\alpha q_{M-2} p_M - 2 q_{M-3} p_M) - 2(\alpha q_{M-3} p_M - 2 q_{M-4} p_M)] \\ &= p_M^2 [\alpha(\alpha q_{M-2} q_M - 2 q_{M-3} q_M) - 2(\alpha q_{M-3} q_M - 2 q_{M-4} q_M)] \\ &= p_M^2 (\beta_N \hbar)^{2N} \det \mathbf{G_0}. \end{aligned} \tag{E.16}$$

This final expression is almost a proof of Eq. E.1 in the case of $n = 2$, except that the latter involves $\det' \mathbf{G}$ and $\det' \mathbf{J}$, in which the zero-frequency mode

s_1 of Eq. 5.12 has been projected out. However, since we can write

$$\det{}' \mathbf{J} = \det\left(\mathbf{J} + \mathbf{v}\mathbf{v}^{\mathbf{T}}\right), \tag{E.17}$$

where the elements are $\mathbf{v}$ are $v_i = (\tilde{x}_{i+1} - \tilde{x}_i)\sqrt{m/\beta_N \hbar S_{\text{kink}}}$ (from Eq. 5.12), and $\mathbf{v}$ is zero at $\pm x_0$, the above proof applies also to $\det{}' \mathbf{G}$ and $\det{}' \mathbf{J}$. Hence we have proved Eq. E.1 for a one-dimensional system in the case that $n = 2$.

To extend the proof to $n > 2$, we can generalize Eq. E.16 for the case $q_M^n (\beta_N \hbar)^{nN} \det \mathbf{G}$. The determinant $\det \mathbf{G}$ can be split in exactly the same way into p-terms, and when these are exchanged for q-terms using Eq. E.13, the expression is equal to $p_M^n (\beta_N \hbar)^{nN} \det \mathbf{G_0}$.

To extend the proof to multiple dimensions, one transforms the Hessians to the coordinate system $\mathbf{q}$ of the normal modes at the well minimum. These are obtained by computing the eigenvectors of the Hessian at the position $\mathbf{x_0}$ or from the formulae in Eq. 2.22. As a result the Hessian matrix contains no coupling terms between different components of $\mathbf{q}$, except along the kinks. The relations derived above can then be applied independently to each component of $\mathbf{q}$.

Bibliography

I. Affleck. "Quantum-statistical metastability." *Phys. Rev. Lett.* **46**(6), 388 (1981).

C. Alexandrou and J. W. Negele. "Stochastic calculation of tunneling in systems with many degrees of freedom." *Phys. Rev. C* **37**(4), 1513 (1988).

S. C. Althorpe. "On the equivalence of two commonly used forms of semiclassical instanton theory." *J. Chem. Phys.* **134**, 114104 (2011).

S. C. Althorpe and D. C. Clary. "Calculation of the intermolecular bound states for water dimer." *J. Chem. Phys.* **101**(5), 3603 (1994).

S. C. Althorpe and D. C. Clary. "A new method for calculating the rovibrational states of polyatomics with application to water dimer." *J. Chem. Phys.* **102**(11), 4390 (1995).

S. C. Althorpe and D. C. Clary. "Quantum scattering calculations on chemical reactions." In vol. 54 of *Annu. Rev. Phys. Chem.*, edited by S. R. Leone, pp. 493–529 (Palo Alto, Calif.: Annual Reviews, 2003).

S. C. Althorpe, D. C. Clary and P. R. Bunker. "Calculation of the far-infrared spectra for $(HF)_2$, $(HCl)_2$ and $(HBr)_2$." *Chem. Phys. Lett.* **187**(4), 345 (1991).

H. C. Andersen. "Molecular dynamics simulations at constant pressure and/or temperature." *J. Chem. Phys.* **72**(4), 2384 (1980).

H. C. Andersen. "Rattle: A "velocity" version of the shake algorithm for molecular dynamics calculations." *J. Comput. Phys.* **52**, 24 (1983).

S. Andersson, G. Nyman, A. Arnaldsson, U. Manthe and H. Jónsson. "Comparison of quantum dynamics and quantum transition state theory estimates of the $H + CH_4$ reaction rate." *J. Phys. Chem. A* **113**(16), 4468 (2009).

S. Andersson, T. P. M. Goumans and A. Arnaldsson. "Tunneling in hydrogen and deuterium atom addition to CO at low temperatures." *Chem. Phys. Lett.* **513**, 31 (2011).

P. Atkins and R. Friedman. *Molecular Quantum Mechanics*. 4th ed. (New York: Oxford University Press, 2005).

J. Baker. "An algorithm for the location of transition states." *J. Comput. Chem.* **7**(4), 385 (1986).

S. L. Baughcum, Z. Smith, E. B. Wilson and R. W. Duerst. "Microwave spectroscopic study of malonaldehyde. 3. Vibration-rotation interaction and one-dimensional model for proton tunneling." *J. Am. Chem. Soc* **106**(8), 2260 (1984).

S. a Beccara, G. Garberoglio, P. Faccioli and F. Pederiva. "Communications: *Ab initio* dynamics of rare thermally activated reactions." *J. Chem. Phys.* **132**, 111102 (2010).

V. A. Benderskii, D. E. Makarov and C. A. Wight. *Chemical Dynamics at Low Temperatures*, vol. 88 of *Adv. Chem. Phys.* (New York: John Wiley and Sons, 1994).

E. Bitzek, P. Koskinen, F. Gähler, M. Moseler and P. Gumbsch. "Structural relaxation made simple." *Phys. Rev. Lett.* **97**, 170201 (2006).

J. M. Blatt. "Practical points concerning the solution of the Schrödinger equation." *J. Comput. Phys.* **1**, 382 (1967).

J. M. Bofill. "Updated Hessian matrix and the restricted step method for locating transition structures." *J. Comput. Chem.* **15**(1), 1 (1994).

J. A. Bondy and U. S. R. Murty. *Graph Theory with Applications* (London: Macmillan, 1976).

A. I. Boothroyd, W. J. Keogh, P. G. Martin and M. R. Peterson. "An improved H_3 potential energy surface." *J. Chem. Phys.* **95**(6), 4343 (1991).

A. I. Boothroyd, W. J. Keogh, P. G. Martin and M. R. Peterson. "A refined H_3 potential energy surface." *J. Chem. Phys.* **104**(18), 7139 (1996).

L. Bove, S. Klotz, A. Paciaroni and F. Sacchetti. "Anomalous proton dynamics in ice at low temperatures." *Phys. Rev. Lett.* **103**, 165901 (2009).

J. M. Bowman. "Reduced dimensionality theory of quantum reactive scattering." *J. Phys. Chem.* **95**(13), 4960 (1991).

J. M. Bowman, D. Wang, X. Huang, F. Huarte-Larrañaga and U. Manthe. "The importance of an accurate CH_4 vibrational partition function in full dimensionality calculations of the $H + CH_4 \rightarrow H + CH_4$ reaction." *J. Chem. Phys.* **114**(21), 9683 (2001).

B. J. Braams and D. E. Manolopoulos. "On the short-time limit of ring polymer molecular dynamics." *J. Chem. Phys.* **125**, 124105 (2006).

G. Brink and L. Glasser. "Studies in hydrogen bonding: The octamers of water." *J. Phys. Chem.* **88**(16), 3412 (1984).

U. Buck, I. Ettischer, M. Melzer, V. Buch and J. Sadlej. "Structure and spectra of three-dimensional $(H_2O)_n$ clusters, $n = 8, 9, 10$." *Phys. Rev. Lett.* **80**(12), 2578 (1998).

C. G. Callan, Jr and S. Coleman. "Fate of the false vacuum. II. First quantum corrections." *Phys. Rev. D* **16**(6), 1762 (1977).

J. Cao and G. A. Voth. "A unified framework for quantum activated rate processes. I. General theory." *J. Chem. Phys.* **105**(16), 6856 (1996).

B. K. Carpenter. "Taking the high road and getting there before you." *Science* **332**, 1269 (2011).

W. Cencek, K. Szalewicz, C. Leforestier, R. van Harrevelt and A. van der Avoird. "An accurate analytic representation of the water pair potential." *Phys. Chem. Chem. Phys.* **10**, 4716 (2008).

D. M. Ceperley. "Path integrals in the theory of condensed helium." *Rev. Mod. Phys.* **67**(2), 279 (1995).

D. M. Ceperley and G. Jacucci. "Calculation of exchange frequencies in bcc ^{3}He with the path-integral Monte Carlo method." *Phys. Rev. Lett.* **58**(16), 1648 (1987).

S. I. Chan and D. Stelman. "Oscillators perturbed by Gaussian barriers." *J. Chem. Phys.* **39**(3), 545 (1963).

D. Chandler. *Introduction to Modern Statistical Mechanics* (New York: Oxford University Press, 1987).

D. Chandler and P. G. Wolynes. "Exploiting the isomorphism between quantum theory and classical statistical mechanics of polyatomic fluids." *J. Chem. Phys.* **74**(7), 4078 (1981).

H. Chen, S. Liu and J. C. Light. "Six-dimensional quantum calculation of the intermolecular bound states for water dimer." *J. Chem. Phys.* **110**(1), 168 (1999).

D. F. Coker and R. O. Watts. "Structure and vibrational spectroscopy of the water dimer using quantum simulation." *J. Phys. Chem.* **91**(10), 2513 (1987).

S. Coleman. "Fate of the false vacuum: Semiclassical theory." *Phys. Rev. D* **15**(10), 2929 (1977*a*).

S. Coleman. "The uses of instantons." In *Proc. Int. School of Subnuclear Physics* (Erice, 1977*b*). Also in S. Coleman, *Aspects of Symmetry*, chapter 7, pp. 265–350 (Cambridge: Cambridge University Press, 1985).

R. Collepardo-Guevara, I. R. Craig and D. E. Manolopoulos. "Proton transfer in a polar solvent from ring polymer reaction rate theory." *J. Chem. Phys.* **128**, 144502 (2008).

R. Collepardo-Guevara, Y. V. Suleimanov and D. E. Manolopoulos. "Bimolecular reaction rates from ring polymer molecular dynamics." *J. Chem. Phys.* **130**, 174713 (2009).

R. Collepardo-Guevara, Y. V. Suleimanov and D. E. Manolopoulos. "Erratum: "Bimolecular reaction rates from ring polymer molecular dynamics" [J. Chem. Phys. 130, 174713 (2009)]." *J. Chem. Phys.* **133**, 049902 (2010).

L. H. Coudert and J. T. Hougen. "Tunneling splittings in the water dimer: Further development of the theory." *J. Mol. Spectrosc.* **130**, 86 (1988).

I. R. Craig and D. E. Manolopoulos. "Quantum statistics and classical mechanics: Real time correlation functions from ring polymer molecular dynamics." *J. Chem. Phys.* **121**(8), 3368 (2004).

I. R. Craig and D. E. Manolopoulos. "Chemical reaction rates from ring polymer molecular dynamics." *J. Chem. Phys.* **122**, 084106 (2005*a*).

I. R. Craig and D. E. Manolopoulos. "A refined ring polymer molecular dynamics theory of chemical reaction rates." *J. Chem. Phys.* **123**, 034102 (2005*b*).

D. di Domenico, M. I. Hernández and J. Campos-Martínez. "A time-dependent wave packet approach for reaction and dissociation in $H_2 + H_2$." *Chem. Phys. Lett.* **342**, 177 (2001).

A. N. Drozdov. "Improved Feynman's path integral method with a large time step: Formalism and applications." *J. Chem. Phys.* **108**(16), 6580 (1998).

R. J. Duchovic, Y. L. Volobuev, G. C. Lynch, A. W. Jasper, D. G. Truhlar, T. C. Allison, A. F. Wagner, B. C. Garrett, J. Espinosa-García and J. C. Corchado. "POTLIB." (2001–). URL `http://comp.chem.umn.edu/potlib`.

T. R. Dyke. "Group theoretical classification of the tunneling-rotational energy levels of water dimer." *J. Chem. Phys.* **66**(2), 492 (1977).

T. R. Dyke, K. M. Mack and J. S. Muenter. "The structure of water dimer from molecular beam electric resonance spectroscopy." *J. Chem. Phys.* **66**(2), 498 (1977).

C. Eckart. "The penetration of a potential barrier by electrons." *Phys. Rev.* **35**(11), 1303 (1930).

H. Eyring. "The activated complex in chemical reactions." *J. Chem. Phys.* **3**, 107 (1935).

P. Faccioli, M. Sega, F. Pederiva and H. Orland. "Dominant pathways in protein folding." *Phys. Rev. Lett.* **97**, 108101 (2006).

G. S. Fanourgakis and S. S. Xantheas. "Development of transferable interaction potentials for water. V. Extension of the flexible, polarizable, Thole-type model potential (TTM3-F, v. 3.0) to describe the vibrational spectra of water clusters and liquid water." *J. Chem. Phys.* **128**, 074506 (2008).

M. D. Feit, J. A. Fleck, Jr. and A. Steiger. "Solution of the Schrödinger equation by a spectral method." *J. Comput. Phys.* **47**, 412 (1982).

R. S. Fellers, L. B. Braly, R. J. Saykally and C. Leforestier. "Fully coupled six-dimensional calculations of the water dimer vibration-rotation-tunneling states with split Wigner pseudospectral approach. II. Improvements and tests of additional potentials." *J. Chem. Phys.* **110**(13), 6306 (1999).

R. P. Feynman. *Statistical Mechanics: A set of Lectures* (Reading, Mass.: W. A. Benjamin, 1972).

R. P. Feynman and A. R. Hibbs. *Quantum Mechanics and Path Integrals* (New York: McGraw-Hill, 1965).

D. W. Firth, K. Beyer, M. A. Dvorak, S. W. Reeve, A. Grushow and K. R. Leopold. "Tunable far-infrared spectroscopy of malonaldehyde." *J. Chem. Phys.* **94**(3), 1812 (1991).

R. Fletcher. *Practical Methods of Optimization.* 2nd ed. (Chichester: John Wiley and Sons, 1987).

J. E. Fowler and H. F. Schaefer III. "Detailed study of the water trimer potential energy surface." *J. Am. Chem. Soc* **117**(1), 446 (1995).

G. T. Fraser, R. D. Suenram and L. H. Coudert. "Microwave electric-resonance optothermal spectroscopy of $(H_2O)_2$." *J. Chem. Phys.* **90**(11), 6077 (1989).

D. Frenkel and B. Smit. *Understanding Molecular Simulation.* 2nd ed. (San Diego: Elsevier, 1996).

M. J. Gillan. "Quantum-classical crossover of the transition rate in the damped double well." *J. Phys. C Solid State* **20**, 3621 (1987).

H. Goldstein, C. Poole and J. Safko. *Classical Mechanics.* 3rd ed. (San Francisco: Addison Wesley, 2002).

T. Gonzalez-Lezana, E. J. Rackham and D. E. Manolopoulos. "Quantum reactive scattering with a transmission-free absorbing potential." *J. Chem. Phys.* **120**(5), 2247 (2004).

T. P. M. Goumans and J. Kästner. "Deuterium enrichment of interstellar methanol explained by atom tunneling." *J. Phys. Chem. A* **115**, 10767 (2011).

I. S. Gradshteyn and I. M. Ryzhik. *Tables of Integrals, Series and Products.* 6th ed. (San Diego: Academic Press, 2000).

J. K. Gregory and D. C. Clary. "Calculations of the tunneling splittings in water dimer and trimer using diffusion Monte Carlo." *J. Chem. Phys.* **102**(20), 7817 (1995*a*).

J. K. Gregory and D. C. Clary. "Three-body effects on molecular properties in the water trimer." *J. Chem. Phys.* **103**(20), 8924 (1995*b*).

J. K. Gregory and D. C. Clary. "Tunneling dynamics in water tetramer and pentamer." *J. Chem. Phys.* **105**(16), 6626 (1996).

G. C. Groenenboom, P. E. S. Wormer, A. van der Avoird, E. M. Mas, R. Bukowski and K. Szalewicz. "Water pair potential of near spectroscopic accuracy. II. Vibration-rotation-tunneling levels of the water dimer." *J. Chem. Phys.* **113**, 6702 (2000).

C. J. Gruenloh, J. R. Carney, C. A. Arrington, T. S. Zwier, S. Y. Fredericks and K. D. Jordan. "Infrared spectrum of a molecular ice cube: The S_4 and D_{2d} water octamers in benzene-$(water)_8$." *Science* **276**, 1678 (1997).

Y. Guo, T. D. Sewell and D. L. Thompson. "A full-dimensional semiclassical calculation of vibrational mode selectivity in the tunneling splitting in a planar model of malonaldehyde." *Chem. Phys. Lett.* **224**, 470 (1994).

M. C. Gutzwiller. "Phase-integral approximation in momentum space and the bound states of an atom." *J. Math. Phys.* **8**(10), 1979 (1967).

M. C. Gutzwiller. "Periodic orbits and classical quantization conditions." *J. Math. Phys.* **12**(3), 343 (1971).

S. Habershon, G. S. Fanourgakis and D. E. Manolopoulos. "Comparison of path integral molecular dynamics methods for the infrared absorption spectrum of liquid water." *J. Chem. Phys.* **129**, 074501 (2008).

S. Habershon, T. E. Markland and D. E. Manolopoulos. "Competing quantum effects in the dynamics of a flexible water model." *J. Chem. Phys.* **131**, 024501 (2009).

J. W. Halley, J. R. Rustad and A. Rahman. "A polarizable, dissociating molecular dynamics model for liquid water." *J. Chem. Phys.* **98**(5), 4110 (1993).

T. Hammer, M. D. Coutinho-Neto, A. Viel and U. Manthe. "Multiconfigurational time-dependent Hartree calculations for tunneling splittings of vibrational states: Theoretical considerations and application to malonaldehyde." *J. Chem. Phys.* **131**, 224109 (2009).

P. Hänggi, P. Talkner and M. Borkovec. "Reaction-rate theory: Fifty years after Kramers." *Rev. Mod. Phys.* **62**(2), 251 (1990).

D. O. Harris, G. G. Engerholm and W. D. Gwinn. "Calculation of matrix elements for one-dimensional quantum-mechanical problems and the application to anharmonic oscillators." *J. Chem. Phys.* **43**(5), 1515 (1965).

E. J. Heller. "Frozen Gaussians: A very simple semiclassical approximation." *J. Chem. Phys.* **75**(6), 2923 (1981).

G. Henkelman and H. Jónsson. "A dimer method for finding saddle points on high dimensional potential surfaces using only first derivatives." *J. Chem. Phys.* **111**(15), 7010 (1999).

M. F. Herman and E. Kluk. "A semiclasical justification for the use of non-spreading wavepackets in dynamics calculations." *Chem. Phys.* **91**, 27 (1984).

H. F. von Horsten, S. T. Banks and D. C. Clary. "An efficient route to thermal rate constants in reduced dimensional quantum scattering simulations: Applications to the abstraction of hydrogen from alkanes." *J. Chem. Phys.* **135**, 094311 (2011).

X. Huang, B. J. Braams, J. M. Bowman, R. E. A. Kelly, J. Tennyson, G. C. Groenenboom and A. van der Avoird. "New *ab initio* potential energy surface and the vibration-rotation-tunneling levels of $(H_2O)_2$ and $(D_2O)_2$." *J. Chem. Phys.* **128**, 034312 (2008).

F. Huarte-Larrañaga and U. Manthe. "Full dimensional quantum calculations of the $CH_4 + H \rightarrow CH_3 + H_2$ reaction rate." *J. Chem. Phys.* **113**(13), 5115 (2000).

S. Jang and G. A. Voth. "A relationship between centroid dynamics and path integral quantum transition state theory." *J. Chem. Phys.* **112**(20), 8747 (2000).

B. R. Johnson. "The multichannel log-derivative method for scattering calculations." *J. Comput. Phys.* **13**, 445 (1973).

E. Jones, T. Oliphant, P. Peterson et al. "SciPy: Open source scientific tools for Python." (2001–). URL `http://www.scipy.org/`.

S. C. L. Kamerlin and A. Warshel. "An analysis of all the relevant facts and arguments indicates that enzyme catalysis does not involve large contributions from nuclear tunneling." *J. Phys. Org. Chem.* **23**, 677 (2010).

E. N. Karyakin, G. T. Fraser and R. D. Suenram. "Microwave spectrum of the $K_a = 1 \leftarrow 0$ rotation-tunnelling band of $(D_2O)_2$." *Mol. Phys.* **78**(5), 1179 (1993).

J. Kästner and P. Sherwood. "Superlinearly converging dimer method for transition state search." *J. Chem. Phys.* **128**, 014106 (2008).

J. Kästner and W. Thiel. "Bridging the gap between thermodynamic integration and umbrella sampling provides a novel analysis method: "Umbrella integration"." *J. Chem. Phys.* **123**, 144104 (2005).

F. N. Keutsch and R. J. Saykally. "Water clusters: Untangling the mysteries of the liquid, one molecule at a time." *P. Natl. Acad. Sci. USA* **98**(19), 10533 (2001).

F. N. Keutsch, R. J. Saykally and D. J. Wales. "Bifurcation tunneling dynamics in the water trimer." *J. Chem. Phys.* **117**(19), 8823 (2002).

F. N. Keutsch, J. D. Cruzan and R. J. Saykally. "The water trimer." *Chem. Rev.* **103**(7), 2533 (2003*a*).

F. N. Keutsch, N. Goldman, H. A. Harker, C. Leforestier and R. J. Saykally. "Complete characterization of the water dimer vibrational ground state and testing the VRT(ASP-W)III, SAPT-5st, and VRT(MCY-5f) surfaces." *Mol. Phys.* **101**(23–24), 3477 (2003*b*).

J. Kim, D. Majumdar, H. M. Lee and K. S. Kim. "Structures and energetics of the water heptamer: Comparison with the water hexamer and octamer." *J. Chem. Phys.* **110**(18), 9128 (1999).

H. Kleinert. *Path Integrals in Quantum Mechanics, Statistics, Polymer Physics and Financial Markets*. 4th ed. (Singapore: World Scientific, 2006).

M. Kryvohuz. "Semiclassical instanton approach to calculation of reaction rate constants in multidimensional chemical systems." *J. Chem. Phys.* **134**, 114103 (2011).

A. Kuki and P. G. Wolynes. "Electron tunneling paths in proteins." *Science* **236**, 1647 (1987).

R. Kumar and J. L. Skinner. "Water simulation model with explicit three-molecule interactions." *J. Phys. Chem. B* **112**(28), 8311 (2008).

L. D. Landau and E. M. Lifshitz. *Quantum Mechanics: Non-Relativistic Theory.* 2nd ed. (Oxford: Pergamon Press, 1965).

H. M. Lee, S. B. Suh, J. Y. Lee, P. Tarakeshwar and K. S. Kim. "Structures, energies, vibrational spectra, and electronic properties of water monomer to decamer." *J. Chem. Phys.* **112**(22), 9759 (2000).

C. Leforestier, F. Gatti, R. S. Fellers and R. J. Saykally. "Determination of a flexible (12D) water dimer potential via direct inversion of spectroscopic data." *J. Chem. Phys.* **117**(19), 8710 (2002).

R. D. Levine. *Molecular Reaction Dynamics* (Cambridge: Cambridge University Press, 2005).

J. C. Light, I. P. Hamilton and J. V. Lill. "Generalized discrete variable approximation in quantum mechanics." *J. Chem. Phys.* **82**(3), 1400 (1985).

D. C. Liu and J. Nocedal. "On the limited memory BFGS method for large scale optimization." *Math. Program.* **45**, 503 (1989).

J. Liu and W. H. Miller. "A simple model for the treatment of imaginary frequencies in chemical reaction rates and molecular liquids." *J. Chem. Phys.* **131**, 074113 (2009).

K. Liu, J. G. Loeser, M. J. Elrod, B. C. Host, J. A. Rzepiela, N. Pugliano and R. J. Saykally. "Dynamics of structural rearrangements in the water trimer." *J. Am. Chem. Soc* **116**(8), 3507 (1994).

K. Liu, M. G. Brown, M. R. Viant, J. D. Cruzan and R. J. Saykally. "Far infrared VRT spectroscopy of two water trimer isotopomers: Vibrationally averaged structures and rearrangement dynamics." *Mol. Phys.* **89**(5), 1373 (1996).

T. Loerting, K. R. Liedl and B. M. Rode. "Predictions of rate constants and estimates for tunneling splittings of concerted proton transfer in small cyclic water clusters." *J. Chem. Phys.* **109**(7), 2672 (1998).

H. C. Longuet-Higgins. "The symmetry groups of non-rigid molecules." *Mol. Phys.* **6**(5), 445 (1963).

S. Maeda and K. Ohno. "Structures of water octamers $(H_2O)_8$: Exploration on ab initio potential energy surfaces by the scaled hypersphere search method." *J. Phys. Chem. A* **111**(20), 4527 (2007).

D. E. Makarov and M. Topaler. "Quantum transition-state theory below the crossover temperature." *Phys. Rev. E* **52**(1), 178 (1995).

D. E. Manolopoulos. "An improved log derivative method for inelastic scattering." *J. Chem. Phys.* **85**(11), 6425 (1986).

U. Manthe, T. Seideman and W. H. Miller. "Full-dimensional quantum mechanical calculation of the rate constant for the $H_2 + OH \rightarrow H_2O + H$ reaction." *J. Chem. Phys.* **99**(12), 10078 (1993).

M. Marchi and D. Chandler. "Path-integral calculation of the tunnel splitting in aqueous ferrous–ferric electron transfer." *J. Chem. Phys.* **95**(2), 889 (1991).

R. A. Marcus and M. E. Coltrin. "A new tunneling path for reactions such as $H + H_2 \rightarrow H_2 + H$." *J. Chem. Phys.* **67**, 2609 (1977).

D. Marx and M. H. Müser. "Path integral simulations of rotors: Theory and applications." *J. Phys.-Condens. Mat.* **11**, R117 (1999).

D. Marx and M. Parrinello. "*Ab initio* path integral molecular dynamics: Basic ideas." *J. Chem. Phys.* **104**(11), 4077 (1996).

O. Matsuoka, E. Clementi and M. Yoshimine. "CI study of the water dimer potential surface." *J. Chem. Phys.* **64**(4), 1351 (1976).

B. J. McClelland. *Statistical Thermodynamics* (London: Chapman and Hall, 1973).

J. Meisner, J. B. Rommel and J. Kästner. "Kinetic isotope effects calculated with the instanton method." *J. Comput. Chem.* **32**(16), 3456 (2011).

H.-D. Meyer, F. Gatti and G. W. Worth, editors. *Multidimensional Quantum Dynamics: MCTDH Theory and Applications* (Weinheim: Wiley-VCH, 2009).

W. H. Miller. "Classical path approximation for the Boltzmann density matrix." *J. Chem. Phys.* **55**(7), 3146 (1971).

W. H. Miller. "Classical-limit quantum mechanics and the theory of molecular collisions." In vol. 25 of *Adv. Chem. Phys.*, edited by I. Prigogine and S. A. Rice, pp. 69–177 (New York: John Wiley and Sons, 1974*a*).

W. H. Miller. "Quantum mechanical transition state theory and a new semiclassical model for reaction rate constants." *J. Chem. Phys.* **61**(5), 1823 (1974*b*).

W. H. Miller. "Semiclassical limit of quantum mechanical transition state theory for nonseparable systems." *J. Chem. Phys.* **62**(5), 1899 (1975).

W. H. Miller. "Periodic orbit description of tunneling in symmetric and asymmetric double-well potentials." *J. Phys. Chem.* **83**(8), 960 (1979).

W. H. Miller. "Beyond transition-state theory: A rigorous quantum theory of chemical reaction rates." *Accounts Chem. Res.* **26**(4), 174 (1993).

W. H. Miller. "The semiclassical initial value representation: A potentially practical way for adding quantum effects to classical molecular dynamics simulations." *J. Phys. Chem. A* **105**(13), 2942 (2001).

W. H. Miller, S. D. Schwartz and J. W. Tromp. "Quantum mechanical rate constants for bimolecular reactions." *J. Chem. Phys.* **79**(10), 4889 (1983).

W. H. Miller, Y. Zhao, M. Ceotto and S. Yang. "Quantum instanton approximation for thermal rate constants of chemical reactions." *J. Chem. Phys.* **119**(3), 1329 (2003).

C. Millot, J.-C. Soetens, M. T. C. Martins Costa, M. P. Hodges and A. J. Stone. "Revised anisotropic site potentials for the water dimer and calculated properties." *J. Phys. Chem. A* **102**(4), 754 (1998).

G. Mills, G. K. Schenter, D. E. Makarov and H. Jónsson. "Generalized path integral based quantum transition state theory." *Chem. Phys. Lett.* **278**, 91 (1997).

G. V. Mil'nikov and H. Nakamura. "Practical implementation of the instanton theory for the ground-state tunneling splitting." *J. Chem. Phys.* **115**(15), 6881 (2001).

G. V. Mil'nikov, K. Yagi, T. Taketsugu, H. Nakamura and K. Hirao. "Simple and accurate method to evaluate tunneling splitting in polyatomic molecules." *J. Chem. Phys.* **120**(11), 5036 (2004).

L. J. Munro and D. J. Wales. "Defect migration in crystalline silicon." *Phys. Rev. B* **59**(6), 3969 (1999).

J. Nichols, H. Taylor, P. Schmidt and J. Simons. "Walking on potential energy surfaces." *J. Chem. Phys.* **92**(1), 340 (1990).

J. Nocedal. "Updating quasi-Newton matrices with limited storage." *Math. Comput.* **35**(151), 773 (1980).

E. H. T. Olthof, A. van der Avoird, P. E. S. Wormer, K. Liu and R. J. Saykally. "Tunneling dynamics, symmetry, and far-infrared spectrum of the rotating water trimer. II. Calculations and experiments." *J. Chem. Phys.* **105**(18), 8051 (1996).

M. Parrinello and A. Rahman. "Study of an F center in molten KCl." *J. Chem. Phys.* **80**(2), 860 (1984).

M. R. Pastrana, L. A. M. Quintales, J. Brandão and A. J. C. Varandas. "Recalibration of a single-valued double many-body expansion potential energy surface for ground-state HO_2 and dynamics calculations for the $O + OH \rightarrow O_2 + H$ reaction." *J. Phys. Chem.* **94**(21), 8073 (1990).

J. B. Paul, R. A. Provencal and R. J. Saykally. "Characterization of the $(D_2O)_2$ hydrogen-bond-acceptor antisymmetric stretch by IR cavity ringdown laser absorption spectroscopy." *J. Phys. Chem. A* **102**(19), 3279 (1998).

A. M. Polyakov. "Quark confinement and topology of gauge theories." *Nucl. Phys. B* **120**, 429 (1977).

W. H. Press, S. A. Teukolsky, W. T. Vetterling and B. P. Flannery. *Numerical Recipes in Fortran 77: The Art of Scientific Computing.* 2nd ed. (Cambridge: Cambridge University Press, 1992).

N. Pugliano and R. J. Saykally. "Measurement of quantum tunneling between chiral isomers of the cyclic water trimer." *Science* **257**, 1937 (1992).

M. Quack and M. A. Suhm. "Accurate quantum Monte Carlo calculations of the tunneling splitting in $(HF)_2$ on a six-dimensional potential hypersurface." *Chem. Phys. Lett.* **234**, 71 (1995).

J. O. Richardson and S. C. Althorpe. "Ring-polymer molecular dynamics rate-theory in the deep-tunneling regime: Connection with semiclassical instanton theory." *J. Chem. Phys.* **131**, 214106 (2009).

J. O. Richardson and S. C. Althorpe. "Ring-polymer instanton method for calculating tunneling splittings." *J. Chem. Phys.* **134**, 054109 (2011).

J. O. Richardson, S. C. Althorpe and D. J. Wales. "Instanton calculations of tunneling splittings for water dimer and trimer." *J. Chem. Phys.* **135**, 124109 (2011).

J. B. Rommel and J. Kästner. "Adaptive integration grids in instanton theory improve the numerical accuracy at low temperature." *J. Chem. Phys.* **134**, 184107 (2011).

J. B. Rommel, T. P. M. Goumans and J. Kästner. "Locating instantons in many degrees of freedom." *J. Chem. Theory Comput.* **7**, 690 (2011).

L. Salem. *The Molecular Orbital Theory of Conjugated Systems* (New York: W. A. Benjamin, 1966).

R. J. Saykally (2012). *Private communication.*

L. I. Schiff. *Quantum Mechanics.* 3rd ed. (New York: McGraw-Hill, 1968).

P. R. Schreiner, H. P. Reisenauer, D. Ley, D. Gerbig, C.-H. Wu and W. D. Allen. "Methylhydroxycarbene: Tunneling control of a chemical reaction." *Science* **332**, 1300 (2011).

T. D. Sewell, Y. Guo and D. L. Thompson. "Semiclassical calculations of tunneling splitting in malonaldehyde." *J. Chem. Phys.* **103**(19), 8557 (1995).

A. Shank, Y. Wang, A. Kaledin, B. J. Braams and J. M. Bowman. "Accurate *ab initio* and "hybrid" potential energy surfaces, intramolecular vibrational energies, and classical ir spectrum of the water dimer." *J. Chem. Phys.* **130**, 144314 (2009).

D. Sheppard, R. Terrell and G. Henkelman. "Optimization methods for finding minimum energy paths." *J. Chem. Phys.* **128**, 134106 (2008).

D. E. Skinner and W. H. Miller. "Application of the semiclassical initial value representation and its linearized approximation to inelastic scattering." *Chem. Phys. Lett.* **300**, 20 (1999).

B. J. Smith, D. J. Swanton, J. A. Pople, H. F. Schaefer III and L. Radom. "Transition structures for the interchange of hydrogen atoms within the water dimer." *J. Chem. Phys.* **92**(2), 1240 (1990).

T. Stecher. *Benchmark Studies of Ring Polymer Molecular Dynamics Rate Theory.* Ph.D. thesis, University of Cambridge (2010).

F. H. Stillinger and C. W. David. "Polarization model for water and its ionic dissociation products." *J. Chem. Phys.* **69**(4), 1473 (1978).

F. H. Stillinger and C. W. David. "Study of the water octamer using the polarization model of molecular interactions." *J. Chem. Phys.* **73**(7), 3384 (1980).

R. D. Suenram, G. T. Fraser and F. J. Lovas. "Microwave spectrum of $(D_2O)_2$." *J. Mol. Spectrosc.* **138**, 440 (1989).

M. A. Suhm and R. O. Watts. "Quantum Monte Carlo studies of vibrational states in molecules and clusters." *Phys. Rep.* **204**(4), 293 (1991).

Y. V. Suleimanov, R. Collepardo-Guevara and D. E. Manolopoulos. "Bimolecular reaction rates from ring polymer molecular dynamics: Application to $H + CH_4 \rightarrow H_2 + CH_3$." *J. Chem. Phys.* **134**, 044131 (2011).

H. Sun and R. O. Watts. "Diffusion Monte Carlo simulations of hydrogen fluoride dimers." *J. Chem. Phys.* **92**(1), 603 (1990).

S. Suzuki and G. A. Blake. "Pseudorotation in the D_2O trimer." *Chem. Phys. Lett.* **229**, 499 (1994).

K. Szalewicz, C. Leforestier and A. van der Avoird. "Towards the complete understanding of water by a first-principles computational approach." *Chem. Phys. Lett.* **482**, 1 (2009).

M. Takahashi, Y. Watanabe, T. Taketsugu and D. J. Wales. "An *ab initio* study of tunneling splittings in the water trimer." *J. Chem. Phys.* **123**, 044302 (2005).

T. Taketsugu and D. J. Wales. "Theoretical study of rearrangements in water dimer and trimer." *Mol. Phys.* **100**(17), 2793 (2002).

D. J. Tannor. *Introduction to Quantum Mechanics: A Time-Dependent Perspective* (Sausalito, Calif.: University Science Books, 2007).

C. S. Tautermann, A. F. Voegele, T. Loerting and K. R. Liedl. "The optimal tunneling path for the proton transfer in malonaldehyde." *J. Chem. Phys.* **117**(5), 1962 (2002*a*).

C. S. Tautermann, A. F. Voegele, T. Loerting and K. R. Liedl. "An accurate semiclassical method to predict ground-state tunneling splittings." *J. Chem. Phys.* **117**(5), 1967 (2002*b*).

D. G. Truhlar and B. C. Garrett. "Variational transition state theory." In vol. 35 of *Annu. Rev. Phys. Chem.*, edited by B. S. Rabinovitch, pp. 159–189 (Palo Alto, Calif.: Annual Reviews, 1984).

D. G. Truhlar, A. D. Isaacson and B. C. Garrett. "Generalized transition state theory." In *Theory of Chemical Reaction Dynamics*, vol. IV, edited by M. Baer, chap. 2, pp. 65–137 (Boca Raton, Fla.: CRC Press, 1985).

C. J. Tsai and K. D. Jordan. "Monte Carlo simulation of $(H_2O)_8$: Evidence for a low-energy S_4 structure and characterization of the solid $\leftrightarrow$ liquid transition." *J. Chem. Phys.* **95**(5), 3850 (1991).

M. E. Tuckerman. "Path integration via molecular dynamics." In *Quantum Simulations of Complex Many-Body Systems: From Theory to Algorithms,* Lecture Notes, vol. 10 of *NIC Series*, edited by J. Grotendorst, D. Marx and A. Muramatsu, pp. 269–298 (Jülich: John von Neumann Institute for Computing, 2002).

A. I. Vainshtein, V. I. Zakharov, V. A. Novikov and M. A. Shifman. "ABC of instantons." **25**, 195 (1982). Also in *Instantons in Gauge Theories*, edited by M. Shifman, pp. 468 (Singapore: World Scientific, 1994).

J. Vaníček, W. H. Miller, J. F. Castillo and F. J. Aoiz. "Quantum-instanton evaluation of the kinetic isotope effects." *J. Chem. Phys.* **123**, 054108 (2005).

M. R. Viant, J. D. Cruzan, D. D. Lucas, M. G. Brown, K. Liu and R. J. Saykally. "Pseudorotation in water trimer isotopomers using terahertz laser spectroscopy." *J. Phys. Chem. A* **101**(48), 9032 (1997).

J. H. van Vleck. "The correspondence principle in the statistical interpretation of quantum mechanics." *P. Natl. Acad. Sci. USA* **14**(2), 178 (1928).

G. A. Voth. "Path-integral centroid methods in quantum statistical mechanics and dynamics." In *New Methods in Computational Quantum Mechanics*, vol. 93 of *Adv. Chem. Phys.*, edited by I. Prigogine and S. A. Rice, pp. 135–218 (New York: John Wiley and Sons, 1996).

G. A. Voth, D. Chandler and W. H. Miller. "Rigorous formulation of quantum transition state theory and its dynamical corrections." *J. Chem. Phys.* **91**(12), 7749 (1989).

D. J. Wales. "OPTIM, a program for optimizing geometries and calculating reaction pathways." URL `http://www-wales.ch.cam.ac.uk/software.html`.

D. J. Wales. "Theoretical study of water trimer." *J. Am. Chem. Soc* **115**(24), 11180 (1993*a*).

D. J. Wales. "Some estimates of tunneling splittings in small clusters." *J. Am. Chem. Soc* **115**(24), 11191 (1993*b*).

D. J. Wales. "Rearrangements of water dimer and hexamer." In *Theory of Atomic and Molecular Clusters: With a Glimpse at Experiments*, edited by J. Jellinek, pp. 86–110 (Berlin: Springer-Velag, 1999).

D. J. Wales. *Energy Landscapes* (Cambridge: Cambridge University Press, 2003).

D. J. Wales and I. Ohmine. "Rearrangements of model $(H_2O)_8$ and $(H_2O)_{20}$ clusters." *J. Chem. Phys.* **98**(9), 7257 (1993).

D. J. Wales and T. R. Walsh. "Theoretical study of the water pentamer." *J. Chem. Phys.* **105**(16), 6957 (1996).

T. R. Walsh and D. J. Wales. "Rearrangements of the water trimer." *J. Chem. Soc. Faraday Trans.* **92**(14), 2505 (1996).

Y. Wang and J. M. Bowman. "One-dimensional tunneling calculations in the imaginary-frequency, rectilinear saddle-point normal mode." *J. Chem. Phys.* **129**, 121103 (2008).

Y. Wang and J. M. Bowman. "Towards an *ab initio* flexible potential for water, and post-harmonic quantum vibrational analysis of water clusters." *Chem. Phys. Lett.* **491**, 1 (2010).

Y. Wang and J. M. Bowman (2011). *Private communication.*

Y. Wang, B. J. Braams, J. M. Bowman, S. Carter and D. P. Tew. "Full-dimensional quantum calculations of ground-state tunneling splitting of malonaldehyde using an accurate *ab initio* potential energy surface." *J. Chem. Phys.* **128**, 224314 (2008).

Y. Wang, B. C. Shepler, B. J. Braams and J. M. Bowman. "Full-dimensional, *ab initio* potential energy and dipole moment surfaces for water." *J. Chem. Phys.* **131**, 054511 (2009).

Y. Wang, J. M. Bowman and X. Huang. "Communication: Prediction of the rate constant of bimolecular hydrogen exchange in the water dimer using an *ab initio* potential energy surface." *J. Chem. Phys.* **133**, 111103 (2010).

Y. Wang, X. Huang, B. C. Shepler, B. J. Braams and J. M. Bowman. "Flexible, *ab initio* potential, and dipole moment surfaces for water. I. Tests and applications for clusters up to the 22-mer." *J. Chem. Phys.* **134**, 094509 (2011).

Y. Watanabe, T. Taketsugu and D. J. Wales. "An *ab initio* study of tunneling splittings in the water dimer." *J. Chem. Phys.* **120**(13), 5993 (2004).

H.-J. Werner, P. J. Knowles, G. Knizia, F. R. Manby, M. Schütz et al. "MOLPRO, version 2010.1, a package of ab initio programs." (2010). URL `http://www.molpro.net`.

E. P. Wigner. "Über das überschreiten von Potentialschwellen bei chemischen Reaktionen." *Z. Phys. Chem. B* **19**(2/3), 203 (1932).

R. J. Wilson. *Introduction to Graph Theory.* 4th ed. (Harlow: Pearson Education, 1996).

S. S. Xantheas and E. Aprà. "The binding energies of the D_{2d} and S_4 water octamer isomers: High-level electronic structure and empirical potential results." *J. Chem. Phys.* **120**(2), 823 (2004).

K. Yagi, T. Taketsugu and K. Hirao. "Generation of full-dimensional potential energy surface of intramolecular hydrogen atom transfer in malonaldehyde and tunneling dynamics." *J. Chem. Phys.* **115**(23), 10647 (2001).

T. Yamamoto and W. H. Miller. "On the efficient path integral evaluation of thermal rate constants within the quantum instanton approximation." *J. Chem. Phys.* **120**(7), 3086 (2004).

T. Yamamoto, H. Wang and W. Miller. "Combining semiclassical time evolution and quantum Boltzmann operator to evaluate reactive flux correlation function for thermal rate constants of complex systems." *J. Chem. Phys.* **116**(17), 7335 (2002).

D. H. Zhang and J. Z. H. Zhang. "Full-dimensional time-dependent treatment for diatom–diatom reactions: the $H_2 + OH$ reaction." *J. Chem. Phys.* **101**(2), 1146 (1994).

C. Zhu, R. H. Byrd, P. Lu and J. Nocedal. "Algorithm 778: L-BFGS-B: Fortran subroutines for large-scale bound-constrained optimization." *ACM Trans. Math. Softw.* **23**(4), 550 (1997).

E. Zwart, J. J. ter Meulen, W. L. Meerts and L. H. Coudert. "The submillimeter rotation tunneling spectrum of the water dimer." *J. Mol. Spectrosc.* **147**, 27 (1991).